RICE UNIVERSITY

INERT GAS INVESTIGATIONS OF THE APOLLO 15 AND 17 LANDING SITES

by

JIMMIE LYNN JORDAN

A THESIS SUBMITTED

IN PARTIAL FULFILLMENT OF THE

REQUIREMENTS FOR THE DEGREE OF

DOCTOR OF PHILOSOPHY

Thesis Director's Signature

Houston, Texas

April, 1975

TABLE OF CONTENTS

I. INTRODUCTION

The lunar surface may be thought of as a large target for various kinds of irradiation in space. The three basic kinds of charged particle irradiation may be classified according to their energy, depth, and type of interaction with the solid materials of the moon: 1 With energies up to 100 GeV, galactic cosmic rays and their less energetic secondaries penetrate to depths of several meters, producing spallation products. 2 Solar cosmic rays associated with solar flare events have energies up to several hundred MeV and produce spallation products mainly in the upper few centimeters of the lunar surface. 3 Solar wind ions penetrate to depths of 1 μm in the lunar surface and firmly implant themselves to these depths. The solar wind constitutes the source of the largest amounts of inert gases found in the lunar soil.

The lunar surface is subject to bombardments of larger scale as well - its surface has suffered numerous large meteorite impacts and even today soil particles are continuously being fractured by micrometeorites. The net result is to juxtapose and even erase the historical record of the charged particle irradiation. Grains from all depths sampled contain some solar wind gas, suggesting that every particle has been at the surface at one time or another -

when or how long a particle has been at the surface is a most difficult question to answer.

Another, related problem is that while the fragmented materials of the lunar surface, collectively referred to as the regolith, extend from 5 m to 10 m the cosmic ray exposure ages of individual particles rarely exceed 10^9 yr, and more often these are only a few hundred million years. Yet, the moon has probably been in existence for 4.5 by - where are the particles with cosmic ray exposure ages comparable to this formation age? Fireman (1974) has suggested that the moon is losing mass by micrometeorite bombardment at a rate of $\sim$ 80 g/cm^2 per 10^9 yr. This could be the explanation for the missing cosmic ray record, but irradiation history of the zone just beneath the regolith is not well understood. Perhaps this zone is heavily irradiated with respect to cosmic rays.

Other questions present themselves: Do inert gases imbedded in the surfaces of particles reflect only present day solar wind composition or can one find particles which contain the record of ancient solar wind? Are surfaces saturated with solar wind ions or can one find particles whose surfaces are undersaturated, allowing one to make firm statements about relative exposure to solar irradiation?

In an attempt to answer these questions, at least in part, I have analyzed several lunar surface fines (particles

with < 1 mm diameter) from the Apollo 15 landing site for their inert gas contents. Grain size analysis was performed in order to understand how the inert gases are distributed among particles of different sizes up to 1 mm. Theoretical and analytical techniques were employed to separate the various components of the gases. Correlations and trends within a landing site as well as between sites was sought. These were compared in turn to other landing sites (Apollo 11, 12, 14, 16) in order to make generalizations.

I have also examined surface fines from the Apollo 17 landing site, and focused particular attention on fines from three depths in a trench at this site in an effort to understand what differences, if any, exist between particles not now at the surface and those at the surface at the time of collection. The trench was dug in the ejecta blanket of a 90 m diameter crater (Van Serg). An attempt was made to define the regolith surface that existed prior to deposition of the ejecta blanket.

II. SOURCES OF INERT GASES IN LUNAR SOILS

A. Radiogenic Components

1. Radiogenic He^4

Radiogenic He^4_R is produced by the natural radioactive decay of U^{238}, U^{235}, and Th^{232} according to the simplified decay scheme:

$$U^{238} \rightarrow Pb^{206} + 8\ He^4$$

$$U^{235} \rightarrow Pb^{207} + 7\ He^4$$

$$Th^{232} \rightarrow Pb^{208} + 6\ He^4$$

The total amount of He^4 produced after time t from the three decays may be expressed (units: atoms/g) as:

$$He^4_R = N_{238}\left[8(e^{\lambda_{238}t} - 1) + 7\left(\frac{U^{235}}{U^{238}}\right)(e^{\lambda_{235}t} - 1) + 6\left(\frac{Th}{U}\right)(e^{\lambda_{238}t} - 1)\right]$$

A typical value for U^{238} concentration in lunar soils is 1 ppm, therefore $N_{238} = 2.531 \times 10^{17}$ atoms/g. Common values for U^{238}/U^{235} and Th/U are 7.5×10^{-3} and 4.0, respectively.

Using the decay constants $\lambda_{238} = 1.540 \times 10^{-10}\ y^{-1}$, $\lambda_{235} = 9.72 \times 10^{-10}\ y^{-1}$ and $\lambda_{232} = 4.99 \times 10^{-11}\ y^{-1}$ and $t = 4.0 \times 10^{9}$ y, I obtain $He^4_R = 3.7 \times 10^{16}$ atoms/g.

Dividing by Lohschmidt's number 2.69×10^{19} atoms/cm^3 STP results in $He^4_R = 1.38 \times 10^{-3}$ cm^3 STP/g. The concentration of He^4 in bulk fines (soils with particle diameter < 1 mm) is typically 1×10^{-1} cm^3 STP/g and for coarse grains (~ 1 mm diameter) about 1×10^{-2} cm^3 STP/g. Thus 90 to 99% of the He^4 in bulk fines is nonradiogenic; its source is primarily from the solar wind although there is a small (negligible) contribution from cosmic rays (see section IIC).

2. Radiogenic Ar^{40}

The radioactive decay of K^{40} produces the stable isotope Ca^{40} by β^- emission, which accounts for 89% of the disintegrating K^{40} nuclei. The remaining 11% decay to Ar^{40} by K-capture. Just as the solar wind component masks radiogenic He^4_R, the radiogenic Ar^{40}_R in lunar soils is generally dominated by another component. This component is correlated with Ar^{36} which is almost purely solar wind derived (see II-C). Plots of Ar^{40} vs. Ar^{36} for size fractions of lunar soils generally result in a straight line with an Ar^{40} intercept value at $Ar^{36} = 0$ (see VI-B). This intercept value is interpreted to be radiogenic Ar^{40}_R for lunar soils, although it may represent the average of radiogenic Ar^{40}_R for particles with different apparent K^{40}-Ar^{40} ages.

B. Cosmic Rays

1. Galactic cosmic rays

The source of galactic cosmic rays is speculative, but they are apparently isotropic. Galactic cosmic rays are composed of ~ 85% protons, the remainder are α-particles, and < 2% heavier nuclei. These are the most energetic types of radiation (500 MeV to 100 GeV) to which objects in the solar system are exposed. The primary incident protons at the lunar surface interact with the nuclei of target elements in the lunar soil. Reaction products are produced by the spallation mechanism. The incident particle strikes the nucleus of the target element scattering one or more nucleons. The scattered nucleons (cosmic ray secondaries) will have relatively high kinetic energies and will interact with nuclei of other target elements. The struck nucleus has a very high residual energy which it loses by "boiling off" particles of low mass such as p, n, H^2, H^3, He^4, etc. The result is an internuclear cascade. The cosmic ray secondaries rapidly become the major interacting particles with increasing depth. The galactic cosmic ray production of any isotope does not increase monotonically with depth. The production of a given isotope passes through a maximum and then decreases. The decrease of production of a particular isotope is generally expressed in terms of half thickness (the depth at which production decreases by a fac-

tor of 2) which is a function of the composition of the target and the energy of the primary flux of protons. For production of inert gas isotopes in the lunar soil, the half thickness is ~150g/cm^2 or 75 cm (using a bulk soil density of ~ 2.0 g/cm^3).

Although all of the inert gases could be produced in this fashion, the major cosmogenic nuclides are He^3_C, Ne^{21}_C, and Ar^{38}_C (C≡cosmogenic). The production rate of these nuclides are a function of the composition of the target and specific equations for the production by primary protons and secondaries have been obtained by correlating inert gas measurements with chemical composition in the interior of meteorites and dividing by 2 to account for 2π irradiation of the lunar surface (Eberhardt et al, 1965; Hintenberger et al, 1964; Stauffer et al., 1962; Yaniv et al., 1971). These equations are:

$$He^3_C = 1.00[0.01179\ O + 0.572] \times 10^{-8} cm^3 STP/g \text{ per } 10^6 \text{ y}$$

$$Ne^{21}_C = 0.00347[2.2\ Mg + 1.35\ Al + Si + 0.17\ Ca + 0.017\ (Fe+Ni+Ti)] \times 10^{-8} cm^3 STP/g \text{ per } 10^6 y$$

$$Ar^{38}_C = 0.000597[16.5Ca + Fe + Ni + 2.5Ti] \times 10^{-8} cm^3 STP/g \text{ per } 10^6 \text{ y}$$

It is assumed by inert gas researchers that these equations are valid for lunar rocks and soils. For lunar soil compositions these are approximately 1 x 10^{-8}, 0.15 - 0.20, and (0.08 - 0.10) x 10^{-8} cm^3 STP/g per 10^6 y, respectively. From a large number of meteorite studies it has been deter-

mined that $(He^4/He^3)_C \sim 5.2$, $(Ar^{36}/Ar^{38})_C \sim 0.6$, and $(Ne^{20}/Ne^{21}/Ne^{22})_C = 1$. Thus the production rate of He_C^4 is about 5×10^{-8} cm^3 STP/g per 10^6 y, and in 4.0×10^9 y this amounts to 2×10^{-4} cm^3 STP/g, assuming continuous exposure to cosmic rays. This is a negligibly small quantity compared to observed concentrations of He^4 in most lunar soils. Similar exposure times would give rise to non-negligible amounts of He_C^3, Ne_C^{21}, and Ar_C^{38}, since the measured concentrations of He^3, Ne^{21}, and Ar^{38} in lunar fines are about 1×10^{-5}, 1×10^{-6}, and 1×10^{-5} cm^3 STP/g, respectively.

A more commonly determined exposure time for lunar soils is ~ 250 my, which would yield concentrations of about 2.5×10^{-6}, 5.0×10^{-7}, and 2.5×10^{-7} cm^3 STP/g for He_C^3, Ne_C^{21}, and Ar_C^{38}, respectively, in lunar soils which were within the depth of galactic cosmic ray production of these isotopes. The measured Ar^{36} is generally $1\text{-}2 \times 10^{-4}$ cm^3 STP/g. Using $(Ar^{36}/Ar^{38})_C = 0.6$, the calculated concentration of Ar_C^{36} is only about 1.5×10^{-7} cm^3 STP/g. The measured ratios Ne^{20}/Ne^{21} and Ne^{22}/Ne^{21} in lunar fines are generally ~ 400 and ~ 30, respectively. Assuming a concentration for Ne^{21} of 1×10^{-6} cm^3 STP/g, an exposure of 250 my, and $(Ne^{20}/Ne^{21}/Ne^{22})_C = 1$, the amounts of Ne_C^{20} and Ne_C^{22} would account for approximately 0.1% and 1% of the observed Ne^{20} and Ne^{22}.

2. Solar cosmic rays

Emitted during violent solar events, called solar flares, solar cosmic rays are mainly protons (with some α-particles and heavier nuclei) with energies up to several hundred MeV, but less than 10% have energies above 50 MeV. Because of their much lower energy compared to galactic rays, solar cosmic ray protons are generally stopped within the top few centimeters. Walton (1974) has studied the solar cosmic ray production of He, Ne, and Ar isotopes with depth below the lunar surface. He concludes that these production rates are at least comparable to galactic cosmic ray production rates to a depth of about 5 mm in the regolith, below which the production rates decrease rapidly.

C. Solar Wind

It has been well established that a steady stream of charged particles emanates from the sun. Collectively referred to as the solar wind, this plasma has velocities near the moon of 300 - 500 km/sec and temperatures of about 10^6 °K. The particle density is 2-10 cm^{-3}, and its composition is mainly protons and electrons. Prior to Apollo missions ions were detected by Mariner and Vela satellites carrying high resolution mass analyzers. The He/H ratio was determined to be variable with a range of 0.01 to 0.25; oxygen, silicon and iron were detected. Ion energies were

determined to be ~ 1 keV/nucleon. (Bame et al., 1968, 1970; Hundhausen et al., 1967; Ogilvie et al., 1968; Robbins et al., 1970; Snyder et al., 1964; Wolfe et al., 1966).

Since the moon essentially has no magnetic field it behaves like a passive obstacle to the solar wind. During a normal lunar day, the solar wind will strike the lunar surface with essentially unchanged energy. During the Apollo missions aluminum foils were deployed on the lunar surface and used as targets for collecting solar wind ions. Laboratory experiments have shown that ions with energy of 1 keV/nucleon will penetrate ~ 1000 Å of aluminum foil (Buchler et al., 1966, 1969; Geiss et al., 1969). In this way the aluminum foil trapped He, Ne, and Ar in measurable quantities. These solar wind ions were shown to arrive at the surface in a highly directional flow. Fluxes and elemental and isotopic ratios were determined (Geiss et al., 1969). Inert gas studies of lunar fines have revealed that lunar materials also trap solar wind ions in their surfaces. For this reason this component of the inert gases is sometimes referred to as the trapped component. About 90% of the gas contents of these fines may be attributed to implanted solar wind ions. The inert gas composition of the fines resembles that of the foil with good agreement for $He^4/He^3 \sim 2000$, $Ne^{20}/Ne^{22} \sim 13.0$, and $Ne^{22}/Ne^{21} \sim 30$. However, the elemental ratio of He^4/Ne^{20} and Ne^{20}/Ar^{36} differ greatly between lunar materials and the foil. The foil has

a ratio of $He^4/Ne^{20} \sim 550$, and $Ne^{20}/Ar^{36} \sim 30$, while the lunar materials have He^4/Ne^{20} ratios of 50 - 100 and a ratio of $Ne^{20}/Ar^{36} \sim 5$, which may be attributed to diffusion losses of He^4 and Ne^{20} from the regolith.

While most protons and other ions imbed themselves in the outer surfaces of lunar grains, some have a tendency to erode these surfaces. This effect, referred to as sputtering, is the result of collision of energetic solar wind protons and other ions with atoms composing the surface of the solid. The result is removal of the surface atom for atom by scattering. Thus, much of the history of the ancient solar wind in the surfaces of the grains must be erased.

III. DESCRIPTION OF EXPERIMENTS

A. Sample Preparation

All samples discussed in this work are referred to as fines. Most often the definition of the term fines is soil particles with dimensions less than 1 mm in diameter; however, the restriction is sometimes relaxed and references to 1-10 mm "coarse fines" in the Lunar literature are not uncommon.

The samples arrived at our laboratory in polyethylene MSC (Manned Spacecraft Center) vials. For cases in which bulk fines (fines which have not been altered experimentally by mineral or size separations) were to be analyzed, all or part of the sample was removed, depending on the quantity available and the quantity necessary for the experiment, and weighed on a Cahn electrobalance. Typical weights for bulk fines were restricted to about 1000 μg since their inert gas contents are relatively large. When grain size analysis was desired, a large enough portion of the bulk soil was chosen so as to yield experimentally useful weights for each size fraction, and was subsequently washed with acetone through standard mesh sieves with grid sizes of 63, 74, 88, 105, 250, 354, 500, and 700 μm. If mineral separation was desirable, size fractions were observed under a binocular microscope, the minerals were identified, and then hand picked for

weighing and packaging. After weighing, samples were wrapped in aluminum foil (known experimentally to have negligibly small inert gas contents) and loaded into the side arm of the preparation line.

B. Instrumentation

1. General description and theory

The instrument used for inert gas measurements was a Reynolds-type mass spectrometer shown in Figure 1 (Reynolds, 1956). It operates in a static mode with the valve to the ion pump closed rather than open as is done in the dynamic mode, and consequently has the high sensitivity necessary for inert gas measurements. It is enclosed in a pyrex glass envelope which can be baked to higher temperatures than most metal instruments, and with a suitable amount of baking, the pressure near the ion gauge (see below) may be as low as 5×10^{-11} mm Hg when the valve to the ion pump is open. The principle of its operation is as follows: neutral gas atoms to be measured are ionized in the source region by an electron beam. The ions pass through slits in a series of plates with a voltage drop V; they are collimated and accelerated. The ion beam which emerges through the final slit is a mixture of ions with different charge to mass ratios. The beam is subsequently "split" into several orbital paths of different radii by a 60^{o} sector magnetic analyzer whose field

lines are perpendicular to the plane of the ion beam. It is a well known result of electromagnetic theory that, under these conditions,

$$\frac{e}{m} = \frac{2V}{B^2 r^2}$$

where e = charge of the ion, m = mass of the ion, v = accelerating voltage, B = magnetic field intensity, and r = radius of the ion orbit. In the mass spectrometer r is restricted by the radius of curvature of the analyzer tube (4.5 inches in the Reynolds-type instrument) between the poles of the magnet. Hence, by varying the accelerating voltage V or the magnetic field intensity B, particular $\frac{e}{m}$ values may be scanned. For the instrument used in these experiments, V was fixed at 2 kilovolts and B was varied. Ions passing through the magnetic analyzer are detected by an ion collector. The signal is amplified and recorded on a strip chart.

2. Description of individual parts

Ion Source: The electron beam is produced by emission of electrons from a tungsten filament housed in the ionization chamber. The emission current, the current of electrons between the filament and the chamber walls, is maintained constant in the following way: There exists a potential difference between the chamber wall and the

filament (the electron voltage). When the trap current (the electron current measured at the wall of the ionization chamber) falls below a certain critical value the emission regulator electronically increases the current through the filament and, hence, the emission current. The electrons' energy may vary from 5 to 100 eV, for which single ionization efficiency is much greater than multiple ionization efficiency of the inert gases. There is, however, some double and higher order ionization which may influence the measurement of a particular mass m. For example, a beam of ions with e/m of + 1/20 will contain some ions with e/m of + 2/40. This becomes an important consideration in the measurement of Ne^{20} (see below, He and Ne measurement). After their formation, the ions are collimated and accelerated to energies up to 2 keV by a series of plates with slits.

Magnetic Analyzer: The magnetic analyzer is an electromagnet with opposite poles on either side of the analyzer tube whose field intensity is varied by adjusting the current through the coils. As can be seen from the mass spectrometer equation given above, increasing the current and thus B results in increasing the mass of ions allowed through the analyzer tube. The geometry of the magnet plays an important role in focusing the ion beam. If a beam containing a particular mass m enters the field of

a 60^{o} sector analyzer perpendicularly it will emerge perpendicular to the magnet. The same beam with a small angular spread will be refocused by the fringing fields of the magnet and converge on the collector slit. The ability to resolve one mass from another depends critically on this focusing property, the width of the source and collector slits, and the radius of curvature of the analyzer tube, since masses with orbital radii slightly divergent from the one of interest may be focused along with it. Mass resolution becomes more difficult with increasing mass since the difference in e/m values and hence r is less.

Ion Collector: The resolved ion beam arriving at the collector passes through a defining slit, and then impinges on the surface of the conversion dynode of a nine stage Be-Cu electron multiplier. At the conversion dynode ions produce secondary electrons which are focused and accelerated to a second dynode where a greater number of electrons are released and accelerated to the third dynode, etc. In this manner the small ion current may be magnified. The amount of magnification or gain is governed by the interdynode potentials, produced by passing a current (string current) through a series of resistors situated between each dynode. A string current of about 40 microamperes was passed through a series of 5 megaohm resistors to obtain an interdynode potential of 200 volts and a gain of

$\sim 10^3$ in the instrument used for these measurements. The last dynode collects all the secondary electrons and the current passes to a vibrating reed electrometer where it charges the plate of a capacitor whose plate distance oscillates, thereby changing the d. c. signal to a. c.. The a. c. signal passes through an input resistance of 10^{10} ohms resulting in a voltage drop which drives the output recorder.

Ion Gauge: The pressure in the mass spectrometer used in these experiments was measured with an ultrahigh vacuum ion gauge connected by pyrex glass tubing to the source and collector housings. This gauge consists of a filament and grid which, when operating in the "regulated" mode, has a current passing through the filament emitting electrons which ionize neutral gas atoms. The ion current thus produced is proportional to the pressure in the ion gauge, which is read in units of mm Hg. In the "regulated" mode the ion gauge also serves as a protective device for the source filament. When the pressure rises above some preset level (usually 5×10^{-4} mm Hg), the high voltages and the current to the source filament are shut off, to prevent oxidation of the filament. During measurements the pressure near the ion gauge is high compared to that existing when the valve to the ion pump is open, and there may be severe pumping effects, due to ion implantation into

the glass walls, resulting in gas loss during the measurement. For this reason the grid of the ion gauge is "floated" while measuring gas from a sample.

C. Inert Gas Analysis

1. Gas extraction technique

A schematic diagram of the sample preparation system is shown in Figure 1. A sample is transferred from the side arm to the water cooled quartz furnace by pushing it with a small tack (located in the prepline) which is set in motion by a hand-held magnet. Once in the furnace the sample rests in a molybdenum crucible. It is completely fused and gases are totally released by R. F. heating with an external coil, the principle of which is as follows: An alternating current through the copper coil surrounding the furnace must from Ampère's circuital law have associated with it an alternating magnetic field. From Faraday's induction law this changing magnetic field must induce an electric field in the region of a conductor, in this case the molybdenum crucible. The electric field induced sets the conduction electrons of the mulybdenum crucible in motion, and heat is generated by eddy currents. A temperature in the crucible of about 1500° C (determined with an optical pyrometer) is thus obtained with the R. F. power supply's plate and grid settings at 1.3 and 0.26 amperes,

respectively. To avoid having particles possessing surface charge jump out of the crucible, in the presence of a suddenly increasing magnetic field, heating was done in stages by beginning with a plate setting of 0.5 ampere and grid at 0.1 ampere for four minutes and then increasing the plate and grid currents at a rate of 0.01 amp/30 sec and 0.02 amp/30 sec, respectively, until the final settings were reached and maintained for 10 minutes. At this stage the gas is confined to a relatively small portion of the preparation line (i.e. the furnace and side arm) by two ultra-high vacuum valves, one to an ion pump and the other to the remainder of the system. At the end of the heating phase the gas is expanded to the remainder of the prepline (excluding the line to the standards) and allowed to equilibrate by opening the appropriate valve. Equilibration is complete in about 20 minutes and during this 20 minute period the gas is exposed to a Ti-Zr getter heated to about 900° C by a resistance furnace. The Ti-Zr getter removes hydrocarbons and other contaminants by reacting with them. At the end of 20 minutes the resistance furnace is turned off and hydrogen is absorbed on the surface of the Ti-Zr alloy. The system is now filled for the most part with the inert gases He, Ne, Ar, Kr and Xe from the sample plus small background amounts of these gases. Immediately after turning off the resistance furnace, liquid nitrogen in a dewar is placed around a charcoal trap. At liquid nitrogen

temperatures (- 180° C) charcoal is a very efficient absorber of the heavier inert gases Ar, Kr, and Xe. Within a period of 90 minutes after liquid nitrogen is placed around the trap these heavier gases are completely "frozen" on the charcoal. During this cooling phase, H_2 is gathered by the Ti-Zr alloy. At the end of 90 minutes, He and Ne isotopes are ready for measurement.

2. Measurements

He and Ne: Prior to admitting He and Ne the mass spectrometer is open to an ion pump through an ultra-high vacuum valve (V1). Shortly before the measurement of He^4 and He^3 the valve is closed and He^4 from the atmosphere diffusing through the pyrex glass envelope is monitored. The effect of such diffusion is a linear increase in the He^4 peak height at a rate of about 3 mv/min in the mass spectrometer and about 10 mv/min in the mass spectrometer + prepline, so that the absolute amounts of He^4 are obtained by drawing a line through successive peak tops back to the time of gas admission to the mass spectrometer, from which the atmospheric He^4 that accummulated in the mass spectrometer just prior to the admission must be subtracted. He and Ne were introduced by opening a valve separating the prepline from the mass spectrometer (V2) and the ion gauge is turned from regulated to float to prevent pumping. Only a fraction of the total gas was admitted to avoid having

to pump the mass spectrometer several times to get the rather large signal from He^4 to be within the 30 volt range, the maximum recorder scale setting. This is accomplished by closing a valve on the prepline side (V3) prior to admission, thereby isolating a small volume (i.e., the volume contained by V2, V3, and V5). The total signal may then be computed by multiplying the measured signal from the restricted volume + mass spectrometer by the volume ratio of the total prepline + mass spectrometer to the restricted volume + mass spectrometer. (See Appendix A for details.) Measurements of the millivolt signals of He^3, He^4, Ne^{20}, Ne^{21}, and Ne^{22} were thus obtained. In addition, peaks of three other masses were measured since they constituted corrections on the mass peaks of the rare gas isotopes. These were masses 18, 40, and 44. Mass 18 is predominately H_2O^{16}, but H_2O^{18}/H_2O^{16} is approximately 1/500; therefore, 1/500 of the mass 18 peak is equal to the amount of H_2O^{18} present which appears on the mass 20 peak. It has been determined experimentally that for mass spectrometers with operating conditions similar to the one used in this work that $Ar^{40++}/Ar^{40+} \simeq 1/6$. Although most of the Ar^{40} is "frozen out" on charcoal cooled by liquid nitrogen during the He and Ne measurement, a small equilibrium amount existing in a free state may be detected and 1/6 of this amount appears on the mass 20 peak due to double ionization. Hence to obtain the amount of Ne^{20},

1/500 of the mass 18 peak and 1/6 of the mass 40 peak were subtracted from the mass 20 peak. Mass 44, essentially CO_2, is in part doubly ionized and it has been determined that $CO_2^{++}/CO_2^{+} \simeq 1/70$. Thus 1/70 of the mass 44 peak equals the amount of CO_2^{++} that was subtracted from the mass 22 peak to obtain the amount of Ne^{22} present.

Argon, Krypton, and Xenon: After the measurement of He and Ne and the masses used for corrections, the valve connecting the mass spectrometer to the prepline (V2) was closed and the mass spectrometer was pumped. The valve (V3) separating the small prepline volume from the remainder was opened, the liquid nitrogen was removed from the charcoal trap and was replaced by hot water ($\sim 60^{\circ}$ C) resulting in the evolution of the heavier inert gases Ar, Kr, and Xe. Equilibration over the entire volume of the prepline is complete in about 30 minutes, and gas introduction to the mass spectrometer and subsequent measurement of Ar^{36}, Ar^{38}, Ar^{40}, Kr^{84}, and Xe^{132} was the same as for He and Ne, except for the low abundance isotopes, Kr^{84} and Xe^{132} ($\sim 10^{-8}$ cm^3 STP/g), for which total gas introduction was required. Therefore, Ar isotopes were measured first, perhaps with a restricted volume, and then the entire gas was admitted for the measurement of Kr^{84} and Xe^{132}.

Blank Runs and Calibrations: Before the measurement of a series of samples and at intervals between samples

(usually every four samples) blank measurements were performed in which all procedures were the same except that no sample was introduced into the crucible. The background millivolt signals from the gas thus obtained must be subtracted from the total signals found in the sample measurements. Typical blank gas contents are given in Table 1.

To obtain gas contents of the samples in units of cm^3 STP/g the sensitivity (mv/cm^3 STP) of the instrument must be determined. This was accomplished by admitting an accurately known quantity of He^3, He^4, Ne^{20}, Ar^{40}, Kr^{84} and Xe^{132} and measuring their millivolt signals. The gases were introduced into a small pipette from a standard reservoir, then admitted to the preparation line + mass spectrometer and allowed to equilibrate. The volumes and typical sensitivities used for calculations were:

Standard Volume (cm^3STP)	Sensitivity (mv/cm^3STP)
$He^3 = 8.943 \times 10^{-8}$	$S(3) = 3.221 \times 10^9$
$He^4 = 31.66 \times 10^{-8}$	$S(4) = 3.029 \times 10^9$
$Ne^{20} = 11.50 \times 10^{-8}$	$S(20) = 5.187 \times 10^9$
$Ar^{40} = 24.75 \times 10^{-8}$	$S(40) = 1.819 \times 10^{10}$
$Kr^{84} = 0.0839 \times 10^{-8}$	$S(84) = 3.062 \times 10^{10}$
$Xe^{132} = 0.0394 \times 10^{-8}$	$S(132) = 2.100 \times 10^{10}$

Masses 21 and 22 are measured less sensitively than mass 20 due to mass fractionation of these isotopes, so that sensitivities of masses 21 and 22 are obtained by dividing the sensitivity of mass 20 by experimentally determined fractionation factors for these isotopes (i.e., S(20)/S(21) = 1.005 and S(20)/S(22) = 1.01).

3. Calculations

Once total millivolt signals from an experiment have been determined and corrections have been made, the gas concentration (C) of a sample may be obtained from the following equation (units given in parentheses):

$$C\left(\frac{cm^3 STP}{g}\right) = \frac{NSMV\ (mv)}{WT(g) \times S\left(\frac{mv}{cm^3 STP}\right)}$$

where NSMV = net sample millivolt signal. From this relation the amounts of all the inert gas isotopes may be determined. Elemental and isotopic ratios are obtained by taking the ratio of the gas concentrations. For a more detailed analysis of the determination of NSMV and a discussion of errors see Appendix B.

IV. INERT GAS CONTENTS VERSUS GRAIN DIAMETER

A. Surface Correlation of Solar Wind Ions

1. Observations

The relatively low energy solar wind ions penetrate only to a depth of a few hundred to 1000 Å. Eberhardt et al. (1970) found that removing the surface of 41 μm ilmenite grains ($FeTiO_3$) by etching with HF resulted in ~90% decrease in gas concentration with ~ 5000 Å of the surface removed. Obviously, the ions after being stopped diffuse inward into the grain. Bibring et al., (1972) have revealed with an electron microscope that an amorphous layer, which is up to 1000 Å in thickness, appears on the surface of most lunar fines they have studied, and interpret this layer to be the result of radiation damage due to solar wind ion implantation.

A large number of studies of inert gas contents in grain size fractions of lunar fines have been performed (Baur et al., 1972; Bogard et al., 1971, 1973; Bogard and Nyquist, 1972a,b; 1973; Eberhardt et al., 1970, 1972; Eugster et al., 1973; Frick et al., 1973; Heymann et al., 1972, 1973; Heymann and Yaniv, 1970; Hintenberger et al., 1970, 1971; Hintenberger and Weber, 1973; Kirsten et al., 1970, 1971; Lakatos et al., 1973; Pepin et al., 1972; Podosek et al., 1971; Schaeffer et al., 1970; Walton et al., 1973; Yaniv and Heymann, 1971, 1972) and the salient obser-

vation is that the inert gas contents are roughly inversely proportional to the grain diameter (assuming particles are spherical), or C_i (cm^3 STP/g) α D^{-n} (C_i = concentration of isotope i, D = grain diameter). A perfect anti-correlation (n = 1) should be expected for a soil consisting of spherical grains of uniform density which have all been exposed to the solar wind for a length of time greater than or equal to the time required for surface saturation*, since the specific surface area of the soil (cm^2/g) is strictly proportional to D^{-1}. Eberhardt et al. (1970) found $0.82 \leq n \leq 1.15$ for ilmenite grains separated from the Apollo 11 bulk soil 10084 for which $0.58 \leq n \leq 0.65$. These investigators have found similar results for the fines 12001 from the Apollo 12 landing area (Eberhardt, 1972) and Hintenberger and Weber (1973) have found $0.83 \leq n \leq 1.15$ for breccias 10061 and 10021; $0.71 \leq n \leq 0.89$ for fines 15471; and $0.82 \leq n \leq 1.10$ for the orange and gray soil for the Apollo 17 landing site (74220 and 74241, respectively). Apparently, differences in mineralogy and rock types give rise to differences in trapping probabilities and gas retentivity properties. This and several other reasons why strict proportionality to D^{-1} does not exist in lunar soils, may be summarized as follows:

---

*Surface saturation is the limit of gas concentration at the surface of a particle, beyond which no more solar wind ions may be accepted by the surface without an equal amount of gas lost.

1 Soil grains are not spherical.

2 Constructional processes: (a) shock welding of soil particles due to micrometeorite bombardment gives rise to glass welded aggregates (agglutinates) which contain gas rich interior grain boundaries. (b) Formation of relatively coarse-grained particles by larger impacts (breccia formation) often results in the production of gas filled pore spaces.

3 Break up of larger grains would tend to dilute the gas concentration of the smaller grain sizes if the fresh material has not been irradiated since breakup.

4 Diffusive losses of lighter inert gases (He, Ne) while the heavier inert gases (Ar, Kr, Xe) are preferentially retained and diffuse inward, followed by further implantation, may lead to volume correlated amounts of the heavier inert gases.

5 Differences in mineralogy between size fractions may result in differences in the average trapping efficiency between size fractions.

6 Differences in surface residence times for different grain size fractions may lead to time-dependent gas concentrations which may be different for different size fractions.

2. Rosiwal Principle

Criswell (1975) has done a mathematical analysis of the sixth possibility by considering a cube of lunar soil

with one face exposed to the solar wind. The mass of fines in the size range r and r + dr, dm(r), will have an area, s(r), actually exposed to the solar wind. According to Criswell (1975) the soil particles in this range must obey the Rosiwal principle, which is

$$\frac{s(r)}{S} = \frac{dm(r)}{M}$$

where S = total area of one face of the cube and M = total mass of fines in the cube. Criswell (1975) subsequently fines an expression for the time dependency of gas concentration before saturation occurs to be

$$C_i(r,t) = f_i \cdot t / \gamma\rho\ (1 - p)\ L$$

where $f_i \equiv$ solar wind flux (cm^3 STP/cm^2 - yr), $\gamma \equiv$ fraction of soil particles with diameter < 1 mm, $\rho \equiv$ average density of soil particles, $p \equiv$ porosity of soil, $L \equiv$ the length of one side of the cube. It is notable that there is no dependence on grain radius r; thus, before surface saturation is achieved one should not expect an anticorrelation of gas concentration with grain radius or diameter. However, once surface saturation is achieved, grain size dependency occurs because surface saturated grains are unable to accept additional implanted ions.

A consequence of this model is that the larger grain size fractions achieve saturation more rapidly than the

smaller ones since larger grains spend a longer time at the lunar surface, on the average, than smaller grains. Thus, a plot of the log of gas concentration vs. log of grain diameter would result in a horizontal line in the smaller grain sizes which, at some critical diameter (D_c), will turn downward with n = 1 for the largest grain size fractions ($D > D_c$). As exposure continues D_c decreases until all size fractions have been saturated.

The model described does not take into account constructional and destructive processes (2 and 3 above). Constructional processes (eg. agglutinate formation) will tend to make the larger grain sizes more gas rich than predicted by simple surface saturation. Destructive processes (eg. particle comminution by micrometeorite bombardment) will tend to dilute the gas contents of smaller grain sizes if the particles being fractured contain surface correlated gas only and will tend to enrich the gas contents of the smaller grain sizes if the original grains contained large volume correlated amounts of gas prior to fragmentation. Superimposed on these processes is perhaps still another phenomenon proposed earlier by Criswell (1972), levitation of lunar dust grains by a local electric field. The levitating field E is produced about partially illuminated rocks at the terminator. Soft solar X-rays (energy > 500 eV) will eject photoelectrons from the sunlit side of the rock until a sufficient positive charge remains to

retain newly ejected photoelectrons, and a fraction of the ejected photoelectrons will accrete on the dark areas of the rock. Conditions for levitation are satisfied when the electrical force on charged grains exceed the gravitational force, i.e.

$$QE > \frac{4}{3} \pi r^3 \rho g$$

where Q is the charge on a grain of radius r, ρ is the mass density of the grains, g is the lunar gravitational acceleration, and E is the surface electric field. Because of the dependence on grain radius r, the mechanism will tend to selectively levitate the smallest grains. Criswell (1972) further suggests that the smallest grains will have enhanced exposure to the higher energy solar wind ions and solar cosmic rays since levitation is enhanced when the sun is active. Since the particles are dispersed above the lunar surface, all equally exposed to the solar wind, inert gas ions whose penetration depth is less than r should become surface correlated immediately. Thus, while the larger grain size fractions are becoming saturated according to the Rosiwal principle, the smaller grain sizes may become saturated due to levitation thereby shortening the time for the entire soil to become saturated.

B. Inert Gas Contents in Fines from the Apollo 15 Landing Site

A planimetric map of the Apollo 15 landing site appears in Figure 2. There are three morphologically distinct settings: the sloping Apennine Front (south of the dashed line), the flat Mare surface (north of the dashed line), and Hadley Rille (Rima Hadley).

The inert gas contents, elemental and isotopic ratios of five Apollo 15 soils are given in Table 2. For two of the fines from this site (15421, station 7; 15071, station 1), I have plotted the inert gas contents versus grain diameter (Figure 3). Neither sample displays the perfect anticorrelation with n = 1 predicted by the simple trapping mechanism. Considering only 15421, there is an absence of surface correlation and obvious irregularities in the larger grain size fractions. The irregularities also become slightly more pronounced in the direction of the heavier inert gases Ar^{36}, Kr^{84}, and Xe^{132}. Soil 15421 contains in addition to the mineralogical and petrological constituents found in most lunar soils (feldspar, olivine, pyroxene, and basalt fragments) a large percentage of green glass spherules. Jordan et al. (1974) have shown that the He^4/Ne^{20} ratio in Apollo 15 samples is correlated with the green glass content and fines 15421 with $He^4/Ne^{20} \sim 20.0$ was estimated to contain ~ 60% green glass. Lakatos et al.

(1972) have shown that green glass spherules from the "clod"* 15426 (Station 7) also have a high Ne^{20}/Ar^{36} ratio in the range 10-20, while the fines of this study (with the exception of 15421) and the work of Jordan et al. (1974) have an average Ne^{20}/Ar^{36} ratio of about 5. The size fractions of 15421 have an average Ne^{20}/Ar^{36} ratio of 7.70, reflecting the green glass content. Lakatos et al. (1973) conclude from the low gas contents of the 15426 green glass "clod" (two orders of magnitude less trapped gas than other bulk fines from the Apollo 15 site) and the lack of surface correlation of the inert gases, that the green glass spherules composing the "clod" have never been exposed to the solar wind. They suggest that the glass spherules acquired their gas during their formation from an ambient gas phase and that this gas is volume correlated. Following their formation the green glass was buried rapidly and shielded from further exposure to the solar wind, thus explaining the lack of grain size dependency of the inert gas contents. Formation in the presence of a hot gas phase is supported by the low He^4/Ne^{20} ratio of the green glass (< 10 compared to $\gtrsim 40$ for other fines from the site) which suggests that He^4 has been lost relative to Ne^{20} by thermal diffusion.

An alternative explanation would be that irregulari-

---

* a friable aggregate of green glass spherules

ties in the gas contents versus grain diameter curves merely represent the pre-saturation solar wind gas loading of the different size fractions. Frick et al. (paper to be published) have studied feldspar, olivine + pyroxene, and green glass separates in size fractions of 15421 fines and their inert gas data for the feldspar and olivine + pyroxene display a reasonably good anticorrelation with grain size. Thus the data displayed in Figure 3 for the combined materials of 15421 must mainly reflect the green glass content. The increased irregularity of this data in the direction of the heavier inert gases may then reflect the phenomena of undersaturation. That is, one would expect that prior to saturation an inert gas with a relatively low flux (eg. Xe^{132}) will display a gas concentration versus grain diameter pattern at time t_o similar to that which would have been displayed by an inert gas with higher flux (eg. He^4) at some earlier time $t < t_o$. As the exposure time increases the irregularities will tend to "smooth out" due to particle comminution and construction and continued solar wind irradiation, n values will increase toward unity more rapidly for the lighter gases with higher fluxes, and after some time, t_s, even the heaviest inert gases with the lowest fluxes will saturate most grain surfaces. Criswell (1975), assuming the Rosiwal principle is valid, has determined the time required for Xe^{132} to saturate surface grains of radii down to $r = 4\ \mu m$ for the bulk sample 10084 from the

Apollo 11 landing site to be $t_s \simeq 72$ my (the effect of particle levitation is neglected). He notes that this time is a factor of six longer than one would calculate on the basis of the average concentration of Xe^{132} in the size fractions.

Figure 3 also shows gas content versus grain diameter for fines 15071 from Station 1. Three observations are notable: 1 There is a fair anticorrelation with grain diameter. One size fraction (250-354 μm) deviates more strongly than the remainder, especially with respect to Ar^{36}. It has the lowest He^4/Ne^{20} ratio (30.18) and the highest Ne^{20}/Ar^{36} ratio (5.224) compared to the remaining size fractions, implying an enrichment of green glass in this size range. 2 The n values are less than unity ($0.32 \leq n \leq 0.56$). 3 The n values have the following trend: $n_4 > n_{20} > n_{36} > n_{84} > n_{132}$ (subscripts refer to mass). Values of n which display this trend as well as other variations have been reported by many investigators (Bogard et al., 1974; Eberhardt et al., 1972; Hintenberger and Weber, 1973; Heymann et al., 1975). I have summarized these n values in Table 3. The most salient feature of most lunar soils listed is a trend of decreasing n values with increases in mass. Two of the exceptions - 10021 and 10061 - are breccias, which have relatively high n values (10021, $n > 1$) which tend to decrease with mass up to Ar^{36} (10021) or Kr^{84} (10061) and then increase in the direction of higher masses. The il-

menite of breccia 10046 also displays this behavior in a more pronounced manner. Apparently, the departure from the usual trend is connected with breccia formation. Precisely what physical processes gave rise to the behavior of the n values of 10021, 10061 and 10046 could not be resolved in this study.

The general trend of $n_4 > n_{20} > n_{36} > n_{84} > n_{132}$ may be the consequence of the Rosiwal principle on which the effects of comminution and agglutinate formation are superimposed. It follows from the Rosiwal principle that the critical diameter (D_c), at which the slope of the curve changes from horizontal to 45° downward in a log C vs. log D plot, viewed at any instant, will be larger for successively heavier gases (since their flux is less). Thus, if it were not for the effects of comminution, the gas contents versus grain diameter curve could be expressed as two equations: $C=K$ ($D<D_c$, $n=0$) and $C(D) = KD^{-n}$ ($D>D_c$, $n=1$). The effect of comminution by micrometeorites is to add fractured grains from larger grain size fractions to smaller grain size fractions. A certain percentage δ (with respect to the original grain size) of a newly formed grain will be saturated if the original grain had $D > D_c$ (eg. a saturated sphere broken into two identical half spheres will produce two particles each of which is 67% saturated). If the grain size fractions to which the recently formed grains are added has diameters > D_c, then addition of grains to these size fractions by comminution can only result in the decrease of the gas concentra-

tion. However for $D < D_c$, grains in each size range are undersaturated to a successively lesser extent as $D \rightarrow D_c$ from below. Another way of stating this is that there is a certain percentage Φ of the surfaces saturated in the undersaturated grains, and that Φ increases as $D \rightarrow D_c$ from below. Thus, if $\delta > \Phi$ for a grain entering a size range characterized by Φ, then the addition of this grain to the size fraction results in an increase in gas contents of this size fraction. The effect of agglutinate formation is to create larger grains from smaller ones by shock welding due to micrometeorite impact. If grains of diameter $D < D_c$ are welded together to form new grains with diameter $D < D_c$, then the curve does not change slope in this region. However, if grains of diameter $D < D_c$ are welded together to form new grains with diameter $D > D_c$, then there will be an increase in gas concentration in the size fraction containing these recently formed grains. The same result will occur if the original agglutinate-forming grains have $D > D_c$. The net result of <u>both</u> the effect of comminution and agglutinate formation working simultaneously is to smooth out the curve defined by the equations $C = K$ ($D < D_c$, $n = 0$) and $C(D) = KD^{-n}$ ($D > D_c$, $n = 1$) so that the curve may be defined by a single equation $C(D) = KD^{-n}$ ($0 < n < 1$). The value of n should be smaller for larger values of D_c, or, in terms of inert gases, for heavier gases.

V. COSMIC RAY EXPOSURE AGES

A. The Eberhardt Plot

Cosmic ray exposure ages may be calculated, in principle, from any of the three major cosmogenic nuclides - He_C^3, Ne_C^{21}, Ar_C^{38}. However, He_C^3 and Ar_C^{38} are often masked by their trapped component and ages calculated from these isotopes are sometimes negative. Thus, I have only determined Ne_C^{21} and the resultant exposure ages for the fines in this work. The measured amounts of Ne^{21} and Ne^{22} may be expressed as the sum of their respective trapped and cosmogenic components, i.e.

$$Ne_m^{21} = Ne_T^{21} + Ne_C^{21}$$

$$Ne_m^{22} = Ne_T^{22} + Ne_C^{22}$$

Using these relations and substituting the identities $Ne_T^{21} = (Ne^{21}/Ne^{22})_T \, Ne_T^{22}$ and $Ne_C^{22} = (Ne^{22}/Ne^{21})_C \, Ne_C^{21}$ the expression for Ne_C^{21} becomes

$$Ne_C^{21} = \frac{(Ne^{22}/Ne^{21})_T \, Ne_m^{21} - Ne_m^{22}}{(Ne^{22}/Ne^{21})_T - (Ne^{22}/Ne^{21})_C}$$

For the calculations used in this work I adopted $(Ne^{22}/Ne^{21})_C = 1$. This value has been established by many investigators from studies of meteorites and lunar samples. It

was necessary either to assume a trapped ratio $(Ne^{22}/Ne^{21})_T$ or to determine its value from the method of Eberhardt et al. (1970) illustrated in Figure 4. The theory of the method is as follows:

1 The above equation for Ne^{21}_C may be rearranged, obtaining the equation

$$\left(\frac{Ne^{22}}{Ne^{21}}\right)_m = \frac{Ne^{21}_C}{Ne^{21}_m}\left[\left(\frac{Ne^{22}}{Ne^{21}}\right)_C - \left(\frac{Ne^{22}}{Ne^{21}}\right)_T\right] + \left(\frac{Ne^{22}}{Ne^{21}}\right)_T$$

If the Ne^{21}_C contents, and the $(Ne^{22}/Ne^{21})_C$ and $(Ne^{22}/Ne^{21})_T$ ratios are the same for all size fractions, then a plot of $(Ne^{22}/Ne^{21})_m$ vs. $1/Ne^{21}_m$ will define a straight line with a slope equal to $Ne^{21}_C[(Ne^{22}/Ne^{21})_C - (Ne^{22}/Ne^{21})_T]$ and intercept equal to $(Ne^{22}/Ne^{21})_T$.

2 Points which are below the line thus defined contain more Ne^{21}_C than those which are on the line, and vice versa.

3 Lunar materials containing no Ne^{21}_C will plot along a horizontal line which intersects the $(Ne^{22}/Ne^{21})_T$ intercept.

4 Lunar materials containing no trapped Ne will plot along a horizontal line which intersects $(Ne^{22}/Ne^{21})_C = 1$.

B. Cosmic Ray Exposure Ages of Apollo 15 Soils

Using the method of Eberhardt et al. (1970), I have

determined $(Ne^{22}/Ne^{21})_T$ from size fractions of 15071, 15091, and 15601 by standard regression calculations. Samples 15091 and 15601 are from station 2 and 9A respectively (see Figure 2) and data for size fractions were obtained from previous work (Jordan et al., 1974) and from the work of Heymann et al. (1972). The results of the linear best fits are shown in Figures 5, 6, and 7. The errors given for $(Ne^{22}/Ne^{21})_T$ are the standard deviations of the least square fits plus 50 per cent of the typical analytical error of an individual measurement, following the method of Eberhardt et al. (1970). Attempts to fit the data of 15501, 15511, and 15421 were less successful because of scatter of the points. However, 15501 and 15511 come from station 9 which is near station 9A from which 15601 fines were collected; therefore I used the $(Ne^{22}/Ne^{21})_T$ value of 15601 for 15501 and 15511. In the case of 15421 from station 7 there is no $(Ne^{22}/Ne^{21})_T$ value reported in the literature from this or neaby stations. The trend of the Eberhardt plot for 15421 suggests $(Ne^{22}/Ne^{21})_T > 30$ (the linear best fit for 15421 gave $(Ne^{22}/Ne^{21})_T \simeq 35$, although the correlation coefficient was low), therefore I adopted the ratio from 15071 of $(Ne^{22}/Ne^{21})_T = 32.52 \pm 0.52$ for calculation of Ne_C^{21} for 15421. Had I assumed a smaller $(Ne^{22}/Ne^{21})_T$ ratio the calculated Ne_C^{21} would be smaller. Some size fractions (15071, 427 μm, 600 μm; 15091, 427 μm; 15601, 427 μm) deviated considerably (~ 10%) from the lines defined by all the data

points. These were purposely omitted for the best fits shown in Figures 6, 7, 8. This is justifiable in that these size fractions may have had a distinctly different exposure history with respect to cosmic rays.

The Ne^{21}_C ages were determined from the Ne^{21}_C contents and the Ne^{21}_C production rate equation,

$$Ne^{21}_C = 0.00347[2.2(Mg) + 1.35(Al) + Si + 0.17(Ca) + 0.017(Fe + Ni + Ti)] \times 10^{-8} cm^3 \text{ STP/g per } 10^6 yr$$

from Yaniv et al. (1971). The compositions used are an average of data from four Apollo 15 fines (Table 4) taken from LSPET (1972). The resulting production rate was $Ne^{21}_C = 0.164 \times 10^{-8} cm^3$ STP/g per 10^6yr. The Ne^{21}_C contents and resulting cosmic ray exposure ages are listed in Table 5. The errors in Ne^{21}_C and the resulting ages for the smallest grain size fractions (up to 74 μm) are quite large (cf. 15091, < 44 μm error is 125%). This is principally due to the fact that these size fractions are dominated by trapped Ne so that $(Ne^{22}/Ne^{21})_m \rightarrow (Ne^{22}/Ne^{21})_T$, and the Ne^{21}_C errors are proportional to $[(Ne^{22}/Ne^{21})_T Ne^{21}_m - Ne^{22}_m]^{-1}$. Also it is notable that determined ages are sensitive to the choice of $(Ne^{22}/Ne^{21})_T$ and production rate for Ne^{21}_C. For example, if I had chosen $(Ne^{22}/Ne^{21})_T = 27.43$ (determined from 15601) for the calculation of Ne^{21}_C in size fractions of 15421 the Ne^{21}_C contents and ages would be lower by 21% to 42%. A difference of ± 0.01 from the adopted

Ne^{21}_C production rate would result in a difference of 6% in Ne^{21}_C contents and ages. The most reliable ages are generally determined from the largest grain size fractions, if they have low $(Ne^{22}/Ne^{21})_m$ ratios, since these are least sensitive to choices of $(Ne^{22}/Ne^{21})_T$ ratios. Caution must be exercised for these size fractions also. For example, the > 500 μm fraction of 15080 was split into two separates, magnetic and non-magnetic (work done by Dr. J. T. Wasson and coworkers). It is known that the magnetic portion is much enriched in agglutinates containing metal (Goldstein et al., 1974; Housley et al., 1972). Agglutinates comprise ~ 60% of 15080 (Carr and Meyer, 1972). The magnetic separate is characterized by a much greater trapped gas content compared to the non-magnetic separate (see Table 2). The determined Ne^{21}_C content of the magnetic separate is almost an order of magnitude less than the non-magnetic separate. This is only apparent, however, and is a consequence of the large trapped gas contents of this separate which essentially masks the relatively small cosmogenic component. Thus, if one had determined the Ne^{21}_C for the magnetic and non-magnetic separates combined in the proportions in which they occur in the soil, it would be

$$(Ne^{21}_C)_{combined} = 0.6(Ne^{21}_C)_{magnetic} + 0.4(Ne^{21}_C)_{nonmagnetic}$$

Using the values for $(Ne^{21}_C)_{magnetic}$ and $(Ne^{21}_C)_{nonmagnetic}$

given in Table 5, this would be $(Ne^{21}_C)_{combined} = 3.42 \times 10^{-7}$ cm^3 STP/g. Dividing by the production rate of 0.164 x 10^{-8} cm^3 STP/g per 10^6 yr, I obtain an exposure age of ~ 210 my, a factor of two below the age calculated for the non-magnetic separate. It is interesting to compare the age of the non-magnetic fraction of 15080, 450 my, with that of the 500-700 μm fraction of 15071 from the same station (station 1) after correcting the Ne^{21}_C contents of 15071 for the agglutinate content. This requires the assumption that the apparent Ne^{21}_C contents of the agglutinates in 15071 is the same as the non-magnetic fraction of 15080 and that the agglutinates occur in the same proportions in all size fractions. Powell et al. (1973) determined the soil breccia + agglutinate contents of 15071 to be ~ 30%. Assuming 30% agglutinates, I then obtain for the 500-700μm size fraction of 15071 a $Ne^{21}_C = 8.00 \times 10^{-7}$ cm^3 STP/g yielding a Ne^{21}_C exposure age of 490 my as against 360 my before correction, in good agreement with the 450 my exposure age of the > 500 μm size fraction of 15080.

The Ne^{21}_C ages represent an average of a range of exposure times and depths below the surface for all particles within a size range. Since the irradiation history of a soil is not known, relative age differences are more meaningful than absolute values as such. Fines 15091, 15421, and 15511 have age agreements among their respective size fractions within the errors given, and average ages which

are as follows: 15091, 195 my; 15421, 470 my; and 15511, 280 my. The age of 15421 agrees well with Kirsten et al. (1972), who found an age of 460 ± 60 my. Fines 15071, 15501, and 15601 all contain some size fractions whose exposure ages are discordant. Fines 15071 show an average exposure age of ~ 250 my for size fractions up to 354 μm, but the 354-500 μm and 500-700 μm size fractions have an average exposure age of 370 my. This sample was collected 25 m east of the rim of Elbow Crater (Swann et al., 1972) which is adjacent to Hadley Rille (see Figure 2). The 354-500 μm size fraction of sample 15601 collected from station 9A, 20 m east of Hadley Rille, has an exposure age of 370 my compared to 230 my for the remaining size fractions.

The regolith near the rim of Hadley Rille (in particular station 9A) is known to be very thin or absent, and the underlying material has been proposed to be a poorly comminuted basaltic zone (Swann et al., 1972). Elbow Crater - which is ~ 50 m deep (Swann et al., 1972) - must have sampled this zone. Since 50 m is well below the depth of Ne^{21}_C production, one would expect that coarse ejecta from Elbow Crater would have relatively low Ne^{21}_C contents. If the 354-500 μm and 500-700 μm size fractions of 15071 are dominated by coarse ejecta from Elbow Crater, then their Ne^{21}_C contents are contrary to this expectation. I see the same relationship in the 354-500 μm fraction of 15601.

This can be taken as evidence that there exist zones at some depth in the regolith which have considerable exposure to cosmic rays prior to deposition of the soil cover above them. I have already shown that the coarse fraction (> 354 μm) of 15071 may have an exposure age comparable to the 450 my exposure age of the > 500 μm non-magnetic fraction of 15080 from station 1, if one corrects for agglutinates. It is notable that the 250-500 μm fraction of 15601 contains ~ 50% agglutinates (Heiken, 1974) and thus may also have an age of 410 my (370 ± 40 my, see Table 5) or greater. The relatively old cosmic ray age of these zones is further supported by the exposure age of the mare type basalt 15556, which is thought to represent the local bedrock (Swann et al., 1972). Kirsten et al. (1972) found a Ne^{21}_{C} exposure age of 525 ± 40 my for this rock. The younger ages of the soil cover implies that it cannot merely be the result of comminution of this strongly irradiated, old material only, but must come from other sources as well, which are younger with respect to cosmic rays, such as material thrown out by large impacts on the Apennine Front as suggested by Hübner et al. (1973). St. George Crater near the base of the Apennine Front (Figure 2) is definitely the result of such a large impact. Its diameter is greater than 2 km (Swann et al., 1972). Two samples, 15091 and 15101, collected at station 2, located on the northeastern flank of St. George Crater,

indeed have relatively young exposure ages of 195 my (average of size fractions of this work) and 90 my (LSPET, 1972), respectively. Apparently the fines 15071 contain, at least in the finest fraction, material from St. George Crater. The much older age of the coarsest size fractions suggests that the Elbow Crater event penetrated below the flank deposits of St. George Crater.

Sample 15501 (as well as 15511) was collected at station 9, 10 m from a 10 m diameter fresh crater which is 300 m from Hadley Rille and 75 m south of the rim of Scarp Crater (250 m diameter) and about the same distance southwest of a younger, unnamed crater having the same diameter as Scarp. Thus, the young 10 m crater is presumed to be located on the ejecta blankets of the two larger ones (Swann et al., 1972). The average exposure age of size fractions of 15501 up to 700 μm is 310 my, while the > 700 μm size fraction has an exposure age of only 150 my. One possible explanation of the discordancy in age is that the small crater has merely re-excavated debris thrown out of the two larger craters, the ejecta blankets of which may be mixtures of both young and old materials with respect to cosmic rays. The youngest, > 700 μm, material may represent ejecta from the two larger craters which came from a depth below the heavily irradiated zone. Thus, if agglutinate content has not reduced ages significantly, and the > 700 μm size fraction of 15501 represents coarse,

poorly irradiated ejecta from the two large craters, the 150 my exposure age may place an upper limit on their formation. However, an agglutinate content of ~ 56% is reported for 15501 (Carr and Meyer, 1972) and it is conceivable that this upper limit would be increased if the exposure ages were determined for a non-agglutinate (non-magnetic) separate of these fines.

VI. Ar^{40}-Ar^{36} CORRELATIONS

A. The Problem of Excess Ar^{40}

The observed Ar^{40}/Ar^{36} ratios in lunar fines from all Apollo and Luna sites ranges from about 0.15 to about 10.0. These values are far greater than the theoretically predicted solar value of Ar^{40}/Ar^{36} which is $\sim 10^{-4}$ (Cameron, 1968). Furthermore, if one assumes that all Ar^{40} in the fines is radiogenic and calculates age from the K^{40}-Ar^{40} age equation

$$t = \frac{1}{\lambda} \ln \left[1 + \frac{Ar^{40}}{K^{40}} \left(\frac{1 + R}{R} \right) \right]$$

($\lambda = \lambda_\beta + \lambda_K$, $R = \lambda_K/\lambda_\beta$, $K^{40} = 0.000119$ K) one usually arrives at ages greater than the most widely accepted formation age of the solar system, ~4.5 by. For example, the Ar^{40} content of the Apollo 15 sample 15091 was found to be 3.36×10^{-4} cm^3 STP/g (Jordan et al., 1974) and the K content was determined to be 1380 ppm (Wänke et al., 1972). Using $\lambda = 5.304 \times 10^{-10}$ y^{-1} and $R = 0.1237$ ($\lambda_\beta = 4.72 \times 10^{-10}$ y^{-1}, $\lambda_K = 0.584 \times 10^{-10}$ y^{-1}) I obtain $t = 6.60$ by. Thus, there is an excess of Ar^{40}.

B. Diagrams of Ar^{40} versus Ar^{36}

Heymann and Yaniv (1970) found that by plotting Ar^{40} vs. Ar^{36} for size fractions of 10084 a good correlation

resulted, defined by the equation

$$Ar^{40} = 1.06Ar^{36} + (7.12 \pm 1.09) \times 10^{-5} cm^3 STP/g.$$

They conclude that since Ar^{36} is surface correlated that the excess Ar^{40} is also surface correlated with $Ar^{40}/Ar^{36} = 1.06$ and that the intercept value represents the volume correlated component of Ar^{40}. This volume correlated component is interpreted as radiogenic Ar^{40} from *in situ* decay of K^{40} if the K content of all size fractions is the same and if they all have the same K^{40}-Ar^{40} age. The surface correlation implies that the presence of the excess Ar^{40} could be somehow related to solar wind processes. Heymann and Yaniv (1970) propose the following:

1. The source of the excess Ar^{40} is from K^{40} decay within the interior of the solid moon.
2. The Ar^{40} is released into the atmosphere of the moon by heating of the lunar interior or by large scale melting processes near the surface.
3. Since neutral Ar^{40} atoms have lifetimes against gravitational escape of about 10^8 y (Bernstein *et al.*, 1963) they are gravitationally bound and their concentration above the lunar surface will be given by a Boltzman distribution

$$n(z) = n_o e^{-z\ mg/kT}$$

$(n(z))$ ≡ the concentration at height z above the surface, n_o = concentration at the surface, m = mass of Ar^{40}, g = lunar gravitational acceleration, k = Boltzman's constant). The e-fold or scale height occurs for $z = kT/mg$, which is 50 km for the sunlit side of the moon ($T = 400°K$).

4 However, the lifetime against ionization via charge exchange with solar wind protons and by photoionization is only $\sim 10^6$ seconds and Ar^{40} neutrals with 10^2 $cm^{-3} < n_o < 10^3$ cm^{-3} have ~ 10% probability of photoionization (Manka and Michel, 1970, 1971).

5 Once formed, the ions will be in the presence of the 10γ (at 1 a.u.) interplanetary magnetic field $\underset{\sim}{B}_{SW}$ which has associated with it an electric field $\underset{\sim}{E}_{SW}$ produced by the solar wind moving with a velocity $\underset{\sim}{V}_{SW}$ through a stationary magnetic field. The ion will experience a Lorentz force $q\underset{\sim}{E}_{SW} = -q\underset{\sim}{V}_{SW} \times \underset{\sim}{B}_{SW}$ and will execute a cycloidal orbit. The initial motion is along $\underset{\sim}{E}_{SW}$, and since the cyclotron radius ($\sim 10^4$ km) is much greater than the scale height of 50 km, the Ar^{40} ion deviates only slightly from parallel to $\underset{\sim}{E}_{SW}$ before impacting on the lunar surface.

Manka and Michel (1971) have calculated the ion trajectories and conclude that for $\underset{\sim}{E}_{SW}$ pointing in the direction of the north pole, ions formed at the south pole will be implan-

ted with an energy of only 200 eV, while ions formed -10° below the selenographic equator (taken to be the same as the electric equator) will be implanted about 7° above the equator with energies up to 2 keV. The direction of $\underset{\sim}{B}_{SW}$ reverses periodically, and thus $\underset{\sim}{E}_{SW}$ will be pointing toward the south pole half of the time, implanting ions in the southern hemisphere. The flux of Ar^{36} is parallel with $\underset{\sim}{V}_{SW}$ and thus arrives at the lunar surface at an angle near 90° to the reimplanted Ar^{40}. Thus the Ar^{40}/Ar^{36} arriving at the lunar surface is very sensitive to local topography. In an earlier work (Jordan et al., 1973) I argued in favor of local topographic variations accounting for variations in the Ar^{40}/Ar^{36}. In particular I claimed that the north sloping Apennine Front was exposed to a larger flux of Ar^{40} ions relative to Ar^{36} than the same on the flat lying Mare terrain. The observed higher Ar^{40}/Ar^{36} ratios on the Front seem to confirm this hypothesis.

The Ar^{40}/Ar ratio arriving at the lunar surface also reflects the concentration of neutral Ar^{40} in the lunar atmosphere relative to the solar wind flux. Yaniv and Heymann (1972) have suggested that the neutral concentration of Ar^{40} decreased between 4.0 and 3.0 by ago and cite as evidence a correlation between rock ages from Apollo 11, 12, 14 and Lunar 16 and the Ar^{40}/Ar^{36} ratios in fines from these sites. Thus older rock ages representing earlier onsets of regolith formation are associated with higher Ar^{40}/Ar^{36} ratios. The

Apollo 15 site is consistent with this trend. The mare crystalline rock ages are about 3.30 by; whereas the Apennine Front rocks have dates similar to 15415 of 4.09 by (Schaeffer et al., 1972). Hence the Front fines may be "older" in the sense that they acquired much of their Ar^{40}/Ar^{36} ratio at a time when the neutral concentration of Ar^{40} was higher, and the "younger" mare fines may have acquired their Ar^{40}/Ar^{36} ratios when the neutral concentration of Ar^{40} was less. The two explanations for the observed Ar^{40}/Ar^{36} ratios need not be considered mutually exclusive. Fines around at a time when the neutral Ar^{40} concentration was higher were exposed to a larger Ar^{40} flux independent of topography but superimposed on this there must be slope effects. It is doubtful, however, that the effect of local topography on Ar^{40}/Ar^{36} variations survives very long without being erased or smeared out by impacts.

C. Ar^{40} versus Ar^{36} for Apollo 15 Fines

I have plotted Ar^{40} versus Ar^{36} for size fractions of 15071, 15421, 15511 and 15501 which are shown in Figures 8, 9, 10 and 11. Inspection of these figures reveals that each sample has a rather unique history with respect to Ar^{40} intercept and the Ar^{40}/Ar^{36} ratio trapped in its surfaces; therefore, I shall discuss the samples individually:

15071, Station 1: This sample displays a good correlation between Ar^{40} and Ar^{36} (Figure 8), the equation of the line is $Ar^{40} = 0.792\ Ar^{36} + 0.140 \times 10^{-4}$ cm^3 STP/g.

The trapped ratio $(Ar^{40}/Ar^{36})_T = 0.792$ is typical of other mare fines in the landing area (average of Ar^{40}/Ar^{36} for mare bulk fines from Jordan et al., 1974 and size fractions of 15601 from Yaniv and Heymann, 1972, is 0.73), but the Ar^{40} intercept of 0.140×10^{-4} cm^3 STP/g is lower than one would expect for fines which formed from the comminution of rocks whose formation age is about 3.3 by (age from Schaeffer et al., 1972), and a K content of about 1000 - 1500 ppm, typical of fines from this site. No K content is given for fines 15071 but I have estimated it to be 1141 ppm assuming a constant Na_2O/K_2O ratio, from the Na_2O contents of 15071 (Fruchter et al., 1973) and the Na_2O and K_2O contents of 15081 from the same station (Wänke et al., 1972). Yaniv and Heymann (1972) have found a gross correlation between K contents and $Ar^{40}_{intercept}$ values based on the apparent K^{40}-Ar^{40} ages of several lunar soils, breccias, and basalts. This correlation is given by

$$Ar^{40}_{intercept} = 4 \times 10^{-8} \text{ K(ppm) } cm^3 \text{ STP/g.}$$

Thus for 1141 ppm the $Ar^{40}_{intercept}$ value should be 0.456×10^{-4} cm^3 STP/g. The K^{40}-Ar^{40} age that results from the real intercept value of 0.140×10^{-4} cm^3 STP/g is 1.8 by. There exist other such apparently young ages at the Apollo 15 site (15501, 15601, 15091). Discussion of what these discordant ages imply will be given below (Section VI-D).

15421, Station 7: Figure 9 shows that this soil consists of two components. The linear best fit for all the data is:

$$Ar^{40} = 3.31\ Ar^{36} + 0.301 \times 10^{-4}\ cm^3\ STP/g.$$

The four smallest fractions have a linear best fit of:

$$Ar^{40} = 2.97\ Ar^{36} + 0.388 \times 10^{-4}\ cm^3\ STP/g$$

while the linear best fit of the four largest fractions is:

$$Ar^{40} = 3.94\ Ar^{36} + 0.082 \times 10^{-4}\ cm^3\ STP/g.$$

I have noted earlier that the He^4/Ne^{20} ratios of sample 15421 imply a green glass content of ~ 60%. The green glass has been estimated to have Ar^{40}/Ar^{36} ~ 4-5 (Lakatos et al., 1973). The Ar^{40}/Ar^{36} ratio of the non-green glass material is unknown, but judging from other fines in the vicinity it may be as low as 1.0 (average values of Ar^{40}/Ar^{36} from 15271, Station 6, from Jordan et al., 1974). It appears that the green glass dominates the four largest grain size fractions of 15421. Both the non-green glass and green glass materials influence one another's individual Ar^{40}/Ar^{36} slopes to the extent that they lie near the average slope of 3.31.

Using the volume correlated component for all size fractions 0.301×10^{-4} cm^3 STP/g and a K content of the 15427 (LSPET, 1972) of 913 ppm, one obtains an apparent K^{40}-Ar^{40} age of 3.2 by.

15511, Station 9: These fines display no linear correlation. The lines shown in Figure 10 represent estimated limits for the Ar^{40}/Ar^{36} slopes. The lower limit of ~0.9 is slightly higher than the Ar^{40}/Ar^{36} ratio of mare fines and may represent the lower limit of the Ar^{40}/Ar^{36} ratios of the Apennine Front fines. The slope of ~3.0 approaches the highest Ar^{40}/Ar^{36} ratio of the Front fines 15421 (Ar^{40}/Ar^{36} = 3.31, Jordan et al., 1974). These fines were collected from the rim of the fresh young 10 m diameter crater 300 m from Hadley Rille and 75 m south of the rim of Scarp Crater (250 m diameter) and southwest of the younger unnamed crater of the same dimensions. Apparently the two larger craters have excavated materials from considerable depths which have a wide range of Ar^{40}/Ar^{36} ratios, and the young 10 m crater has merely re-excavated this material. That such variation in the Ar^{40}/Ar^{36} ratios exist at depths at least down to 240 cm is revealed by inert gas studies of the drill core 15001/15006 (Bogard and Nyquist, 1972b; Bogard et al. 1973; Hübner et al., 1973). This core, 242 cm long and 2.04 cm in diameter, was collected by the crew of Apollo 15 at station 8, 50 m from the ALSEP station (Heiken et al., 1972). The $(Ar^{40}/Ar^{36})_T$ ratio in samples from this core does not show any systematics, but variations from ~0.9 to ~ 1.6 have been reported (Bogard et al., 1973; Hübner et al., 1973). Hübner et al. (1973) suggest that such variations could be explained by periodic large impacts on the Apennine Front.

Indeed, the Ar^{40}/Ar^{36} ratios of 15511 do have ratios that resemble the Front fines, and it is noteworthy that the 500 - 1000 μm fraction of 15511 contain ~ 30% green glass spheres (Heiken, 1974). The large variations in the Ar^{40}/Ar^{36} ratios in the - now surface - fines of 15511 suggests that there has not been adequate time for the ratios of these fines to assume the present day ratio of Ar^{40}/Ar^{36} in the mare fines.

15501, Station 9: Collected 10 m from the rim of the 10 m diameter young fresh crater, these fines resemble 15511 in the variability of their Ar^{40}/Ar^{36} ratios (Figure 11) although there is a fair correlation between Ar^{40} and Ar^{36} given by $Ar^{40} = 0.723\ Ar^{36} + 0.246 \times 10^{-4}$ cm^3 STP/g. The $(Ar^{40}/Ar^{36})_T = 0.723$ does resemble that of nearby mare fines (15601, station 9A: from size fractions, $Ar^{40}/Ar^{36} = 0.86$, Yaniv and Heymann, 1972; from average of bulk fines, $Ar^{40}/Ar^{36} = 0.75$, Jordan et al., 1974). The 15501 surface fines may reflect a more extensive exposure to present day solar wind than the fines 15511, so that the variations that appear in 15511 have been reduced to the values now present in 15501. Further exposure may result in complete erasure of previous variations so that the final correlation may resemble that of 15071 (Figure 8).

Using the Ar^{40} intercept of 0.246×10^{-4} cm^3 STP/g and a K-contents of 1328 ppm (LSPET, 1972) the apparent K^{40}-Ar^{40} age is 2.4 by.

D. Low Ar^{40} Intercept Values and Apparent K^{40}-Ar^{40} Ages From Apollo 15 Fines

Shown in Table 6 is a summary of Ar^{40} intercept values and apparent K^{40}-Ar^{40} ages discussed in section VI-C plus the same from two additional Apollo 15 fines - 15091 (Jordan et al., 1974) and 15601 (Yaniv and Heymann, 1972). The ages represent a weighted average of K^{40}-Ar^{40} ages of individual particles within the size fractions. Fines 15601, 15511, and 15071 collected near Hadley Rille on the mare surface have apparent K^{40}-Ar^{40} ages (2.0 by., 2.4 by., 1.8 by., respectively) younger than the 3.3 by. age of the crystalline rocks on the mare surface (Schaeffer et al., 1972). Fines 15091 are near Hadley Rille on the Front surface and have an apparent K^{40}-Ar^{40} age of 2.6 by.; whereas much further away from Hadley Rille on the Front fines 15421 have an apparent K^{40}-Ar^{40} age of 3.2 by.

Husain et al. (1972) report K^{40}-Ar^{40} ages for rocks from Hadley Rille and Spur Crater which are in good agreement with the ~ 3.3 by. age determined by techniques which are not influenced by radiogenic Ar^{40} loss (eg. Ar^{39}-Ar^{40}, Rb-Sr). This implies there has been little if any radiogenic Ar^{40} loss by diffusion from these rocks. Thus unless one invokes processes whereby the lunar fines lose radiogenic Ar^{40} more readily than the rocks from which they form, one must conclude that there has been a contribution to the

regolith at the Apollo 15 site of materials with an apparent K^{40}-Ar^{40} age < 1.8 by (the youngest age in Table 6) from some external source. Photogeologic maps of the entire landing site reveal light colored rays and satellitic clusters of secondary impact craters (South Cluster) which are associated with the much larger (~ 50 km diameter) craters Autolycus and Aristillus to the north. These ray craters are believed to be Copernican age (Swann et al., 1972), a relative age based on photogeologic maps of large regions of the moon. The Copernican age is associated with the formation of Copernicus Crater ~ 400 km north of the Apollo 12 landing site. Eberhardt et al. (1973) have determined an Ar^{39}-Ar^{40} age of 800 my. for KREEP (materials enriched in K, rare earths, and P) glass from soil 12033, which they interpret as the age of Copernicus Crater, provided that the glass was ejected by the Copernicus event. If Autlycus and Aristillus are, indeed, Copernican age (800 my or younger) then these craters could provide materials with the necessary apparently young K^{40}-Ar^{40} ages in the Apollo 15 fines.

VII. THE APOLLO 17 LANDING SITE: EVIDENCE FOR RECENT MIXING AT TRENCH NEAR VAN SERG CRATER

A. General Description of Trench

A planimetric map of the Apollo 17 landing site and the location of discussed samples are shown in Figure 12. Inert gas contents, elemental and isotopic ratios of bulk fines are given in Table 7. The regolith at the Apollo 17 is rich in trapped inert gases, with Ar^{36} contents ranging from 0.15×10^{-4} cm^3 STP/g to 6.2×10^{-4} cm^3 STP/g (cf. Apollo 15 fines, Table 2). Strikingly high values occur at the Trench at Station 9 near Van Serg Crater.

Van Serg is a fresh 90 m diameter crater. The ejecta blanket is blocky and the dominant rock type is described as a dark matrix-rich breccia (Muehlberger et al., 1973). A 17 cm trench was dug by the astronauts (Schmitt and Cernan) at station 9, approximately 60 m southwest of the rim and 10 m from the rim of the older Subdued Crater. The astronauts observed a dark surface soil cover of only a few centimeters in thickness on top of a lighter gray fragmental material. Three soil samples were collected from the trench: 79220 from 0-2 cm; 79240 from 2-7 cm; and 79260 from 7-17 cm. I have determined inert gas contents in the fines 79221, 79241, and 79261 from the three levels.

B. Grain Size Analysis of Fines 79221, 79241, and 79261

In an attempt to arrive at a more suitable choice of diameter than the usually chosen average diameter within a size range, Heymann et al. (1975) defined an effective diameter D_{eff}. D_{eff} is the uniform diameter of spherical particles of an imaginary sample which has the same volume and specific surface area as the real sample (see Appendix C for determination of D_{eff} for 79221, 79241, 79261). Heymann et al. (1975) assume that for a given size fraction (mesh sizes $D_n < D_m$) that the size distribution law is given by:

$$N(D) = kD^{-\alpha},$$

where N(D) is the number of particles with diameter greater than D, and k and α are constants. Further assuming particle sphericity and that the average bulk density, $\bar{\rho}$, is the same for all size fractions, they obtain expressions for the weight ratios of any two size fractions which may be used to determine the unknown quantity α:

$$\frac{W_{m,n}}{W_{p,q}} = \frac{[D_m^{(3-\alpha)} - D_n^{(3-\alpha)}]}{[D_p^{(3-\alpha)} - D_q^{(3-\alpha)}]}$$

$$\frac{W_{m,n}}{W_{p,q}} \ (\alpha=3) = \frac{\ln(D_m/D_n)}{\ln(D_p/D_q)} \quad .$$

I determined values of $W_{m,n}/W_{p,q}$ from the weights of the sieve fractions and found the following estimates for

79221	63-250	3.00
	250-500	3.50
	500-700	4.20
	700-1000	4.70
79241	63-250	3.00
	250-354	3.50
	354-500	3.00
	500-700	4.50
	700-1000	5.00
79261	63-250	3.00
	250-354	3.50
	354-500	2.50
	500-700	4.00
	700-1000	5.50

The size range 63-250 is a combination of the narrower size range 63-105 μm and 105-250 μm which have α's at or near 3.00 but display a gradual increase toward 3.50. I interpret this α range $3.00 \leq \alpha \leq 3.5$ for the size range 63-354 μm to be a reflection of the size distribution prior to the addition of the coarse grain component. The sudden jump to values of 4.00 - 5.50 in the ranges 500-700 μm and 700-1000 μm suggests the addition of a completely different size distribution which is dominated by coarse grains. Note also a drop in α values for samples 79241 and 79261 in the range 354-500 μm. We may understand this by considering curves resulting from plotting N(D) vs. D (Figure 13) for

the two distributions. For the soil prior to the addition of the coarse component one would expect a smooth cummulative curve with gradually changing slope, yielding α values in the range 2.50 - 3.50. The coarse component, on the other hand, would have a relatively steep slope in the larger sizes (with $4.00 \leq \alpha \leq 5.50$) which flattens rapidly in the smaller grain size fractions. The addition of the two cummulative curves results in a composite curve which has the following shape:

(1) a steep slope in the larger grain size fractions

(2) a more gradual slope in the finer grain size fractions,

(3) a "shoulder" with flat or gradual slope (low α's) where the inflexion occurs.

The low α's in 79241 and 79261 are, hence, interpreted to represent the "shoulder" of the composite distribution curve. The absence of a low α value in the range 354-500 μm of the uppermost soil, 79221, merely reflects the fact that particle comminution by micrometeorite bombardment must ultimately smooth out such a composite distribution.

D. Inert Gases in Size Fractions of 79221, 79241, 79261

1. Ar^{36} versus D_{eff}.

The inert gas contents of 79221, 79241, and 79261 are given in Table 8. Figure 14 shows Ar^{36} vs. D_{eff} for 79221,

79241, and 79261. The curves of all three have in common: (a) rather shallow slopes ($n < 1$), (b) striking anomalies ("jumps") where the coarser of two adjacent size fractions contains more trapped gas than the finer fraction.

Figure 14 shows only the Ar^{36} trends. However, it can be seen from Table 8 that the trends for other gases are grossly similar to the Ar^{36} trends. There are several possible explanations for the observed behavior:

a all three fines are agglutinate rich and most of the trapped gas is contained in the constructional particles. Heiken and McKay (1974) have reported agglutinate contents of 44.4% and 22.3% in the 90-150 μm fractions of 79221 and 79261 respectively. The trapped gas contents of the 88-105 and 105-250 μm fractions (Table 8) are roughly proportional to agglutinate contents, which supports this hypothesis.

b however, agglutinate contents of fines tend to decrease rapidly for particles greater than about 250 μm and the curves are still conspicuously flat for $D_{eff} >$ 250 μm. Another source of gas-rich material is abundantly present near the trench, namely soil-breccias such as 79035 and 79135 for which Hintenberger et al. (1975) have reported large inert gas contents (in the 35-54 μm size fraction). The comminution of such breccias by the Van Serg event itself, and subsequently by micrometeorite impact on the blocks at the surface of the ejecta blanket may have been

an important source of gas-rich particles in all size fractions.

c Flatness of curves may be the consequence of the fact that larger grain size fractions must get saturated earlier according to Rosiwal principle (Criswell, 1975).

d Mixing of two soils which have surface correlated gas, but different absolute amounts of these gases.

Explanation d is illustrated in Figure 15. Curve A represents soil which is more gas rich than the soil represented by Curve B. Mixing size fractions in equal proportions would result in Curve C. Sorting may result in many possibilities between Curves A and B. Curves D and E illustrate the contribution of coarse material from the soil characterized by Curve A to the soil characterized by Curve B.

2. Eberhardt Plots

Figures 16, 17, and 18 show Eberhardt plots for 79221, 79241, and 79261, respectively. Straight lines (such as the solid lines in Figure 16) are the locus of samples which contain the same amount of cosmogenic Ne^{21}_C and have the same $(Ne^{22}/Ne^{21})_T$ ratio. Addition of Ne^{21}_C moves sample downward and to the left. Addition of Ne_T moves points upwards and to the left.

Figure 16 shows that the data for 79221 scatter between the extremes represented by the 818 μm and the < 63 μm frac-

tions. If one disregards for the moment the 818 μm fraction then the extremes are the 582 μm and the < 63 μm fractions. From scattered points such as in Figure 16 one cannot obtain the value of $(Ne^{22}/Ne^{21})_T$. Because of this I have assumed $(Ne^{22}/Ne^{21})_T = 32.0$, a value within the range of lunar fines. The line through this assumed value and any sample point determines the amount of Ne^{21}_C in that sample. With a Ne^{21}_C production rate of 0.17×10^{-8} cm^3 STP per m.y. (chemistry from LSPET, 1973 and production rate equation from Yaniv et al., 1971) I have calculated nominal exposure ages for the samples. A sample age of 800 m.y. means that this sample would have acquired 800 m.y. worth of Ne^{21}_C if exposed to cosmic rays at a depth where the Ne^{21}_C production rate is 0.17×10^{-8} cm^3 STP per m.y.

Figure 16 shows that the size fractions in 79221 are mixtures of a very heavily irradiated material with nominal exposure age of 800 m.y. or older and a very lightly irradiated material with uncertain, but young nominal exposure age (the assumed $(Ne^{22}/Ne^{21})_T$ value of 32.0 yields 10 m.y., but this age is very sensitive to the trapped ratio). The size fractions 582 μm to < 63 μm can also be interpreted as mixtures between the very heavily irradiated material and a moderately irradiated material with nominal exposure age of 240 m.y. or younger.

Figures 17 and 18 show that fines 79241 and 79261 too are mixtures of very heavily and moderately irradiated ma-

terials. The dashed lines in these Figures show how the nominal exposure ages change for $(Ne^{22}/Ne^{21})_T = 31.0$. The largest change is about 15% which is an indication of the uncertainties in the absolute age values.

3. Ar^{40} vs. Ar^{36} trend

Figure 19 shows Ar^{40} vs. Ar^{36} for the three trench samples. While Ar^{40} tends to increase with Ar^{36}, the samples do not fall on or near a single straight line, but scatter between two extreme lines, one having an $(Ar^{40}/Ar^{36})_T$ slope of about 1.3; the other of about 2.5. (The lowermost line was fitted to two samples from 79221 and 79261; it yields an Ar^{40} intercept value of 4.0×10^{-5} cm^3 STP/g. The uppermost line was fitted to a calculated intercept value of 6×10^{-5} cm^3 STP/g and one sample from 79241.) As before, the most logical explanation is that the trench fines are mixtures of at least two materials, one with $(Ar^{40}/Ar^{36})_T = 2.5$ or greater, the other with $(Ar^{40}/Ar^{36})_T = 1.3$ or smaller.

E. Interpretation of the Trench

1. Pre-Van Serg regolith surface

An attempt to define a pre-Van Serg surface using the fines from the three levels of the trench requires other chemical and petrological evidence, in addition to information from inert gases. Systematic differences might be expected to occur between samples on either side of the boun-

dary.

The inert gases in 79221 are twice as gas rich as 79241. Based on the inert gas evidence alone this systematic "break" would place the pre-Van Serg surface somewhere between 2 and 7 cm depth. Referring to Table 9, one sees that this evidence is supported by U^{238}/Pb^{204} (Nunes et al., 1974) and to some extent (no data for 79241) by agglutinate content (Heiken and McKay, 1974). However, FeO and TiO_2 (Rose et al., 1974) and C (Moore et al., 1974) do not support this conclusion. MgO and Al_2O_3 (Rose et al., 1974; not shown); Pb^{207}/Pb^{206} (Nunes et al., 1974) and graphic mean grain size (Butler and King, 1974) change too regularly to allow any conclusions.

Schmitt and Cernan observed a distinct change in albedo at a depth of 7 cm (Muehlberger et al., 1973). This observation is consistent with the trends of agglutinate content, FeO + TiO_2, and Al_2O_3 (increases from 79221 to 79261). Hence, the visible boundary could represent the pre-Van Serg regolith surface. This implies that the Van Serg ejecta blanket at the trench site has been stratified from the beginning, with the top 2 centimeters richer in the relatively fine-grained, gas-and agglutinate-rich material than the underlying material represented by 79241.

McGetchin et al. (1973) have developed equations for radial thickness variations in impact crater ejecta. The equation for impact ejecta for craters of less than 100 km

in radius R is:

$$t = 0.04\ R\left(\frac{r}{R}\right)^{-3}$$

where r ≡ the range of crater ejecta measured from the center of the crater. Thus, for R = 45 m and r = 45 m + 60 m = 105 m, I obtain t = 14 cm at Station 9. This would place the pre-Van Serg surface between 7 and 17 cm. However, the model is probably only good within a factor of two for small craters since one should expect lateral variations in ejecta thickness as well.

The evidence presented does not exclude the possibility that the pre-Van Serg surface is deeper than 17 cm, hence has not been exposed in the trench.

2. Trench top

I assume that the trench top, as represented by 79221, is definitely Van Serg ejecta. Fleischer and Hart (1974) have estimated the age of Van Serg between 19 and 24 m.y.

Fines 79221 contain at least two major materials: 1) a mature, agglutinate- and gas-rich soil, and 2) a relatively coarse-grained, fairly gas-rich material. McKay et al. (1974) were the first to suggest a two-component mixture for 79221; they suggested that the coarse-grained component is derived from breccias, which were comminuted by the Van Serg impact, and subsequently - at the surface - by micrometeorite impact. The inert gas results support this

contention. In this respect it is interesting to note that the corrected Pb^{207}/Pb^{206} ratio decreases downward in the trench from a value of 0.8177 in 79221 to 0.7430 in 79261 (Nunes et al., 1974). Church and Tilton (1975) report blank-corrected values of 0.9251 and 0.9183 in two samples of the soil breccia 79135. Hence the lead data also support the presence of a soil-breccia derived component in 79221.

At least some of the source material of the coarse-grained component has been poorly irradiated (by cosmic rays), in fact, was deposited on the surface with little if any pre-irradiation. The young exposure age of the > 700 μm fraction is consistent with Fleischer and Hart's age for Van Serg. Thus it is remarkable that the three rocks from station 9 for which exposure ages are known, 79035, 79135 (both soil breccias), and 79155 (heavily shocked, mare basalt) have old exposure ages of 600 ± 50; 810 ± 60 (Ne^{21}_{C}-ages by Hintenberger et al., 1974); and 575 ± 60 m.y. (Ca-Ar^{37} by Kirsten and Horn, 1974). These ages are so similar to the "old age limits" in Figures 16, 17, and 18 that they lend support to the hypothesis that soil breccias 79035 and 79135 have been produced from heavily irradiated soils by the Van Serg impact.

An alternative hypothesis is that the breccias are excavated by the Van Serg impact. Muehlberger et al., (1973)

have concluded that the regolith at Van Serg is at least 15 m thick. They suggest that the dark matrix breccias come from the deepest portions of the regolith. If 79035 and 79135 were excavated from a depth greater than about ten meters, then it seems that the Van Serg soil cover is underlain by a soil-breccia horizon of substantial thickness. This horizon then contains - at Van Serg - heavily irradiated material, and might be the repository of much of the "missing" cosmic ray record (Fireman, 1974). Along these lines it is interesting to note that I have observed the same heavily (relatively speaking) irradiated zone below more lightly irradiated material at the Apollo 15 landing site (section V-B). This suggests but does not prove that such zones may be a common occurrence on the moon.

3. Trench middle and bottom

The middle and bottom of the trench also contain the heavily irradiated material seen in 79221. As in the case of 79221, the source could be soil breccias, excavated by Van Serg or by the older, subdued crater nearby. It is interesting to note in Figure 19 that 79241 and 79261 contain a greater proportion of material with $(Ar^{40}/Ar^{36})_T$ = 2.5 or larger, and that the trapped ratios in 79035 and 79135 are 2.18 $\pm$ 0.05 and 2.5 $\pm$ 0.1 respectively (Hintenber et al., 1975). However, the bulk Ar^{40}/Ar^{36} ratios in the three trench fines (top-to-bottom) are only 1.5, 1.8

and 1.9 respectively. Hence, 79035 and 79135 could not have been formed from soils now at the surface of the trench. A similar relationship exists at the Apollo 11 site, where the microbreccias have greater $(Ar^{40}/Ar^{36})_T$ ratios than the surface soils (Funkhouser et al., 1970). Furthermore, the Apollo 15 fines 15511, which apparently contain material from depths below the estimated regolith thickness at the site of 5 m, has in its coarse grain size fraction materials which have large $(Ar^{40}/Ar^{36})_T$ ratios compared to the surrounding mare fines. Whether or not these are microbreccias is not known. However, this observation suggests, but does not firmly prove, that the Apollo 11 microbreccias, the Van Serg breccias and perhaps the 15511 coarse materials were formed by much more ancient impacts than Van Serg.

VIII. CONCLUSIONS

A. Undersaturated Surfaces

I have found lunar soils from the Apollo 15 site (15421, 15071) which appear to be undersaturated with respect to solar irradiation. The undersaturated component of 15421 seems to be concentrated primarily in the green glass spherules which comprise ~ 60% of this sample. Because of their unique history of formation they probably were exposed to the solar wind for a very short time interval. The effect of undersaturation in 15071 is reflected in the value of the exponent in the equation $C(cm^3STP/g) = kD^{-n}$ which has the trend $n_4 > n_{20} > n_{36} > n_{84} > n_{132}$. I have explained this in terms of the Rosiwal principle which requires that large grains saturate earlier than smaller ones. Superimposed on this basic pattern are the effects of particle comminution and agglutinate formation. Having examined many n values from samples of Apollo 11, 12, 15, 16, and 17 landing sites, I observe that this is a general characteristic of all of these landing sites expressed in varying degrees. If my interpretation of 15071 is correct, most if not all of the landing sites have grain surfaces which have not yet reached saturation with respect to (at least) the heavier inert gases Ar^{36}, Kr^{84}, and Xe^{132}. This

could have interesting consequences with respect to solar wind energies as a function of time. If one could find saturated particles which were less gas rich than an undersaturated particle, assuming no unusual volume components, this would imply that the undersaturated soil was exposed at the surface at a time when solar wind energies were higher. That is to say, higher energy ions will penetrate deeper into particle surfaces, but will require a greater length of time and larger quantities of gas to fill these surfaces to the point of saturation than would be required for surfaces exposed to lower energy ions.

B. Heavily Irradiated Zones

I have shown that there may exist zones beneath the regolith which are more heavily irradiated, with respect to cosmic rays, than the overlying soil cover. The breccias 79135 and 79035 and the finer and some of the coarser fraction of the Station 9 trench fines at the Apollo 17 landing site contain very heavily irradiated material, possibly >800 my. These may be interpreted to be ejecta from the Van Serg Crater event, which may have brought materials up from deep within the regolith or even below. I have observed the same relationship at the Apollo 15 site. The regolith there is only about 5 m thick. It is apparently lightly irradiated with exposure ages of ~250 my. In the coarsest fraction of

15071 and 15601, however, there is material with exposure ages of ~ 400 my. Since 15071 fines could represent ejecta from Elbow Crater and 15601 fines material from a very thin regolith, I interpret the coarser, more heavily irradiated material to have come from beneath the regolith at that site.

C. Large Scale Mixing

The fines 15511 from Station 9 at the Apollo 15 landing site have Ar^{40}/Ar^{36} ratios which resemble the Apennine Front fines 2 - 3 km away. The materials which have similar ratios at Station 9 may have arrived there as a result of large scale impacts on the Apennine Front as suggested by Hübner et al. (1973). Similarly, the low apparent K^{40}-Ar^{40} ages suggest addition of relatively young material from some external source to the older (~ 3.3 by) mare materials. These materials could have been brought to the site by the formation of Autolycus and Aristillus, two large craters to the north of the site. These craters are believed to be Copernican age which may be ~ 1 by. Ray materials from these craters in the Apollo 15 landing site could indeed cause the observed young apparent K^{40}-Ar^{40} ages.

D. A Suggestion for Future Experiments

The effect of agglutinates in lunar soils on the Ne_C^{21} ages has been demonstrated with the > 500 μm fraction of

15080. If agglutinates tend to lower Ne^{21}_{C} exposure ages for lunar fines in general, then I suggest separating the agglutinates from non-agglutinates by magnetic separation. This may result in higher Ne^{21}_{C} ages, and perhaps a more realistic picture of surface exposure history in gas contents vs. grain diameter plots.

APPENDIX A

Admission technique: It has often been our experience that for total gas release from lunar fine material weighing $\gtrsim$ 2500 μg the He^4, Ar^{40}, Ar^{36}, and to a lesser extent Ne^{20} signals would exceed 30 volts, the maximum output scale setting. Various pumping procedures were employed, which compounded the error in the He^4, Ne^{20}, Ar^{40}, and Ar^{36} contents and the He^4/He^3, Ar^{40}/Ar^{36}, He^4/Ne^{20}, and Ne^{20}/Ar^{36} ratios of the soils. Pumping at least twice to get He^4, Ar^{40}, and Ar^{36} signals on scale was not an uncommon practice, thereby lengthening the time of the experiment. To eliminate several pumpings I reduced sample weights when feasible to about 1000-2000 μg for bulk soils and fine grain fractions, and adopted the following gas admission technique as standard procedure.

1) restricted volume. Shortly before opening V2 (the valve joining the prepline to the mass spectrometer) for gas measurement, V3 was closed, isolating a small fraction of the total gas behind the valves V2, V3, and V5. It is then necessary to know the volume ratio (VR) of the total prepline + mass spectrometer to the restricted volume + mass spectrometer, for this number is the factor by which one must multiply restricted volume signals to obtain total signals. The ratio VR may be determined by dividing the

total signal by the restricted signal which is on scale in both cases, eg. using Ar^{38},

$$VR_{38} = \frac{Ar^{38} \text{ (total mv)}}{Ar^{38} \text{ (restricted mv)}} = \frac{1000 \pm 10 \text{ mv}}{180 \pm 2 \text{ mv}} = 5.56 \pm 0.08$$

2) pumping ratio . Even with lower weights and a restricted volume of gas admitted to the mass spectrometer, the He^4 signal commonly exceeded 30 volts and part of this gas had to be eliminated by pumping. This was done by closing V2 and opening V1 (connecting the mass spectrometer to the ion pump) and pumping the gas from the mass spectrometer. Shortly after pumping begins He^4 was on scale and was used as a monitor to determine how long one must pump to evacuate the mass spectrometer to an acceptable pressure; typically, this time was 7-10 minutes. After this length of time, the gas was readmitted for measurement of He^4 and some other isotopes (usually Ne^{20}) used to determine the pumping ratio (PR). The pumping ratio (PR), which enables one to determine the original He^4 signal, is the ratio of the signal of an isotope that is on scale before pumping to the signal after pumping, eg.

$$PR_{20} = \frac{Ne^{20} \text{ (mv - before pumping)}}{Ne^{20} \text{ (mv - after pumping)}}$$

$$= \frac{1960 \pm 20 \text{ mv}}{140 \pm 2 \text{ mv}} = 14.00 \pm 0.25.$$

APPENDIX B

Determination of NSMV: Determining the gas concentration per gram of sample, C, requires knowledge of the net millivolt signal from the sample, NSMV. If the total volume of gas was admitted, this number was obtained by subtracting the blank millivolt signal, BMV, from the measured millivolt signal, MMV. On several occassions only a restricted volume was introduced and possibly pumping was required to obtain signals under 30 volts (the maximum scale setting). Thus it was necessary to multiply MMV by the volume ratio, VR, and possibly the pumping ratio, PR, before subtracting BMV. We may summarize these options as follows:

Option	NSMV
1. total volume introduced, no pumping required	MMV - BMV
2. restricted volume introduced, no pumping required	MMV x VR - BMV
3. restricted volume introduced, pumping required	MMV x VR x PR - BMV

These options were digitized and incorporated into a computer program (written by G. E. Fryer) which calculated gas contents and elemental isotopic ratios with errors. Compu-

tations were done on a Monroe desk computer (Model 1800).

Errors: Errors in the gas concentration are due to weighing (± 5.0 μg), signal noise, and sensitivity (± 2%). Where a restricted volume was introduced the error in VR (± 1.5%) contributes to the error in NSMV, and in the most extreme case where pumping is required errors in NSMV may be further increased by the errors in PR (± 1.5%). Typical errors from signal noise were as follows:

Scale (mv)	Signal (mv)	Noise (%)
3	1	± 20
	2	± 10
	3	± 5
10	3	± 5
	6	± 3
	9	± 2
30	10	± 2
	20	± 1
	30	± 1
≥ 30	≥ 30	± 1

Errors in isotopic and elemental ratios were obtained from gas concentrations according to the relation

$$\frac{C_1 \pm c_1}{C_2 \pm c_2} = \frac{C_1}{C_2}\left(1 \pm \sqrt{\left(\frac{c_1}{C_1}\right)^2 + \left(\frac{c_2}{C_2}\right)^2}\right) .$$

APPENDIX C

Determination of the Effective Diameter: The construction of diagrams displaying inert gas contents versus grain diameter depends on the choice of an appropriate diameter within a size range. Choosing the average grain diameter is the simplest approach but may distort possible anticorrelations somewhat if the grain size distribution curves are greatly skewed (positively or negatively) about the mean diameter. Ideally one would like to know the shape of these curves for each size range and then use the modal diameter. However, these distribution curves are not always avaiable. An alternative approach is presented by Heymann et al. (1975). They assume that the size distribution law for a given size fraction is given by:

$$N(D) = kD^{-\alpha}$$

, where N(D) is the number of particles with diameter greater than D, and k and α are constants. It is further assumed that all particles in the real sieve fraction are spherical, and then they define an effective diameter D_{eff} ($D_m > D_{eff} > D_n$; D_m and D_n are, respectively, upper and lower limits of mesh sizes) as the uniform diameter of spherical grains in a hypothetical sample which has the same total surface area and volume as the real sample. With these assumptions they obtain:

$$(1)\quad D_{eff} = \frac{2-\alpha}{3-\alpha}\ \frac{[D_m^{(3-\alpha)} - D_n^{(3-\alpha)}]}{[D_m^{(2-\alpha)} - D_n^{(2-\alpha)}]}$$

$$(2)\quad D_{eff}\ (\alpha=2) = \frac{(D_m - D_n)}{\ln(D_m/D_n)}$$

$$(3)\quad D_{eff}(\alpha=3) = \frac{\ln(D_m/D_n)}{[1/D_n - 1/D_m]}$$

Heymann et al. (1975) estimate the unknown quantity, α, from the weight, W, of each sieve fraction by assuming that the mean bulk density, $\overline{\rho}$, is the same for each sieve fraction, for which these equations follow:

$$(4)\quad \frac{W_{m,n}}{W_{p,q}} = \frac{[D_m^{(3-\alpha)} - D_n^{(3-\alpha)}]}{[D_p^{(3-\alpha)} - D_q^{(3-\alpha)}]}$$

$$(5)\quad \frac{W_{m,n}}{W_{p,q}}(\alpha=3) = \frac{\ln\ (D_m/D_n)}{\ln\ (D_p/D_q)}\ .$$

Using equations (1) and (3) to determine the effective diameters, after determining α values from equations (4) and (5), we have the following result for three Apollo 17 trench soils:

Size range	D_{eff} 79221	79241	79261
* 1 - 63	8	8	8
63 - 74	68	68	68
74 - 88	81	81	81
88 - 105	96	96	96
105 - 250	157	157	157
250 - 354	294	294	294
354 - 500	417	419	421
500 - 700	582	581	583
700 - 1000	818	815	811

* An $\alpha = 2.50$ was adopted for this size range.

ACKNOWLEDGEMENTS

The author expresses sincere appreciation to Dr. Dieter Heymann for his valuable guidance and support throughout this research and my years at Rice.

I am also grateful to Dr. Akiva Yaniv for his valuable discussions.

Sincere appreciation goes also to Mr. G. E. Fryer for assistance in mass spectrometer measurements and development of a computer program for calculations.

A special debt of gratitude goes to Miss Jeannine Klein for her time and effort in typing this thesis.

TABLE 1

TYPICAL BLANK VALUES FOR INERT GASES

(UNITS: cm^3 STP)

He^3	He^4	Ne^{20}	Ne^{21}	Ne^{22}
*	3.5×10^{-7}	2.1×10^{-8}	6.0×10^{-11}	2.2×10^{-9}

Ar^{36}	Ar^{38}	Ar^{40}	Kr^{84}	Xe^{132}
2.1×10^{-10}	4.3×10^{-11}	3.6×10^{-8}	*	*

* not detectable above noise level

TABLE 2

INERT GAS CONTENTS AND ISOTOPIC AND ELEMENTAL RATIOS
OF SIZE FRACTIONS OF FINES FROM APOLLO 15

(UNITS: cm^3 STP/g)

Sample: 15071 (Station 1)

Size (μm)	He^3 x 10^{-5}	He^4 x 10^{-2}	Ne^{20} x 10^{-4}	Ne^{21} x 10^{-6}	Ne^{22} x 10^{-5}	Ar^{36} x 10^{-4}	Ar^{38} x 10^{-5}	Ar^{40} x 10^{-4}	Kr^{84} x 10^{-8}	Xe^{132} x 10^{-8}
63-74 (937.5 μg)	1.115 ±0.036	2.591 ±0.070	5.802 ±0.156	1.802 ±0.062	4.562 ±0.158	1.209 ±0.028	2.268 ±0.052	1.107 ±0.027	4.633 ±0.278	0.807 ±0.153
74-88 (1640 μg)	0.829 ±0.026	1.764 ±0.047	4.624 ±0.123	1.506 ±0.054	3.635 ±0.120	1.076 ±0.024	2.008 ±0.045	1.002 ±0.023	3.824 ±0.214	0.610 ±0.131
88-250 (1494.5 μg)	0.725 ±0.029	1.481 ±0.039	3.627 ±0.096	1.272 ±0.047	2.855 ±0.098	0.930 ±0.021	1.757 ±0.037	0.820 ±0.018	3.628 ±0.200	0.478 ±0.095
250-354 (1615 μg)	0.496 ±0.015	0.734 ±0.019	2.382 ±0.071	0.981 ±0.035	1.907 ±0.060	0.456 ±0.010	0.876 ±0.020	0.507 ±0.013	1.932 ±0.108	0.345 ±0.073
354-500 (2469 μg)	0.663 ±0.018	0.872 ±0.023	2.523 ±0.075	1.226 ±0.050	2.035 ±0.062	0.586 ±0.013	1.121 ±0.025	0.674 ±0.016	2.162 ±0.111	0.441 ±0.100
500-700 (2180 μg)	0.582 ±0.016	0.666 ±0.018	2.062 ±0.056	1.077 ±0.054	1.665 ±0.044	0.500 ±0.011	0.972 ±0.021	0.496 ±0.013	2.027 ±0.155	0.365 ±0.078

TABLE 2 (CONTINUED 1)

Sample: 15071 (Station 1)

Size (μm)	$\frac{He^4}{He^3}$	$\frac{Ne^{20}}{Ne^{22}}$	$\frac{Ne^{21}}{Ne^{22}}$	$\frac{Ar^{36}}{Ar^{38}}$	$\frac{Ar^{40}}{Ar^{36}}$	$\frac{He^4}{Ne^{20}}$	$\frac{Ne^{20}}{Ar^{36}}$	$\frac{Ar^{36}}{Kr^{84}}$	$\frac{Kr^{84}}{Xe^{132}}$
63-74	2322 ± 98	12.72 ±0.58	0.0395 ±0.0026	5.329 ±0.174	0.915 ±0.031	44.65 ±1.70	4.799 ±0.170	2609 ±168	5.74 ±1.14
74-88	2129 ± 87	12.72 ±0.54	0.0414 ±0.0020	5.361 ±0.172	0.931 ±0.030	38.14 ±1.44	4.296 ±0.150	2814 ±170	6.27 ±1.39
88-250	2043 ± 98	12.70 ±0.57	0.0445 ±0.0022	5.293 ±0.163	0.882 ±0.028	40.83 ±1.53	3.900 ±0.191	2563 ±153	5.32 ±1.10
250-354	1478 ± 59	12.49 ±0.54	0.0514 ±0.0025	5.208 ±0.165	1.112 ±0.038	30.81 ±1.22	5.224 ±0.182	2360 ±142	5.59 ±1.22
354-500	1316 ± 49	12.39 ±0.53	0.0602 ±0.0031	5.228 ±0.166	1.150 ±0.037	34.57 ±1.37	4.303 ±0.160	2710 ±151	5.04 ±1.18
500-700	1144 ± 44	12.38 ±0.47	0.0646 ±0.0037	5.144 ±0.159	0.992 ±0.034	32.33 ±1.23	4.121 ±0.145	2467 ±196	5.56 ±1.27

TABLE 2 (CONTINUED 2)

Sample: 15421 (Station 7)

Size (μm)	He^3 x 10^{-5}	He^4 x 10^{-2}	Ne^{20} x 10^{-4}	Ne^{21} x 10^{-6}	Ne^{22} x 10^{-5}	Ar^{36} x 10^{-4}	Ar^{38} x 10^{-5}	Ar^{40} x 10^{-4}	Kr^{84} x 10^{-8}	Xe^{132} x 10^{-8}
< 63 (1400 μg)	0.540 ±0.022	1.232 ±0.033	5.955 ±0.165	2.127 ±0.091	4.805 ±0.138	0.698 ±0.019	1.330 ±0.030	2.474 ±0.067	2.216 ±0.138	0.612 ±0.103
63-74 (1085 μg)	0.482 ±0.017	0.989 ±0.026	5.101 ±0.137	2.035 ±0.087	4.060 ±0.138	0.654 ±0.015	1.235 ±0.030	2.295 ±0.053	1.978 ±0.141	0.548 ±0.101
74-88 (1542.5 μg)	0.419 ±0.015	0.892 ±0.024	4.848 ±0.129	1.979 ±0.086	3.880 ±0.116	0.613 ±0.014	1.172 ±0.027	2.217 ±0.051	1.842 ±0.125	0.556 ±0.093
88-105 (1783.5 μg)	0.384 ±0.013	0.753 ±0.020	4.278 ±0.090	1.865 ±0.065	3.506 ±0.103	0.530 ±0.012	1.014 ±0.023	1.963 ±0.045	1.593 ±0.100	0.504 ±0.081
105-250 (2446.5 μg)	0.405 ±0.012	0.837 ±0.022	4.277 ±0.113	1.877 ±0.063	3.438 ±0.095	0.545 ±0.012	1.071 ±0.031	2.209 ±0.051	1.722 ±0.108	0.428 ±0.086
250-354 (2262.5 μg)	0.343 ±0.011	0.704 ±0.019	4.130 ±0.109	1.827 ±0.064	3.380 ±0.095	0.579 ±0.015	1.140 ±0.031	2.309 ±0.064	1.724 ±0.105	0.586 ±0.093
354-500 (1730 μg)	0.389 ±0.014	0.789 ±0.021	4.200 ±0.111	1.719 ±0.074	3.420 ±0.104	0.669 ±0.015	1.300 ±0.029	2.754 ±0.064	2.085 ±0.130	0.806 ±0.120
> 500 (4835 μg)	0.369 ±0.011	0.577 ±0.015	3.491 ±0.092	1.597 ±0.045	2.789 ±0.074	0.433 ±0.010	0.835 ±0.019	1.819 ±0.041	1.210 ±0.071	0.462 ±0.044

TABLE 2 (CONTINUED 3)

Sample: 15421 (Station 7)

Size (μm)	$\frac{He^4}{He^3}$	$\frac{Ne^{20}}{Ne^{22}}$	$\frac{Ne^{21}}{Ne^{22}}$	$\frac{Ar^{36}}{Ar^{38}}$	$\frac{Ar^{40}}{Ar^{36}}$	$\frac{He^4}{Ne^{20}}$	$\frac{Ne^{20}}{Ar^{36}}$	$\frac{Ar^{36}}{Kr^{84}}$	$\frac{Kr^{84}}{Xe^{132}}$
< 63	2270 ±111	12.51 ±0.51	0.0443 ±0.0023	5.245 ±0.184	3.545 ±0.135	20.68 ±0.79	8.533 ±0.305	3150 ±214	3.62 ±0.65
63-74	2052 ± 90	12.69 ±0.56	0.0501 ±0.0027	5.293 ±0.176	3.510 ±0.115	19.38 ±0.73	7.802 ±0.275	3306 ±248	3.61 ±0.71
74-88	2129 ± 95	12.62 ±0.51	0.0510 ±0.0027	5.229 ±0.168	3.617 ±0.117	18.40 ±0.69	7.911 ±0.277	3328 ±238	3.32 ±0.60
88-105	1961 ± 86	12.20 ±0.44	0.0532 ±0.0024	5.229 ±0.168	3.704 ±0.119	20.24 ±0.76	8.072 ±0.278	3327 ±222	3.16 ±0.55
105-250	2065 ± 82	12.44 ±0.47	0.0545 ±0.0023	5.085 ±0.186	4.054 ±0.131	19.57 ±0.73	7.851 ±0.273	3124 ±210	4.02 ±0.84
250-354	2050 ± 86	12.22 ±0.47	0.0540 ±0.0024	5.076 ±0.192	3.991 ±0.154	17.05 ±0.64	7.138 ±0.267	3358 ±222	2.94 ±0.50
354-500	2030 ± 89	12.28 ±0.49	0.0502 ±0.0026	5.145 ±0.164	4.116 ±0.133	18.79 ±0.70	6.276 ±0.219	3209 ±213	2.59 ±0.42
> 500	1564 ± 63	12.51 ±0.47	0.0572 ±0.0022	5.195 ±0.164	4.195 ±0.134	16.54 ±0.62	8.053 ±0.279	3578 ±226	2.62 ±0.30

TABLE 2 (CONTINUED 4)

Sample: 15501 (Station 9)

Size (μm)	He^3 x 10^{-5}	He^4 x 10^{-2}	Ne^{20} x 10^{-4}	Ne^{21} x 10^{-6}	Ne^{22} x 10^{-5}	Ar^{36} x 10^{-4}	Ar^{38} x 10^{-5}	Ar^{40} x 10^{-4}	Kr^{84} x 10^{-8}	Xe^{132} x 10^{-8}
< 63 (1775 μg)	1.518 ±0.057	3.353 ±0.102	7.509 ±0.200	2.499 ±0.133	5.913 ±0.154	1.441 ±0.032	2.685 ±0.061	1.254 ±0.029	5.152 ±0.295	0.885 ±0.122
63-74 (572.5 μg)	1.395 ±0.047	2.838 ±0.079	6.879 ±0.191	2.474 ±0.132	5.263 ±0.153	1.276 ±0.031	2.354 ±0.059	1.092 ±0.028	4.678 ±0.255	0.873 ±0.150
74-88 (1364 μg)	1.210 ±0.039	2.334 ±0.062	5.613 ±0.150	2.168 ±0.127	4.476 ±0.133	1.145 ±0.026	2.188 ±0.050	1.047 ±0.025	4.023 ±0.253	0.715 ±0.158
88-105 (832 μg)	1.057 ±0.028	2.185 ±0.059	5.325 ±0.059	1.980 ±0.086	4.197 ±0.119	1.045 ±0.024	1.961 ±0.045	0.997 ±0.024	3.728 ±0.024	0.686 ±0.135
105-250 (2998.5 μg)	1.100 ±0.039	2.115 ±0.063	5.214 ±0.138	1.949 ±0.100	4.088 ±0.108	1.141 ±0.026	2.205 ±0.049	1.239 ±0.031	4.292 ±0.250	-- --
250-354 (2170 μg)	1.188 ±0.039	2.129 ±0.056	4.764 ±0.126	1.900 ±0.087	3.766 ±0.104	1.069 ±0.024	2.010 ±0.045	1.097 ±0.026	3.969 ±0.310	0.675 ±0.097
354-500	--	--	--	--	--	--	--	--	--	--
500-700 (2886 μg)	0.512 ±0.014	0.830 ±0.022	2.248 ±0.059	1.157 ±0.046	1.787 ±0.057	0.541 ±0.012	1.044 ±0.023	0.713 ±0.017	2.140 ±0.121	0.329 ±0.049
> 700 (3095 μg)	0.351 ±0.010	0.806 ±0.021	3.075 ±0.081	1.130 ±0.044	2.430 ±0.068	1.058 ±0.024	2.009 ±0.045	0.831 ±0.020	4.095 ±0.133	0.676 ±0.069

TABLE 2 (CONTINUED 5)

Sample: 15501 (Station 9)

Size (μm)	$\frac{He^4}{He^3}$	$\frac{Ne^{20}}{Ne^{22}}$	$\frac{Ne^{21}}{Ne^{22}}$	$\frac{Ar^{36}}{Ar^{38}}$	$\frac{Ar^{40}}{Ar^{36}}$	$\frac{He^4}{Ne^{20}}$	$\frac{Ne^{20}}{Ar^{36}}$	$\frac{Ar^{36}}{Kr^{84}}$	$\frac{Kr^{84}}{Xe^{132}}$
< 63	2209 ±107	12.82 ±0.49	0.0422 ±0.0025	5.365 ±0.171	0.870 ±0.028	44.66 ±1.81	5.212 ±0.182	2797 ±172	5.82 ±0.87
63-74	2034 ± 88	13.20 ±0.69	0.0470 ±0.0029	5.422 ±0.189	0.855 ±0.030	41.25 ±1.62	5.388 ±0.199	2728 ±163	5.36 ±0.97
74-88	1930 ± 80	12.66 ±0.52	0.0484 ±0.0032	5.235 ±0.168	0.914 ±0.030	41.59 ±1.57	4.900 ±0.172	2846 ±179	5.62 ±1.29
88-105	2066 ± 77	12.81 ±0.61	0.0471 ±0.0024	5.328 ±0.172	0.954 ±0.032	41.04 ±1.55	5.098 ±0.178	2830 ±187	5.43 ±1.12
105-250	1923 ± 80	12.75 ±0.48	0.0476 ±0.0027	5.175 ±0.179	1.086 ±0.037	40.51 ±1.62	4.570 ±0.171	2658 ±166	-- --
250-354	1792 ± 75	12.65 ±0.48	0.0504 ±0.0027	5.318 ±0.169	1.026 ±0.034	44.69 ±1.67	4.457 ±0.155	2693 ±219	5.88 ±1.03
354-500	--	--	--	--	--	--	--	--	--
500-700	1620 ± 61	12.58 ±0.52	0.0647 ±0.0032	5.179 ±0.164	1.318 ±0.043	36.91 ±1.38	4.156 ±0.144	2528 ±154	6.51 ±1.03
> 700	2297 ± 89	12.66 ±0.49	0.0464 ±0.0022	5.267 ±0.167	0.785 ±0.026	26.20 ±0.98	2.907 ±0.101	2584 ±102	6.06 ±0.65

TABLE 2 (CONTINUED 6)

Sample: 15511 (Station 9)

Size (μm)	He^3 x 10^{-5}	He^4 x 10^{-2}	Ne^{20} x 10^{-4}	Ne^{21} x 10^{-6}	Ne^{22} x 10^{-5}	Ar^{36} x 10^{-4}	Ar^{38} x 10^{-5}	Ar^{40} x 10^{-4}	Kr^{84} x 10^{-8}	Xe^{132} x 10^{-8}
< 63 (1371.5 μg)	1.779 ±0.043	3.581 ±0.073	8.477 ±0.192	2.884 ±0.115	6.663 ±0.193	1.259 ±0.029	2.360 ±0.063	1.358 ±0.032	4.286 ±0.254	0.816 ±0.164
63-74 (755 μg)	1.560 ±0.045	3.195 ±0.087	6.564 ±0.179	2.588 ±0.120	5.213 ±0.150	1.154 ±0.027	2.198 ±0.052	1.280 ±0.032	4.412 ±0.265	0.738 ±0.148
74-88 (1123.5 μg)	1.478 ±0.047	3.098 ±0.083	6.638 ±0.178	2.509 ±0.119	5.243 ±0.158	1.141 ±0.026	2.118 ±0.049	1.091 ±0.026	3.953 ±0.302	0.597 ±0.128
88-105 (1589 μg)	1.340 ±0.046	2.592 ±0.069	5.745 ±0.153	2.327 ±0.114	4.556 ±0.128	1.049 ±0.024	1.985 ±0.045	1.148 ±0.026	3.823 ±0.225	0.719 ±0.138
105-250 (2482.5 μg)	1.103 ±0.034	2.062 ±0.055	4.930 ±0.131	2.018 ±0.095	3.964 ±0.106	0.871 ±0.020	1.649 ±0.040	0.813 ±0.020	3.142 ±0.145	0.468 ±0.057
250-354 (1459 μg)	1.030 ±0.028	2.033 ±0.054	4.732 ±0.126	2.010 ±0.087	3.804 ±0.118	0.983 ±0.022	1.886 ±0.043	1.025 ±0.026	3.989 ±0.169	0.573 ±0.119
354-500 (2280 μg)	0.646 ±0.017	1.013 ±0.027	2.704 ±0.072	1.392 ±0.053	2.157 ±0.063	0.862 ±0.019	1.703 ±0.038	2.051 ±0.048	2.972 ±0.155	0.887 ±0.172
500-700 (3727.5 μg)	0.861 ±0.025	1.541 ±0.034	4.036 ±0.107	1.904 ±0.081	3.188 ±0.084	0.799 ±0.018	1.541 ±0.034	1.256 ±0.029	2.703 ±0.103	0.486 ±0.057
> 700 (3800 μg)	1.425 ±0.045	3.136 ±0.094	7.045 ±0.186	2.546 ±0.083	5.770 ±0.152	1.551 ±0.042	3.111 ±0.071	1.555 ±0.044	6.028 ±0.212	1.112 ±0.127

TABLE 2 (CONTINUED 7)

Sample: 15511 (Station 9)

Size (μm)	$\frac{He^4}{He^3}$	$\frac{Ne^{20}}{Ne^{22}}$	$\frac{Ne^{21}}{Ne^{22}}$	$\frac{Ar^{36}}{Ar^{38}}$	$\frac{Ar^{40}}{Ar^{36}}$	$\frac{He^4}{Ne^{20}}$	$\frac{Ne^{20}}{Ar^{36}}$	$\frac{Ar^{36}}{Kr^{84}}$	$\frac{Kr^{84}}{Xe^{132}}$
< 63	2012 ± 63	12.85 ±0.48	0.0433 ±0.0021	5.333 ±0.187	1.079 ±0.035	42.24 ±1.29	6.733 ±0.216	2937 ±187	5.25 ±1.10
63-74	2048 ± 82	12.72 ±0.50	0.0496 ±0.0027	5.250 ±0.174	1.110 ±0.038	48.68 ±1.87	5.689 ±0.204	2616 ±169	5.98 ±1.25
74-88	2097 ± 87	12.79 ±0.53	0.0478 ±0.0027	5.387 ±0.174	0.956 ±0.032	46.68 ±1.77	5.818 ±0.205	2886 ±231	6.62 ±1.51
88-105	1934 ± 84	12.74 ±0.49	0.0510 ±0.0029	5.281 ±0.170	1.095 ±0.035	45.11 ±1.76	5.479 ±0.193	2744 ±173	7.59 ±1.52
105-250	1870 ± 75	12.44 ±0.47	0.0509 ±0.0028	5.278 ±0.174	0.933 ±0.031	41.83 ±1.57	5.663 ±0.197	2772 ±143	6.71 ±0.87
250-354	1975 ± 75	12.44 ±0.51	0.0528 ±0.0028	5.218 ±0.167	1.041 ±0.035	42.98 ±1.62	4.807 ±0.168	2464 ±119	6.96 ±1.47
354-500	1569 ± 59	12.53 ±0.50	0.0645 ±0.0031	5.062 ±0.161	2.380 ±0.077	37.47 ±1.40	3.138 ±0.109	2900 ±164	3.35 ±0.67
500-700	1790 ± 75	12.66 ±0.47	0.0597 ±0.0031	5.189 ±0.164	1.571 ±0.051	38.18 ±1.53	5.048 ±0.175	2956 ±131	5.56 ±0.68
> 700	2201 ± 96	12.21 ±0.46	0.0441 ±0.0018	4.986 ±0.176	1.002 ±0.039	44.51 ±1.78	4.543 ±0.171	2523 ±112	5.42 ±0.65

TABLE 2 (CONTINUED 8)

Sample: 15080 (Station 1)

Size (μm)	He^3 x 10^{-5}	He^4 x 10^{-2}	Ne^{20} x 10^{-4}	Ne^{21} x 10^{-6}	Ne^{22} x 10^{-5}	Ar^{36} x 10^{-4}	Ar^{38} x 10^{-5}	Ar^{40} x 10^{-4}	Kr^{84} x 10^{-8}	Xe^{132} x 10^{-8}
Non-magnetic > 500 (3945 μg)	0.534 ±0.018	0.204 ±0.005	0.309 ±0.082	0.825 ±0.033	0.350 ±0.012	0.063 ±0.002	0.180 ±0.005	0.233 ±0.006	0.259 ±0.037	-- --
Magnetic > 500	1.917 ±0.057	4.630 ±0.139	1.562 ±0.041	0.442 ±0.013	1.199 ±0.032	2.919 ±0.077	5.370 ±0.142	5.934 ±0.158	11.22 ±0.325	2.013 ±0.116

TABLE 2 (CONTINUED 9)

Sample: 15080 (Station 1)

Size (μm)	$\frac{He^4}{He^3}$	$\frac{Ne^{20}}{Ne^{22}}$	$\frac{Ne^{21}}{Ne^{22}}$	$\frac{Ar^{36}}{Ar^{38}}$	$\frac{Ar^{40}}{Ar^{36}}$	$\frac{He^4}{Ne^{20}}$	$\frac{Ne^{20}}{Ar^{36}}$	$\frac{Ar^{36}}{Kr^{84}}$	$\frac{Kr^{84}}{Xe^{132}}$
Non-magnetic > 500	382 ± 16	8.84 ±0.38	0.236 ±0.012	3.499 ±0.118	3.697 ±0.129	65.95 ±2.47	4.905 ±0.170	2432 ±357	-- --
Magnetic > 500	2415 ±102	13.03 ±0.49	0.0369 ±0.0014	5.436 ±0.203	2.033 ±0.076	29.63 ±1.18	5.353 ±0.200	2601 ±165	5.58 ±0.36

TABLE 3

COMPARISON OF n VALUES FOR LUNAR FINES

[Best fit to $C(cm^3\ STP/g) = KD^{-n}(\mu m)$]

Sample	n_4	n_{20}	n_{36}	n_{84}	n_{132}	Reference
Apollo 11						
10084(bf)	0.64	0.59	0.60	0.55*	0.56	Eberhardt et
10084(ilm)	1.15	1.11	0.96	0.98	0.82	al., 1972
10046(ilm)	1.16	1.13	0.67	0.74*	0.89	
10087(bf)	0.70	0.65	0.60	0.57	0.50	Hintenberger
10061(br)	1.01	1.00	0.94	0.76	0.83	and Weber, 1973
10021(br)	1.15	1.15	1.09	1.12	1.15	
Apollo 12						
12001(bf)	0.71	0.60	0.56	0.58*	0.56	Eberhardt et
12001(ilm)	1.15	1.11	0.96	0.98*	0.82	al., 1972
Apollo 15						
15471(bf)	0.89	0.80	0.75	0.74	0.71	Hintenberger and Weber, 1973
15071(bf)	0.56	0.44	0.40	0.38	0.32	This work
Apollo 16						
61221(bf)	0.86	0.69	0.63	0.60	0.56	Heymann et al.,
61241(bf)	0.68	0.70	0.60	0.58	0.52	1975
67701(bf)	0.79	0.72	0.71	0.10	0.61	

TABLE 3 (CONTINUED)

Sample	n_4	n_{20}	n_{36}	n_{84}	n_{132}	Reference
Apollo 17						
76321(bf) 76501(bf) **	0.59	0.57	0.49	0.45	0.45	Bogard et al., 1974
74220 (orange soil)	1.10	1.00	0.95	0.88	0.85	Hintenberger
74241 (gray soil with orange soil)	1.07	0.98	0.85	0.81	0.82	and Weber, 1973

* these values are for n_{86}

**average of these two soils

bf = bulk fines

br = breccias

ilm = ilmenite

TABLE 4

COMPOSITION OF APOLLO 15 FINES

(mass percent)

	15021	15301	15101	15601
*Oxides				
SiO_2	46.56	45.91	45.95	45.05
TiO_2	1.75	1.17	1.27	1.19
Al_2O_3	13.73	14.53	17.38	5.40
FeO	15.21	14.05	11.65	19.79
MgO	10.37	12.12	10.36	6.57
CaO	10.54	10.70	11.52	9.87
Element				
Si	21.76	21.46	21.46	21.06
Ti	1.05	0.70	0.76	1.19
Al	7.27	7.69	9.20	5.40
Fe	8.31	7.63	6.32	10.74
Mg	6.22	7.31	6.25	6.57
Ca	7.53	7.65	8.23	7.05

* Data from LSPET (1972)

TABLE 5

NE^{21}_{C} RADIATION AGES OF APOLLO 15 FINES

Sample	Size (μm)	Ne^{21}_{C} (10^{-7} cm^3 STP/g)	Ages, 10^6 yr Ne^{21}_{C}
15071	63-74	4.12 ± 0.87	250 ± 50
	74-88	4.01 ± 0.72	240 ± 40
	88-250	4.07 ± 0.65	250 ± 40
	250-354	4.07 ± 0.45	250 ± 30
	354-500	6.19 ± 0.59	380 ± 40
	500-700	5.83 ± 0.49	360 ± 30
15091	< 44	2.80 ± 3.51	170 ± 210
	44-53	3.43 ± 1.51	210 ± 90
	53-63	3.55 ± 1.21	220 ± 70
	63-74	3.74 ± 1.11	230 ± 70
	74-88	3.15 ± 0.97	190 ± 60
	88-105	2.99 ± 1.02	180 ± 60
	105-250	3.52 ± 0.87	210 ± 50
	250-354	3.52 ± 0.79	210 ± 50
	354-500	1.96 ± 0.45	120 ± 30
	500-700	3.35 ± 0.70	200 ± 40
15421	< 63	6.70 ± 1.10	410 ± 70
	63-74	8.11 ± 1.06	490 ± 60
	74-88	8.11 ± 1.02	490 ± 60
	88-105	8.12 ± 0.82	490 ± 50

TABLE 5 (CONTINUED 1)

Sample	Size (μm)	Ne^{21}_C (10^{-7} cm^3 STP/g)	Ages, 10^6 yr Ne^{21}_C
15421	105-250	8.46 ± 0.79	520 ± 50
	250-354	8.13 ± 0.80	500 ± 50
	354-500	6.89 ± 0.89	420 ± 50
	500-700	7.63 ± 0.60	470 ± 40
15501	< 63	3.56 ± 1.88	220 ± 120
	63-74	5.76 ± 1.87	350 ± 110
	74-88	5.56 ± 1.73	340 ± 110
	88-105	4.67 ± 1.36	280 ± 80
	105-250	4.76 ± 1.34	290 ± 80
	250-354	5.47 ± 1.33	330 ± 80
	354-500	------	----
	500-700	5.25 ± 0.78	320 ± 50
	> 700	2.53 ± 0.74	150 ± 40
15601	< 44	4.83 ± 4.60	290 ± 276
	44-53	3.26 ± 1.67	200 ± 100
	53-63	2.79 ± 1.17	170 ± 70
	63-74	3.83 ± 1.31	230 ± 80
	74-88	3.44 ± 1.25	210 ± 80
	88-105	3.91 ± 1.13	240 ± 70
	105-250	3.66 ± 1.04	220 ± 60
	250-354	4.89 ± 0.80	300 ± 50

TABLE 5 (CONTINUED 2)

Sample	Size (μm)	Ne^{21}_C (10^{-7} cm^3 STP/g)	Ages, 10^6 yr Ne^{21}_C
15601	354-500	6.01 ± 0.68	370 ± 40
	500-700	3.74 ± 0.51	230 ± 30
15511	< 63	4.72 ± 1.92	290 ± 120
	63-74	7.14 ± 1.84	430 ± 110
	74-88	6.20 ± 1.80	380 ± 110
	88-105	6.91 ± 1.68	420 ± 100
	105-250	5.95 ± 1.43	360 ± 90
	250-354	6.47 ± 1.39	390 ± 80
	354-500	6.29 ± 0.91	380 ± 50
	500-700	7.70 ± 1.29	470 ± 80
	> 700	4.59 ± 1.56	280 ± 90
15080 Nonmagnetic	> 500	7.40 ± 0.37	450 ± 20
15080 Magnetic	> 500	0.76 ± 0.18	46 ± 10

TABLE 6

APPARENT K^{40}-Ar^{40} AGES FROM APOLLO 15 FINES

(based on $Ar^{40}_{intercept}$ values from plots of Ar^{40} vs. Ar^{36} for size fractions)

Sample	$Ar^{40}_{intercept}$ (10^{-4} cm^3 STP/g)	K (ppm)	Apparent K^{40}-Ar^{40} Age (10^9 y)	K reference
15071 Station 1	0.140	1141*	1.8	**
15091 Station 2	0.332+	1494	2.6	Carran et al., 1972
15421 Station 7	0.301	913	3.2	LSPET, 1972
15501 Station 9	0.246	1328	2.4	LSPET, 1972
15601 Station 9A	0.120++	830	2.0	LSPET, 1972

+Ar^{40} intercept from Jordan et al., 1973.

++Ar^{40} intercept from Yaniv and Heymann, 1972.

*Based on assumed constant Na_2O/K_2O ratio between fines 15071 and 15081 (station 1).

**Na_2O of 15071 from Fruchter et al., 1973; Na_2O and K_2O from Wänke et al., 1973.

TABLE 7

INERT GAS CONTENTS AND ISOTOPIC AND ELEMENTAL RATIOS
OF APOLLO 17 BULK FINES

(UNITS: cm^3 STP/g)

Sample & Weight	He^3 x 10^{-5}	He^4 x 10^{-1}	Ne^{20} x 10^{-3}	Ne^{21} x 10^{-6}	Ne^{22} x 10^{-4}	Ar^{36} x 10^{-4}	Ar^{38} x 10^{-5}	Ar^{40} x 10^{-4}	Kr^{84} x 10^{-8}	Xe^{132} x 10^{-8}
Station 2:										
72141 (2249 µg)	5.698	1.489	2.335	6.295	1.793	4.01	7.955	6.073	15.49	2.892
72161 (2426 µg)	6.777	1.664	2.802	7.502	2.180	4.923	9.219	7.680	18.36	2.696
72321 (2280 µg)	1.874	0.719	1.498	3.924	1.145	3.276	6.078	6.120	12.80	1.783
72441 (2415 µg)	2.236	0.678	1.682	4.530	1.280	3.597	6.696	5.608	12.76	2.267
72461 (2301.5 µg)	2.758	0.738	1.554	4.406	1.183	3.272	6.063	6.674	12.17	1.871
72501 (2381.5 µg)	3.250	0,867	1.837	4.779	1.381	3.650	6.779	9.048	14.41	2.539
Station 3:										
73121 (2551 µg)	2.804	0.734	1.604	4.417	1.223	3.669	6.786	6.238	13.36	2.232
73141 (2326 µg)	2.263	0.595	1.238	3.356	0.948	2.534	4.567	6.578	10.38	1.836

TABLE 7 (CONTINUED 1)

Sample & Weight	He^3 x 10^{-5}	He^4 x 10^{-1}	Ne^{20} x 10^{-3}	Ne^{21} x 10^{-6}	Ne^{22} x 10^{-4}	Ar^{36} x 10^{-4}	Ar^{38} x 10^{-5}	Ar^{40} x 10^{-4}	Kr^{84} x 10^{-8}	Xe^{132} x 10^{-8}
Station 4:										
74220 (3957 µg)	0.433	0.111	0.133	0.372	0.101	0.153	0.287	3.383	1.676	0.315
74241 (2770 µg)	5.023	1.676	1.438	3.755	1.111	1.774	3.332	14.06	4.489	1.627
Station 5:										
75081 (2142 µg)	6.879	1.365	2.152	5.913	1.620	3.106	5.853	8.726	13.70	2.42
75121 (2494.5 µg)	6.04	1.440	2.180	5.620	1.650	4.490	8.38	9.160	20.30	3.34
Station 9:										
79221 (1952 µg)	11.16	2.922	4.560	11.97	3.510	5.970	11.33	8.870	15.85	2.410
79241 (4799.5 µg)	5.476	1.348	2.401	7.164	1.870	3.163	5.913	4.978	7.853	1.282
(1949 µg)*	6.934	1.756	2.841	7.645	2.211	3.770	7.090	6.460	12.63	2.360
79261 (4775 µg)	5.000	1.230	2.117	5.734	1.669	2.724	5.127	5.231	8.843	1.583
(1057.7 µg)*	7.591	1.801	2.858	7.544	2.212	3.823	6.900	6.090	12,24	2.117

* repeat runs

TABLE 7 (CONTINUED 2)

Sample	$\frac{He^4}{He^3}$	$\frac{Ne^{20}}{Ne^{22}}$	$\frac{Ne^{21}}{Ne^{22}}$	$\frac{Ar^{36}}{Ar^{38}}$	$\frac{Ar^{40}}{Ar^{36}}$	$\frac{He^4}{Ne^{20}}$	$\frac{Ne^{20}}{Ar^{36}}$	$\frac{Ar^{36}}{Kr^{84}}$	$\frac{Kr^{84}}{Xe^{132}}$
Station 2:									
72141	2613	13.02	0.0351	5.039	1.515	63.77	5.823	2588	5.35
72161	2455	12.82	0.0343	5.340	1.560	59.39	5.692	2681	6.81
72321	3835	13.08	0.0343	5.390	1.868	47.98	4.573	2559	7.18
72441	3034	13.17	0.0355	5.372	1.559	40.30	4.676	2819	5.63
72461	2676	13.14	0.0342	5.397	2.040	47.48	4.750	2689	6.50
72501	2669	13.30	0.0346	5.384	2.479	47.22	5.033	2533	5.68
Station 3:									
73121	2619	13.11	0.0361	5.407	1.70	45.79	4.372	2746	4.48
73141	2630	13.06	0.0354	5.548	2.596	48.08	4.886	2441	5.65

TABLE 7 (CONTINUED 3)

Sample	$\frac{He^4}{He^3}$	$\frac{Ne^{20}}{Ne^{22}}$	$\frac{Ne^{21}}{Ne^{22}}$	$\frac{Ar^{36}}{Ar^{38}}$	$\frac{Ar^{40}}{Ar^{36}}$	$\frac{He^4}{Ne^{20}}$	$\frac{Ne^{20}}{Ar^{36}}$	$\frac{Ar^{36}}{Kr^{84}}$	$\frac{Kr^{84}}{Xe^{132}}$
Station 4:									
74220	2630	13.06	0.0354	5.548	2.596	48.08	4.886	2441	5.32
74241	3337	12.94	0.338	5.324	7.925	116.55	8.106	3952	2.76
Station 5:									
75081	1984	13.28	0.0365	5.307	2.809	63.43	6.928	2267	5.66
75121	2384	13.18	0.0340	5.360	2.040	66.06	4.86	2112	6.08
Station 9:									
79221	2618	12.99	0.0341	5.271	1.486	64.08	7.637	3767	6.57
79241	2462	12.84	0.0383	5.349	1.574	56.14	7.591	4028	6.13
(repeat)	2352	12.85	0.0346	5.317	1.763	61.80	7.563	2985	5.35
79261	2457	12.69	0.0344	5.313	1.920	58.10	7.772	3080	5.59
(repeat)	2372	12.92	0.0341	5.541	1.593	63.01	7.475	3123	5.31

NOTES TO TABLE 7

Errors in absolute amounts are generally ± 3% for He, Ne, and Ar; 5-10% for Kr and Xe. This includes errors in weighing, calibration of the mass spectrometer, and standard deviations of measured peakheights.

Errors in isotope ratios are generally ± 1%. Errors in element ratios (e.g. He^4/Ne^{20}) are about ± 5%.

TABLE 8

INERT GAS CONTENTS AND ISOTOPIC AND ELEMENTAL RATIOS
OF SIZE FRACTIONS OF FINES FROM APOLLO 17 TRENCH

(UNITS: cm^3 STP/g)

Sample: 79221 (Depth: 0-2 cm)

Size (μm)	He^3 x 10^{-5}	He^4 x 10^{-2}	Ne^{20} x 10^{-3}	Ne^{21} x 10^{-6}	Ne^{22} x 10^{-4}	Ar^{36} x 10^{-4}	Ar^{38} x 10^{-5}	Ar^{40} x 10^{-4}	Kr^{84} x 10^{-8}	Xe^{132} x 10^{-8}
BULK (1952 μg)	11.16 ±0.35	29.22 ±0.89	4.560 ±0.123	11.97 ±0.39	3.510 ±0.093	5.970 ±0.161	11.33 ±0.30	8.870 ±0.241	15.85 ±0.61	2.410 ±0.385
< 63 (983 μg)	9.417 ±0.297	23.32 ±0.71	4.042 ±0.109	10.74 ±0.35	3.066 ±0.081	5.464 ±0.147	10.58 ±0.28	7.814 ±0.212	16.64 ±0.64	-- --
63-74 (1815 μg)	3.537 ±0.119	9.050 ±0.272	1.577 ±0.042	4.719 ±0.220	1.271 ±0.330	-- --	-- --	-- --	-- --	-- --
63-74* (1125 μg)	2.266 ±0.076	5.321 ± 0.160	1.024 ±0.027	2.864 ±0.130	0.784 ±0.020	1.524 ±0.034	2.921 ±0.066	2.437 ±0.066	3.877 ±0.190	0.958 ±0.153
74-88 (2725 μg)	3.216 ±0.081	8.950 ±0.290	1.490 ±0.040	4.359 ±0.172	1.189 ±0.033	2.241 ±0.051	4.204 ±0.097	3.758 ±0.087	5.841 ±0.280	0.915 ±0.188

* repeat run

TABLE 8 (CONTINUED 1)

Sample: 79221 (Depth: 0-2 cm)

Size (μm)	He^3 x 10^{-5}	He^4 x 10^{-2}	Ne^{20} x 10^{-3}	Ne^{21} x 10^{-6}	Ne^{22} x 10^{-4}	Ar^{36} x 10^{-4}	Ar^{38} x 10^{-5}	Ar^{40} x 10^{-4}	Kr^{84} x 10^{-8}	Xe^{132} x 10^{-8}
88-105 (1720 μg)	3.235 ±0.107	8.430 ±0.247	1.627 ±0.043	4.782 ±0.261	1.265 ±0.033	2.518 ±0.067	4.900 ±0.131	4.344 ±0.118	7.587 ±0.461	1.489 ±0.259
105-250 (2956 μg)	3.526 ±0.125	8.850 ±0.267	1.751 ±0.043	5.049 ±0.261	1.402 ±0.038	2.854 ±0.075	5.336 ±0.139	5.100 ±0.141	8.521 ±0.507	1.749 ±0.296
250-354 (3720 μg)	2.739 ±0.110	6.750 ±0.203	1.278 ±0.034	3.646 ±0.145	1.004 ±0.027	2.317 ±0.061	4.254 ±0.113	4.182 ±0.114	6.790 ±0.412	1.511 ±0.190
354-500 (4555 μg)	2.203 ±0.193	5.784 ±0.174	1.110 ±0.030	3.133 ±0.143	0.879 ±0.024	2.084 ±0.055	3.780 ±0.099	4.397 ±0.119	6.066 ±0.410	1.138 ±0.166
500-700 (5860 μg)	2.431 ±0.072	6.595 ±0.197	1.261 ±0.033	3.441 ±0.234	0.990 ±0.026	1.951 ±0.052	3.598 ±0.095	3.427 ±0.092	5.459 ±0.226	1.211 ±0.093
> 700 (4580 μg)	1.512 ±0.053	3.480 ±0.114	0.665 ±0.017	1.626 ±0.086	0.520 ±0.016	1.057 ±0.022	2.042 ±0.046	2.404 ±0.055	3.056 ±0.168	0.550 ±0.153

TABLE 8 (CONTINUED 2)

Sample: 79221 (Depth: 0-2 cm)

Size (μm)	$\frac{He^4}{He^3}$	$\frac{Ne^{20}}{Ne^{22}}$	$\frac{Ne^{21}}{Ne^{22}}$	$\frac{Ar^{36}}{Ar^{38}}$	$\frac{Ar^{40}}{Ar^{36}}$	$\frac{He^4}{Ne^{20}}$	$\frac{Ne^{20}}{Ar^{36}}$	$\frac{Ar^{36}}{Kr^{84}}$	$\frac{Kr^{84}}{Xe^{132}}$
BULK	2618 ±114	12.99 ±0.50	0.0341 ±0.0015	5.271 ±0.200	1.486 ±0.057	64.08 ±2.60	7.637 ±0.290	3767 ±177	6.57 ±1.09
< 63	2479 ±108	13.18 ±0.51	0.0349 ±0.0015	5.164 ±0.196	1.430 ±0.055	57.71 ±2.34	7.398 ±0.281	3284 ±154	-- --
63-74	2557 ±114	12.41 ±0.48	0.0372 ±0.0019	-- --	-- --	57.36 ±2.30	-- --	-- --	-- --
63-74*	2348 ±105	13.06 ±0.50	0.0364 ±0.0019	5.217 ±0.166	1.599 ±0.056	51.93 ±2.08	6.723 ±0.234	3931 ±212	4.04 ±0.67
74-88	2783 ±114	12.52 ±0.50	0.0366 ±0.0023	5.330 ±0.173	1.677 ±0.055	60.08 ±2.34	6.648 ±0.234	3837 ±204	6.39 ±1.35

* repeat run

TABLE 8 (CONTINUED 3)

Sample: 79221 (Depth: 0-2 cm)

Size (μm)	$\frac{He^4}{He^3}$	$\frac{Ne^{20}}{Ne^{22}}$	$\frac{Ne^{21}}{Ne^{22}}$	$\frac{Ar^{36}}{Ar^{38}}$	$\frac{Ar^{40}}{Ar^{36}}$	$\frac{He^4}{Ne^{20}}$	$\frac{Ne^{20}}{Ar^{36}}$	$\frac{Ar^{36}}{Kr^{84}}$	$\frac{Kr^{84}}{Xe^{132}}$
88-105	2606 ±115	12.86 ±0.49	0.0377 ±0.0019	5.150 ±0.167	1.725 ±0.065	51.83 ±1.72	6.461 ±0.242	3319 ±220	5.10 ±0.94
105-250	2510 ±117	12.50 ±0.48	0.0360 ±0.0023	5.348 ±0.201	1.787 ±0.068	50.53 ±2.04	6.135 ±0.228	3349 ±218	4.87 ±0.88
250-354	2463 ±124	12.73 ±0.49	0.0363 ±0.0018	5.447 ±0.204	1.805 ±0.204	52.78 ±2.13	5.278 ±0.199	3412 ±226	4.49 ±0.81
354-500	2626 ±111	12.63 ±0.49	0.0356 ±0.0017	5.513 ±0.207	2.110 ±0.080	52.11 ±2.09	5.326 ±0.200	3435 ±249	5.33 ±0.75
500-700	2713 ±115	12.73 ±0.49	0.0347 ±0.0015	5.423 ±0.202	1.756 ±0.065	52.30 ±2.10	6.463 ±0.241	3574 ±176	4.51 ±0.40
> 700	2303 ±110	12.78 ±0.52	0.0313 ±0.0019	5.175 ±0.165	2.275 ±0.074	52.36 ±2.23	6.288 ±0.219	3459 ±203	5.56 ±1.58

TABLE 8 (CONTINUED 4)

Sample: 79241 (Depth: 2-7 cm)

Size (μm)	He^3 x 10^{-5}	He^4 x 10^{-2}	Ne^{20} x 10^{-3}	Ne^{21} x 10^{-6}	Ne^{22} x 10^{-4}	Ar^{36} x 10^{-4}	Ar^{38} x 10^{-5}	Ar^{40} x 10^{-4}	Kr^{84} x 10^{-8}	Xe^{132} x 10^{-8}
BULK (4799.5 μg)	5.476 ±0.169	13.48 ±0.409	2.401 ±0.065	7.164 ±0.269	1.870 ±0.051	3.163 ±0.085	5.913 ±0.135	4.978 ±0.135	7.853 ±0.353	1.282 ±0.179
BULK* (1949 μg)	6.934 ±0.214	17.56 ±0.53	2.841 ±0.077	7.645 ±0.284	2.211 ±0.060	3.770 ±0.101	7.090 ±0.162	6.460 ±0.175	12.63 ±0.57	2.360 ±0.330
< 63 (944 μg)	8.935 ±0.293	20.86 ±0.64	3.780 ±0.102	9.434 ±0.334	2.803 ±0.074	4.417 ±0.119	8.105 ±0.219	7.578 ±0.206	12.53 ±0.79	2.136 ±0.332
63-74 (2275 μg)	2.762 ±0.101	5.942 ±0.190	1.128 ±0.030	3.631 ±0.144	0.887 ±0.024	1.524 ±0.035	2.922 ±0.076	2.735 ±0.064	4.302 ±0.205	0.872 ±0.205
74-88 (2120 μg)	2.749 ±0.069	6.092 ±0.197	1.160 ±0.031	3.634 ±0.144	0.934 ±0.026	1.523 ±0.035	2.867 ±0.066	2.759 ±0.064	4.311 ±0.242	0.907 ±0.186
88-105 (2137.5 μg)	2.600 ±0.086	5.770 ±0.174	1.086 ±0.028	3.602 ±0.192	0.862 ±0.023	1.497 ±0.040	2.820 ±0.075	2.770 ±0.075	4.035 ±0.245	0.810 ±0.141

* repeat run

TABLE 8 (CONTINUED 5)

Sample: 79241 (Depth: 2-7 cm)

Size (μm)	He^3 x 10^{-5}	He^4 x 10^{-2}	Ne^{20} x 10^{-3}	Ne^{21} x 10^{-6}	Ne^{22} x 10^{-4}	Ar^{36} x 10^{-4}	Ar^{38} x 10^{-5}	Ar^{40} x 10^{-4}	Kr^{84} x 10^{-8}	Xe^{132} x 10^{-8}
105-250 (2236 μg)	2.081 ±0.074	4.421 ±0.133	0.868 ±0.023	2.991 ±0.167	0.695 ±0.019	1.444 ±0.038	2.723 ±0.085	2.614 ±0.072	4.086 ±0.243	0.808 ±0.137
250-354 (2863.5 μg)	2.736 ±0.110	5.897 ±0.177	1.213 ±0.032	3.793 ±0.150	0.958 ±0.027	1.701 ±0.045	3.207 ±0.085	3.699 ±0.102	3.950 ±0.235	1.136 ±0.119
354-500 (4065 μg)	1.647 ±0.091	3.357 ±0.101	0.691 ±0.019	2.466 ±0.113	0.544 ±0.015	0.991 ±0.026	1.953 ±0.051	2.003 ±0.054	2.690 ±0.168	0.616 ±0.085
500-700 (4728.5 μg)	1.572 ±0.087	3.596 ±0.108	0.821 ±0.023	2.484 ±0.114	0.659 ±0.018	1.744 ±0.046	3.163 ±0.083	4.468 ±0.120	4.644 ±0.290	0.886 ±0.122
> 500 (4330 μg)	2.634 ±0.074	6.665 ±0.200	1.118 ±0.029	3.462 ±0.235	0.893 ±0.023	-- --	-- --	-- --	-- --	-- --
> 700 (7100 μg)	2.112 ±0.117	5.263 ±0.158	1.028 ±0.029	3.424 ±0.157	0.810 ±0.022	1.216 ±0.032	2.290 ±0.060	3.706 ±0.100	2.820 ±0.176	0.755 ±0.104

TABLE 8 (CONTINUED 6)

Sample: 79241 (Depth: 2-7 cm)

Size (μm)	$\frac{He^4}{He^3}$	$\frac{Ne^{20}}{Ne^{22}}$	$\frac{Ne^{21}}{Ne^{22}}$	$\frac{Ar^{36}}{Ar^{38}}$	$\frac{Ar^{40}}{Ar^{36}}$	$\frac{He^4}{Ne^{20}}$	$\frac{Ne^{20}}{Ar^{36}}$	$\frac{Ar^{36}}{Kr^{84}}$	$\frac{Kr^{84}}{Xe^{132}}$
BULK	2462 ±105	12.84 ±0.52	0.0383 ±0.0019	5.349 ±0.188	1.574 ±0.061	56.14 ±2.28	7.591 ±0.289	4028 ±211	6.13 ±1.02
BULK*	2532 ±108	12.85 ±0.50	0.0346 ±0.0017	5.317 ±0.187	1.763 ±0.068	61.80 ±2.51	7.563 ±0.288	2985 ±157	5.35 ±0.89
< 63	2335 ±104	13.49 ±0.52	0.0336 ±0.0017	5.450 ±0.208	1.715 ±0.066	55.19 ±2.24	8.558 ±0.326	3525 ±242	5.87 ±0.98
63-74	2151 ±102	12.72 ±0.50	0.0409 ±0.0020	5.215 ±0.168	1.795 ±0.058	52.68 ±2.20	7.402 ±0.260	3542 ±187	4.93 ±1.18
74-88	2216 ±105	12.42 ±0.50	0.0389 ±0.0019	5.312 ±0.172	1.812 ±0.059	52.51 ±2.21	7.616 ±0.256	3533 ±214	4.75 ±1.00
88-105	2219 ± 98	12.60 ±0.48	0.0418 ±0.0026	5.310 ±0.199	1.850 ±0.070	53.13 ±2.13	7.254 ±0.271	3710 ±246	4.98 ±0.96

* repeat run

TABLE 8 (CONTINUED 7)

Sample: 79241 (Depth: 2-7 cm)

Size (μm)	$\frac{He^4}{He^3}$	$\frac{Ne^{20}}{Ne^{22}}$	$\frac{Ne^{21}}{Ne^{22}}$	$\frac{Ar^{36}}{Ar^{38}}$	$\frac{Ar^{40}}{Ar^{36}}$	$\frac{He^4}{Ne^{20}}$	$\frac{Ne^{20}}{Ar^{36}}$	$\frac{Ar^{36}}{Kr^{84}}$	$\frac{Kr^{84}}{Xe^{132}}$
105-250	2182 ±102	12.50 ±0.48	0.0431 ±0.0027	5.301 ±0.200	1.811 ±0.069	56.11 ±2.36	6.010 ±0.237	3534 ±230	5.06 ±0.91
250-354	2155 ±108	12.66 ±0.48	0.0396 ±0.0019	5.304 ±0.199	2.174 ±0.083	48.62 ±1.95	7.131 ±0.267	3585 ±233	5.02 ±0.59
354-500	2038 ±127	12.69 ±0.49	0.0453 ±0.0024	5.073 ±0.190	2.022 ±0.077	48.61 ±1.95	6.971 ±0.262	3684 ±250	4.37 ±0.67
500-700	2287 ±108	12.47 ±0.48	0.0377 ±0.0020	5.514 ±0.207	2.562 ±0.098	43.79 ±1.76	4.708 ±0.177	3755 ±255	5.24 ±0.80
> 500	2530 ±107	12.52 ±0.48	0.0388 ±0.0017	-- --	-- --	59.61 ±2.39	-- --	-- --	-- --
> 700	2492 ±157	12.69 ±0.49	0.0423 ±0.0022	5.310 ±0.199	3.048 ±0.117	51.20 ±2.06	8.454 ±0.318	4312 ±292	3.74 ±0.57

TABLE 8 (CONTINUED 8)

Sample: 79261 (Depth: 7-17 cm)

Size (μm)	He^3 x 10^{-5}	He^4 x 10^{-2}	Ne^{20} x 10^{-3}	Ne^{21} x 10^{-6}	Ne^{22} x 10^{-4}	Ar^{36} x 10^{-4}	Ar^{38} x 10^{-5}	Ar^{40} x 10^{-4}	Kr^{84} x 10^{-8}	Xe^{132} x 10^{-8}
BULK (4775 μg)	5.000 ±0.154	12.30 ±0.373	2.117 ±0.057	5.734 ±0.215	1.669 ±0.045	2.724 ±0.073	5.127 ±0.117	5.231 ±0.142	8.843 ±0.397	1.583 ±0.221
BULK* (1057.7 μg)	7.591 ±0.248	18.01 ±0.546	2.858 ±0.077	7.544 ±0.283	2.212 ±0.059	3.823 ±0.102	6.900 ±0.158	6.090 ±0.165	12.24 ±0.55	2.117 ±0.296
< 63 (945 μg)	7.186 ±0.235	17.40 ±0.53	2.798 ±0.075	7.580 ±0.303	2.165 ±0.057	3.834 ±0.103	7.057 ±0.162	6.278 ±0.171	11.45 ±0.79	2.233 ±0.331
63-74 (2050 μg)	1.702 ±0.062	4.131 ±0.124	0.705 ±0.019	2.273 ±0.115	0.550 ±0.014	0.997 ±0.026	1.961 ±0.052	1.701 ±0.048	3.891 ±0.248	0.551 ±0.110
63-74* (1152.5 μg)	2.458 ±0.090	5.483 ±0.175	0.946 ±0.025	3.142 ±0.125	0.735 ±0.020	1.368 ±0.031	2.620 ±0.060	2.358 ±0.055	4.310 ±0.205	0.861 ±0.203
74-88 (1990 μg)	2.816 ±0.093	6.213 ±0.201	1.126 ±0.030	3.704 ±0.146	0.865 ±0.024	1.544 ±0.035	2.960 ±0.068	2.841 ±0.066	4.981 ±0.238	1.149 ±0.236

* repeat runs

TABLE 8 (CONTINUED 9)

Sample: 79261 (Depth: 7-17 cm)

Size (μm)	He^3 x 10^{-5}	He^4 x 10^{-2}	Ne^{20} x 10^{-3}	Ne^{21} x 10^{-6}	Ne^{22} x 10^{-4}	Ar^{36} x 10^{-4}	Ar^{38} x 10^{-5}	Ar^{40} x 10^{-4}	Kr^{84} x 10^{-8}	Xe^{132} x 10^{-8}
88-105 (2679.5 μg)	2.673 ±0.088	5.983 ±0.180	0.956 ±0.025	3.485 ±0.190	0.761 ±0.020	1.433 ±0.039	2.699 ±0.072	2.546 ±0.069	3.145 ±0.191	0.609 ±0.106
105-250 (2076 μg)	1.781 ±0.063	4.317 ±0.130	0.760 ±0.020	2.456 ±0.137	0.595 ±0.016	1.223 ±0.032	2.338 ±0.062	2.177 ±0.060	4.152 ±0.247	0.804 ±0.136
250-354 (2862.5 μg)	1.689 ±0.068	4.030 ±0.121	0.678 ±0.018	2.295 ±0.091	0.529 ±0.014	1.209 ±0.032	2.255 ±0.060	2.091 ±0.057	3.921 ±0.238	0.786 ±0.099
354-500 (3419.5 μg)	1.383 ±0.076	2.654 ±0.080	0.441 ±0.012	1.947 ±0.089	0.405 ±0.011	0.866 ±0.023	1.639 ±0.043	1.733 ±0.047	2.915 ±0.197	0.603 ±0.083
500-700 (3612.5 μg)	2.552 ±0.076	6.814 ±0.204	0.992 ±0.026	3.002 ±0.204	0.761 ±0.020	1.550 ±0.041	2.927 ±0.077	3.313 ±0.089	4.905 ±0.203	1.051 ±0.081
> 700 (5058 μg)	0.573 ±0.020	1.067 ±0.035	0.159 ±0.004	0.868 ±0.046	0.128 ±0.004	0.237 ±0.005	0.486 ±0.011	0.699 ±0.016	0.744 ±0.041	0.133 ±0.037

TABLE 8 (CONTINUED 10)

Sample: 79261 (Depth: 7-17 cm)

Size (μm)	$\frac{He^4}{He^3}$	$\frac{Ne^{20}}{Ne^{22}}$	$\frac{Ne^{21}}{Ne^{22}}$	$\frac{Ar^{36}}{Ar^{38}}$	$\frac{Ar^{40}}{Ar^{36}}$	$\frac{He^4}{Ne^{20}}$	$\frac{Ne^{20}}{Ar^{36}}$	$\frac{Ar^{36}}{Kr^{84}}$	$\frac{Kr^{84}}{Xe^{132}}$
BULK	2457 ±105	12.69 ±0.49	0.0344 ±0.0017	5.313 ±0.187	1.920 ±0.074	58.10 ±2.35	7.772 ±0.294	3080 ±161	5.59 ±0.93
BULK*	2372 ±106	12.92 ±0.50	0.0341 ±0.0017	5.541 ±0.195	1.593 ±0.061	63.01 ±2.55	7.475 ±0.283	3123 ±163	5.31 ±0.79
< 63	2420 ±108	12.92 ±0.50	0.0349 ±0.0017	5.433 ±0.192	1.637 ±0.063	62.18 ±2.52	7.298 ±0.278	3348 ±248	5.13 ±0.84
63-74	2427 ±115	12.82 ±0.49	0.0413 ±0.0024	5.085 ±0.191	1.706 ±0.066	58.63 ±2.36	7.066 ±0.266	2563 ±177	7.06 ±1.48
63-74*	2231 ±106	12.87 ±0.51	0.0427 ±0.0021	5.222 ±0.168	1.723 ±0.056	57.93 ±2.42	6.917 ±0.243	3174 ±167	5.00 ±1.20
74-88	2206 ±102	13.02 ±0.52	0.0428 ±0.0021	5.216 ±0.169	1.840 ±0.060	55.19 ±2.32	7.291 ±0.257	3100 ±164	4.34 ±0.92

* repeat runs

TABLE 8 (CONTINUED 11)

Sample: 79261 (Depth: 7-17 cm)

Size (μm)	$\frac{He^3}{He^4}$	$\frac{Ne^{20}}{Ne^{22}}$	$\frac{Ne^{21}}{Ne^{22}}$	$\frac{Ar^{36}}{Ar^{38}}$	$\frac{Ar^{40}}{Ar^{36}}$	$\frac{He^4}{Ne^{20}}$	$\frac{Ne^{20}}{Ar^{36}}$	$\frac{Ar^{36}}{Kr^{84}}$	$\frac{Kr^{84}}{Xe^{132}}$
88-105	2238 ± 99	12.56 ±0.48	0.0457 ±0.0028	5.310 ±0.203	1.776 ±0.066	62.60 ±2.51	6.670 ±0.245	4560 ±309	5.16 ±0.95
105-250	2424 ±113	12.78 ±0.49	0.0413 ±0.0026	5.230 ±0.197	1.780 ±0.068	56.78 ±2.29	6.218 ±0.234	2950 ±191	5.16 ±0.93
250-354	2387 ±120	12.82 ±0.49	0.0434 ±0.0021	5.360 ±0.201	1.730 ±0.066	59.48 ±2.39	5.605 ±0.210	3087 ±204	4.99 ±0.70
354-500	1920 ±120	10.89 ±0.42	0.0481 ±0.0025	5.287 ±0.198	2.000 ±0.076	60.23 ±2.42	5.086 ±0.191	2966 ±215	4.83 ±0.74
500-700	2671 ±113	13.03 ±0.50	0.0394 ±0.0017	5.297 ±0.198	2.137 ±0.080	68.66 ±2.75	6.400 ±0.239	3163 ±155	4.67 ±0.41
> 700	1860 ± 89	12.47 ±0.51	0.0678 ±0.0041	4.890 ±0.156	2.942 ±0.095	66.91 ±2.85	6.715 ±0.234	3391 ±200	5.57 ±1.58

TABLE 9

VARIATION OF CHEMICAL AND PETROLOGICAL PARAMETERS WITH DEPTH IN APOLLO 17 TRENCH AT STATION 9

(Based on fines 79221, 79241, and 79261)

	79221 (0-2cm)	79241 (2-7cm)	79261 (7-17cm)	Reference
Agglutinates (%) (90-150μm)	44.4	--	22.3	Heiken & McKay, 1974
Median Grain Size (μm)	46.7	--	57.9	McKay et al., 1974
Graphic Mean (Φ)*	4.20	4.13	4.00	Butler et al., 1974
FeO + TiO_2 (%)	21.91	22.43	20.97	Rose et al., 1974
Pb^{207}/Pb^{206}	0.8177	0.7766	0.7430	Nunes & Tatsumoto 1974
U^{238}/Pb^{204}	78.4	95.9	101	Nunes & Tatsumoto 1974
C (μg/g)	150	140	110.0	Moore et al., 1974
Al_2O_3 (%)	13.48	13.90	14.51	Moore et al., 1974
MgO (%)	10.30	9.90	9.67	Moore et al., 1974

*for diameter in μm, $D(\mu m) = (\frac{1}{2})^{-\Phi} \times 10^3$

FIGURE CAPTIONS

Figure 1. Schematic diagram of mass spectrometer and sample preparation system.

Figure 2. Planimetric map of Apollo 15 landing site.

Figure 3. Inert gas contents versus grain diameter for two Apollo 15 samples: 15421 and 15071. Values of n for 15071 are from best fit of data to the equation $C(cm^3\ STP/g) = KD^{-n}$ (μm).

Figure 4. Ne^{22}/Ne^{21} versus $1/Ne^{21}$. Illustration of the theory of the Eberhardt plot.

Figure 5. Eberhardt plot for 15071. Data from Jordan *et al.* (1974).

Figure 6. Eberhardt plot for 15091. Data from Heymann *et al.* (1972).

Figure 7. Eberhardt plot for 15601.

Figure 8. Ar^{40} versus Ar^{36} for 15071 line defined by equation $Ar^{40} = 0.792\ Ar^{36} + 0.140 \times 10^{-4} cm^3$ STP/g.

Figure 9. Ar^{40} versus Ar^{36} for 15421. Line fitted to all grain size fractions:
$Ar^{40} = 3.31\ Ar^{36} + 0.301 \times 10^{-4}\ cm^3$ STP/g.

Line fitted to four smallest grain size fractions:
$Ar^{40} = 2.97\ Ar^{36} + 0.388 \times 10^{-4}\ cm^3$ STP/g.

Line fitted to four largest grain size fractions:

$Ar^{40} = 3.94\ Ar^{36} + 0.082 \times 10^{-4}\ cm^3\ STP/g.$

Figure 10. Ar^{40} versus Ar^{36} for 15511. Lines are approximate best fits through extreme points. The slope of the upper limit is ~ 3.0 and the slope of the lower limit is ~ 0.9. No attempt was made to determine intercept values.

Figure 11. Ar^{40} versus Ar^{36} for 15501. Line defined by: $Ar^{40} = 0.723\ Ar^{36} + 0.246 \times 10^{-4}\ cm^3\ STP/g.$

Figure 12. Planimetric map of Apollo 17 landing site and an enlargement of Van Serg Crater.

Figure 13. Hypothetical grain size distribution curve where $N(D) = kD^{-\alpha}$. Both coarse and "mature" soil distributions are shown.

Figure 14. Ar^{36} versus effective diameter (D_{eff}) for Apollo 17 trench fines collected at Station 9 near Van Serg Crater.

Figure 15. Hypothetical gas contents versus effective diameter diagram for two soils with perfect anti-correlations defined by curves A and B. Curve C shows the result of mixing the two soils in equal proportions with no sorting in the process.

Curves D and E show two of many possible mixing curves resulting from mixing predominately coarse material of soil A with soil B.

Figure 16. Eberhardt plot of Apollo 17 trench fines 79221. Ages were calculated from Ne^{21}_C contents determined from the slope of the lines through the extreme points and the assumed intercept $(Ne^{22}/Ne^{21})_T = 32.0$.

Figure 17. Eberhardt plot of Apollo 17 trench fines 79241. Solid lines and associated ages were determined in the same manner as with 79221. Dashed lines illustrate lines and associated ages which would result if an assumed intercept of $(Ne^{22}/Ne^{21})_T = 31.0$ had been used.

Figure 18. Eberhardt plot of Apollo 17 trench fines 79261. Solid and dashed lines determined in the same manner as 79221 and 79241.

Figure 19. Ar^{40} versus Ar^{36} for Apollo 17 trench fines 79221, 79241, and 79261. Slope and intercept of lower limit was determined from approximate best fit through extreme points, the slope is $\sim$ 1.30 and the intercept is $\sim 0.37 \times 10^{-4}$ cm^3 STP/g. The slope of the upper limit is $\sim$ 2.50 and was determined from one extreme point and

an intercept calculated from the relation $Ar^{40}_{intercept} = 4 \times 10^{-8}$ K cm^3 STP (K = potassium content in ppm) from Yaniv and Heymann (1972). The assumed K content was 1450 ppm and the intercept is 0.58×10^{-4} cm^3 STP/g.

FIGURE 1

MASS SPECTROMETER

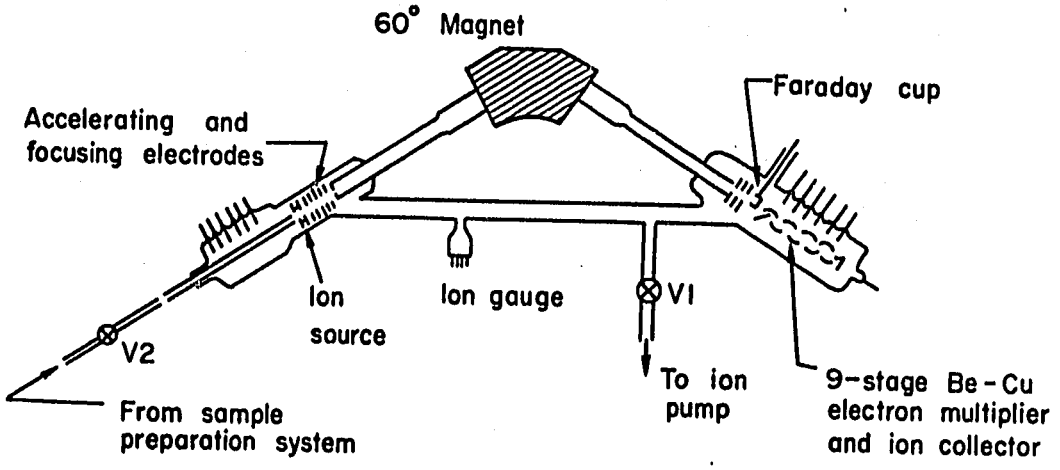

SAMPLE PREPARATION LINE

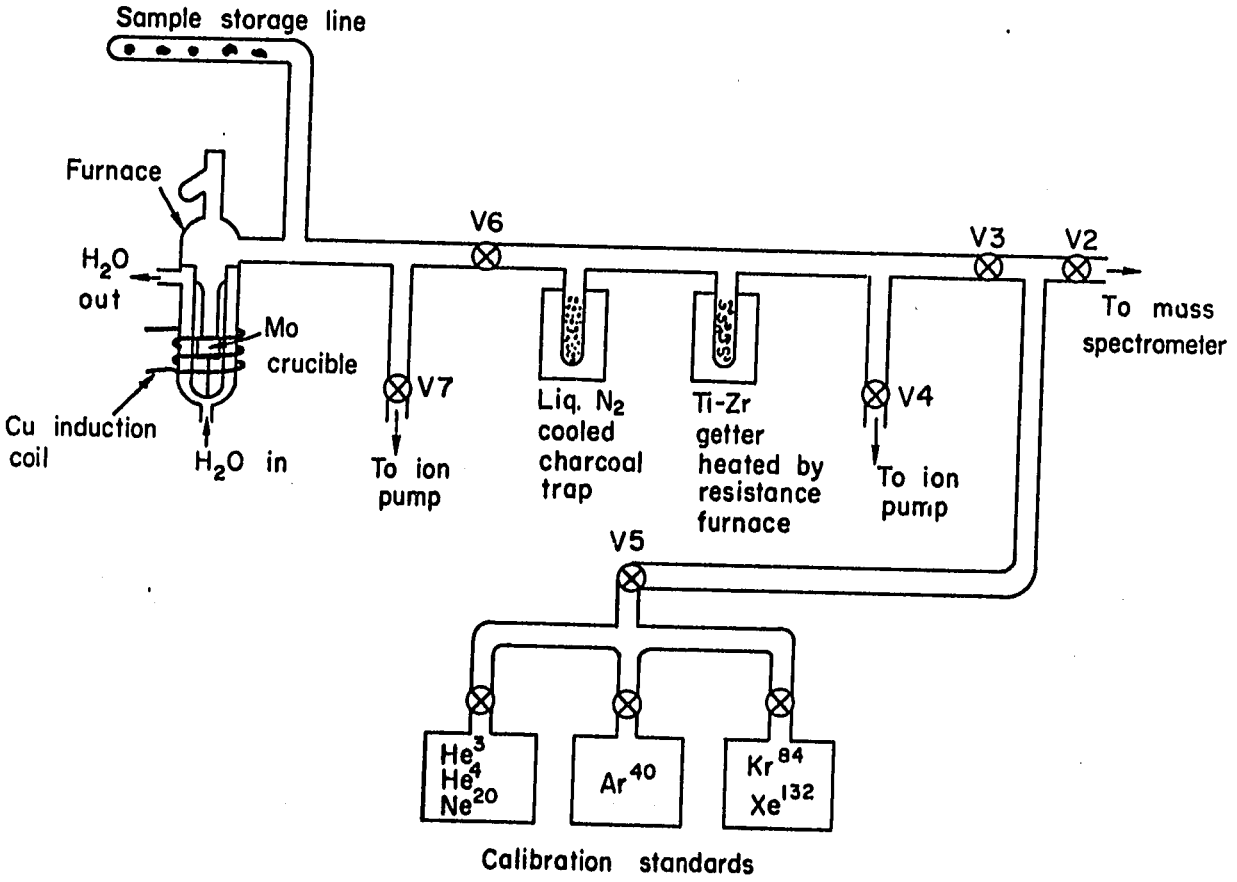

FIGURE 2

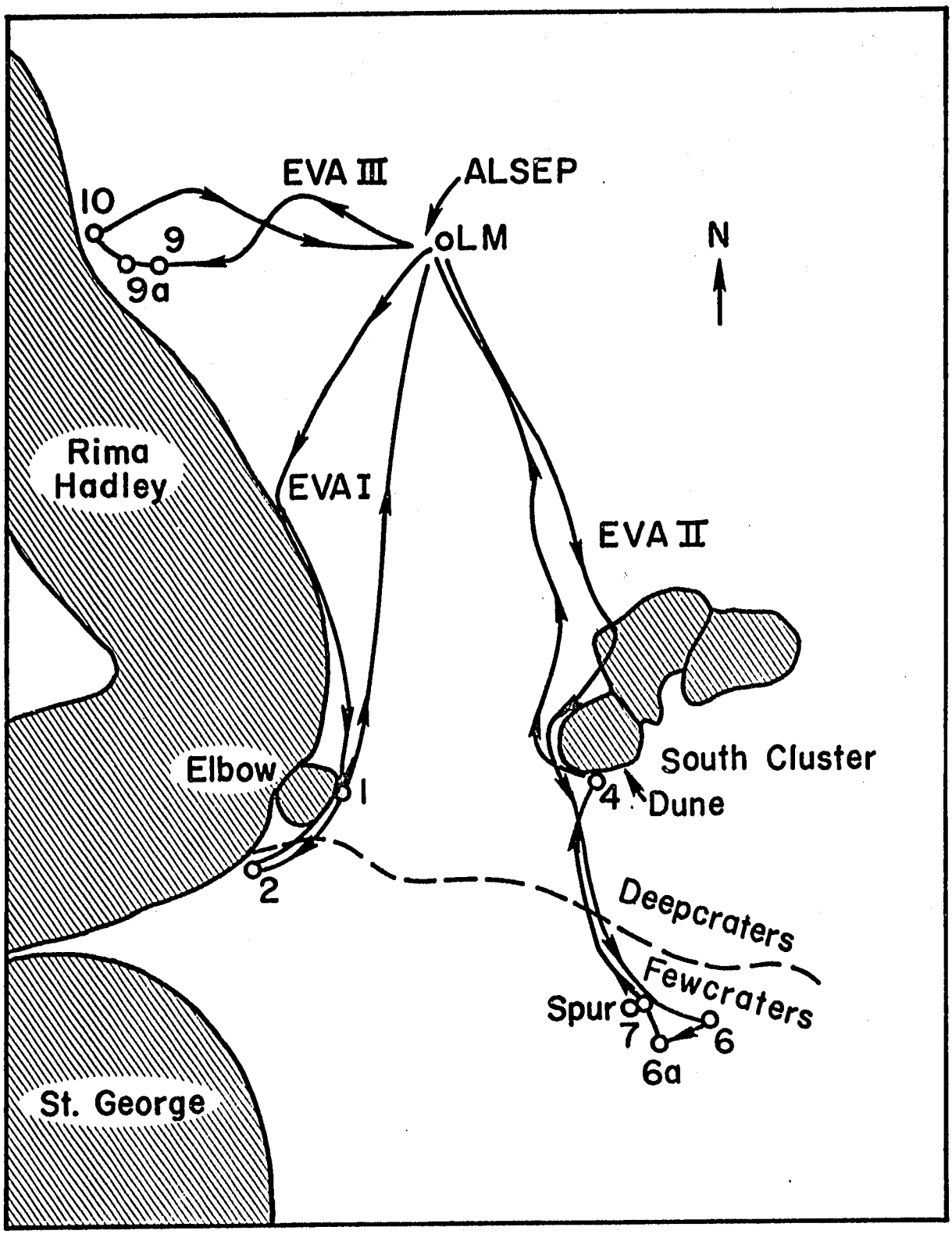

APOLLO 15 LANDING SITE

FIGURE 3

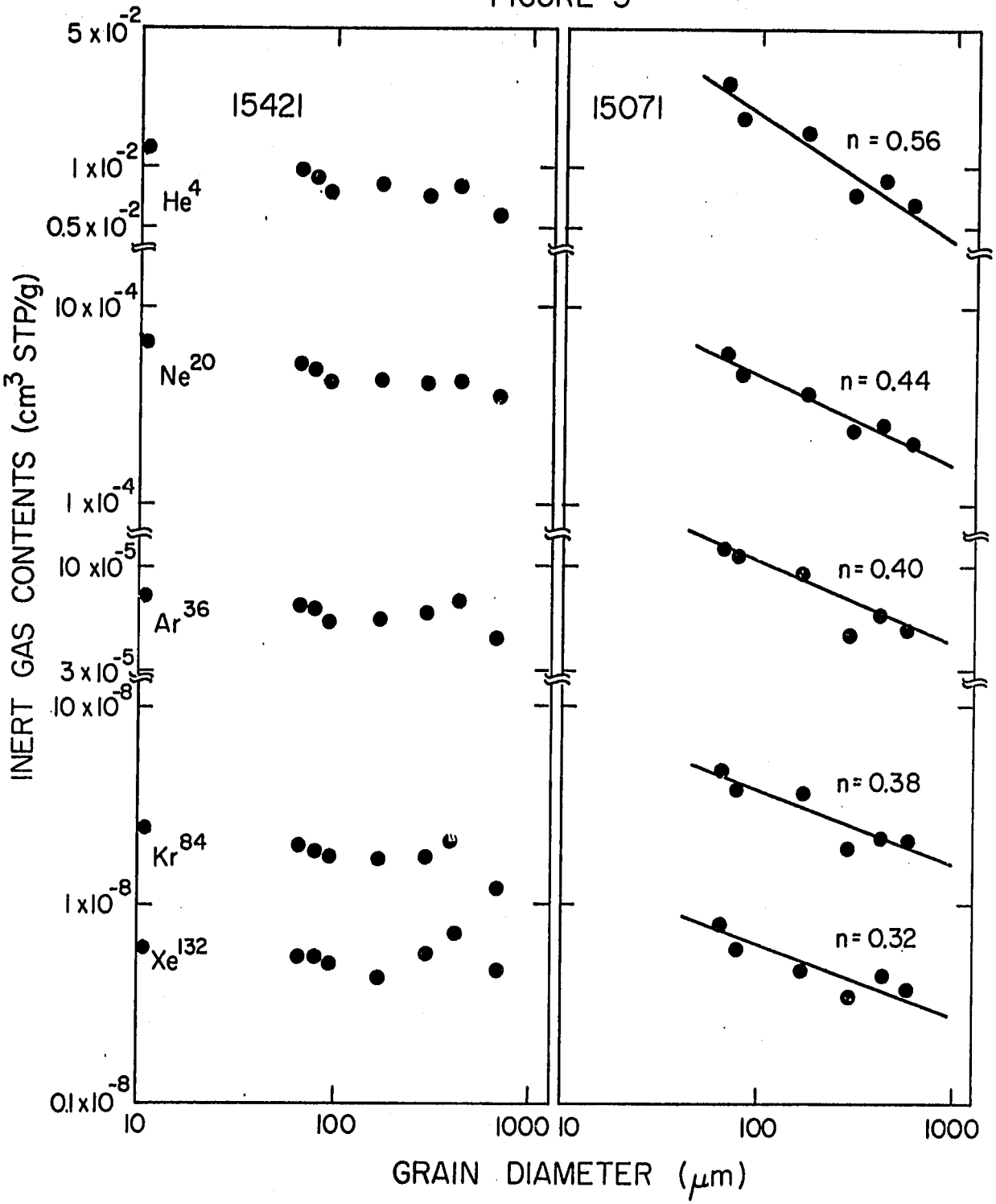
15421
15071
5 x 10^-2
1 x 10^-2
0.5 x 10^-2
10 x 10^-4
1 x 10^-4
10 x 10^-5
3 x 10^-5
10 x 10^-8
1 x 10^-8
0.1 x 10^-8
He^4
Ne^20
Ar^36
Kr^84
Xe^132
n = 0.56
n = 0.44
n = 0.40
n = 0.38
n = 0.32
INERT GAS CONTENTS (cm^3 STP/g)
10
100
1000
GRAIN DIAMETER (μm)

FIGURE 4

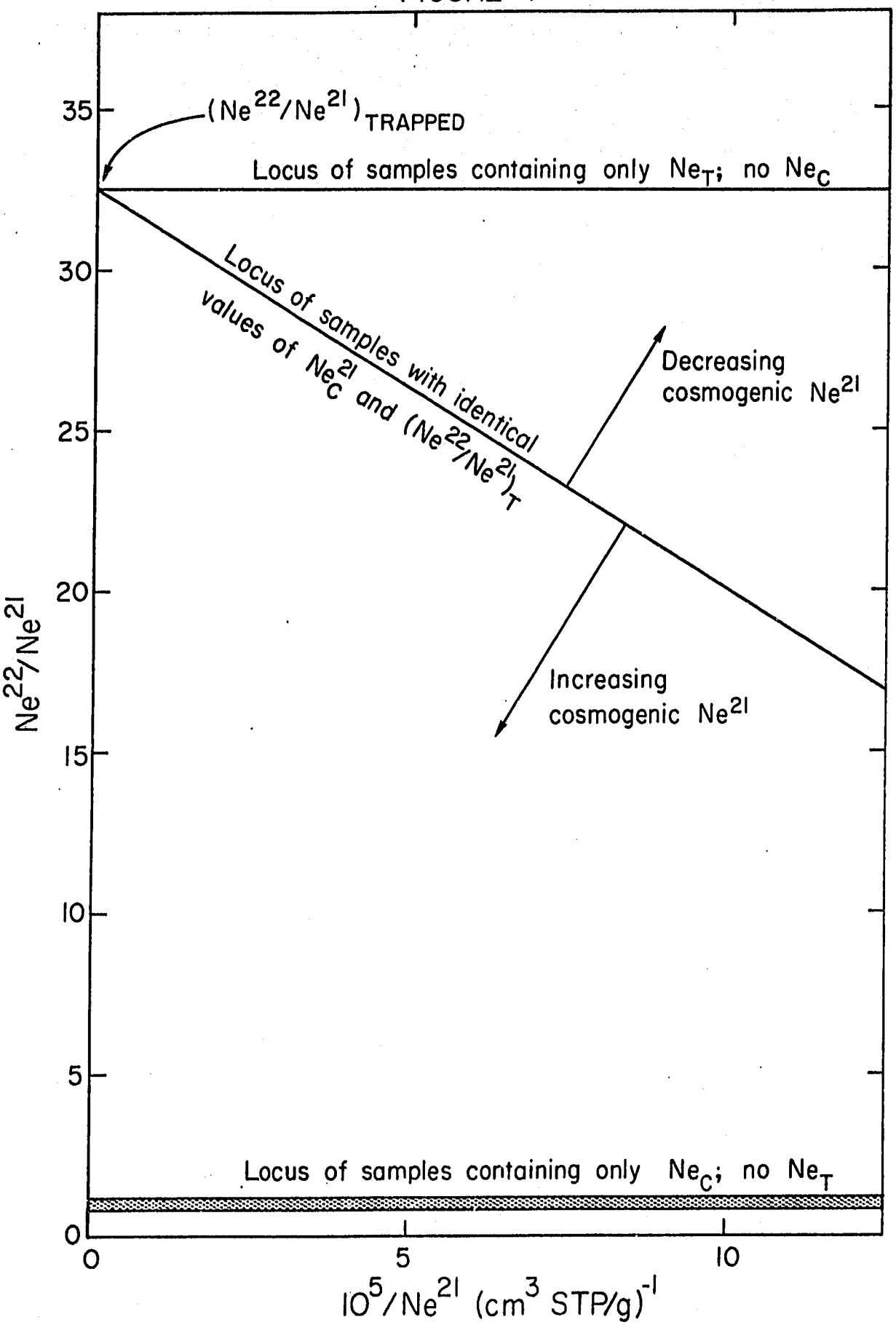
35
30
25
20
15
10
5
0
0
5
10
$(Ne^{22}/Ne^{21})_{TRAPPED}$
Locus of samples containing only Ne_T; no Ne_C
Locus of samples with identical values of Ne_C^{21} and $(Ne^{22}/Ne^{21})_T$
Decreasing cosmogenic Ne^{21}
Increasing cosmogenic Ne^{21}
Locus of samples containing only Ne_C; no Ne_T
Ne^{22}/Ne^{21}
$10^5/Ne^{21}$ $(cm^3$ STP/g$)^{-1}$

FIGURE 5

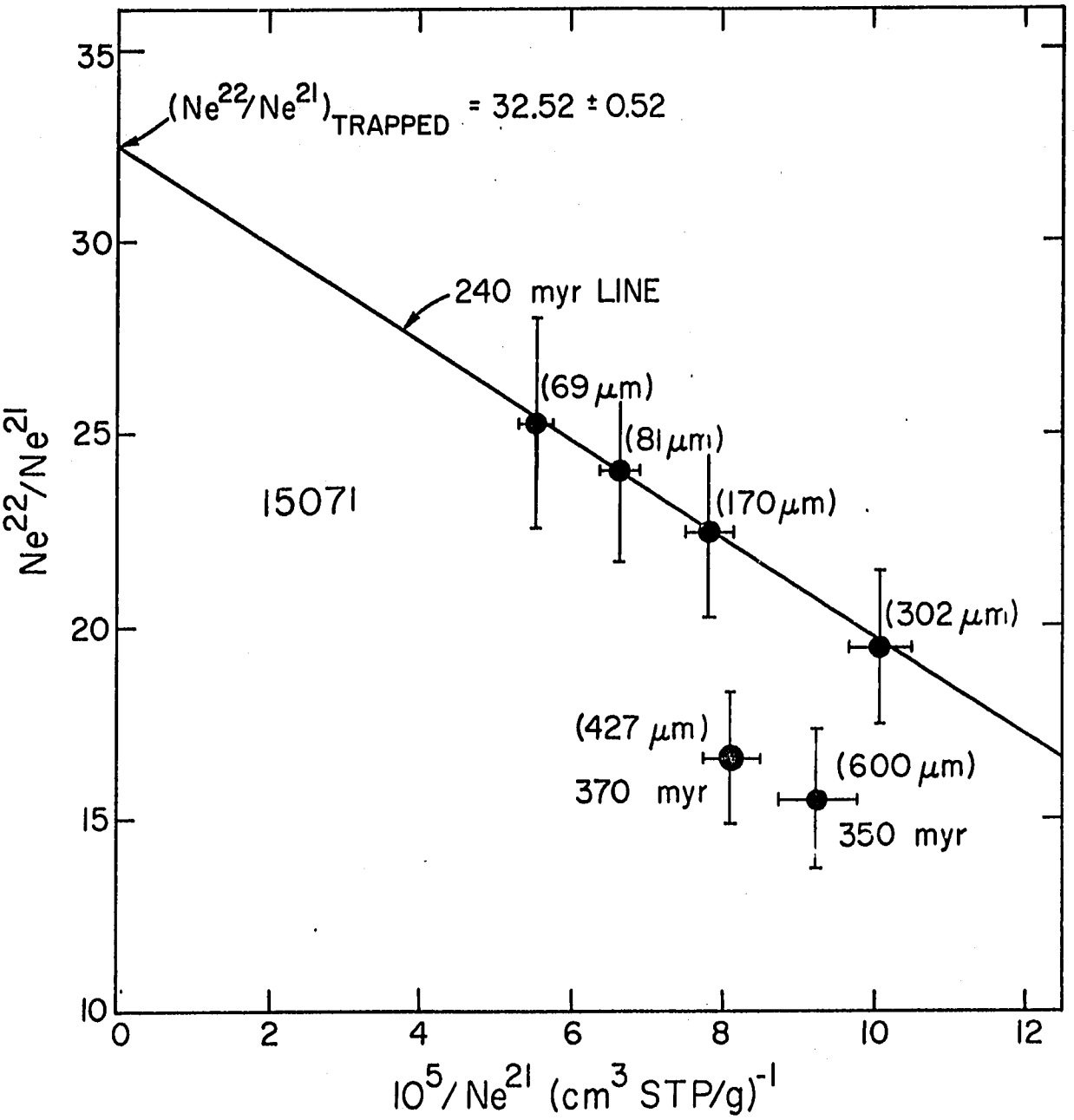
35
30
25
20
15
10
0
2
4
6
8
10
12
$(Ne^{22}/Ne^{21})_{TRAPPED}$ = 32.52 ± 0.52
240 myr LINE
(69 μm)
(81 μm)
(170 μm)
(302 μm)
(427 μm)
370 myr
(600 μm)
350 myr
15071
Ne^{22}/Ne^{21}
$10^5/Ne^{21}$ $(cm^3$ STP/g$)^{-1}$

FIGURE 6

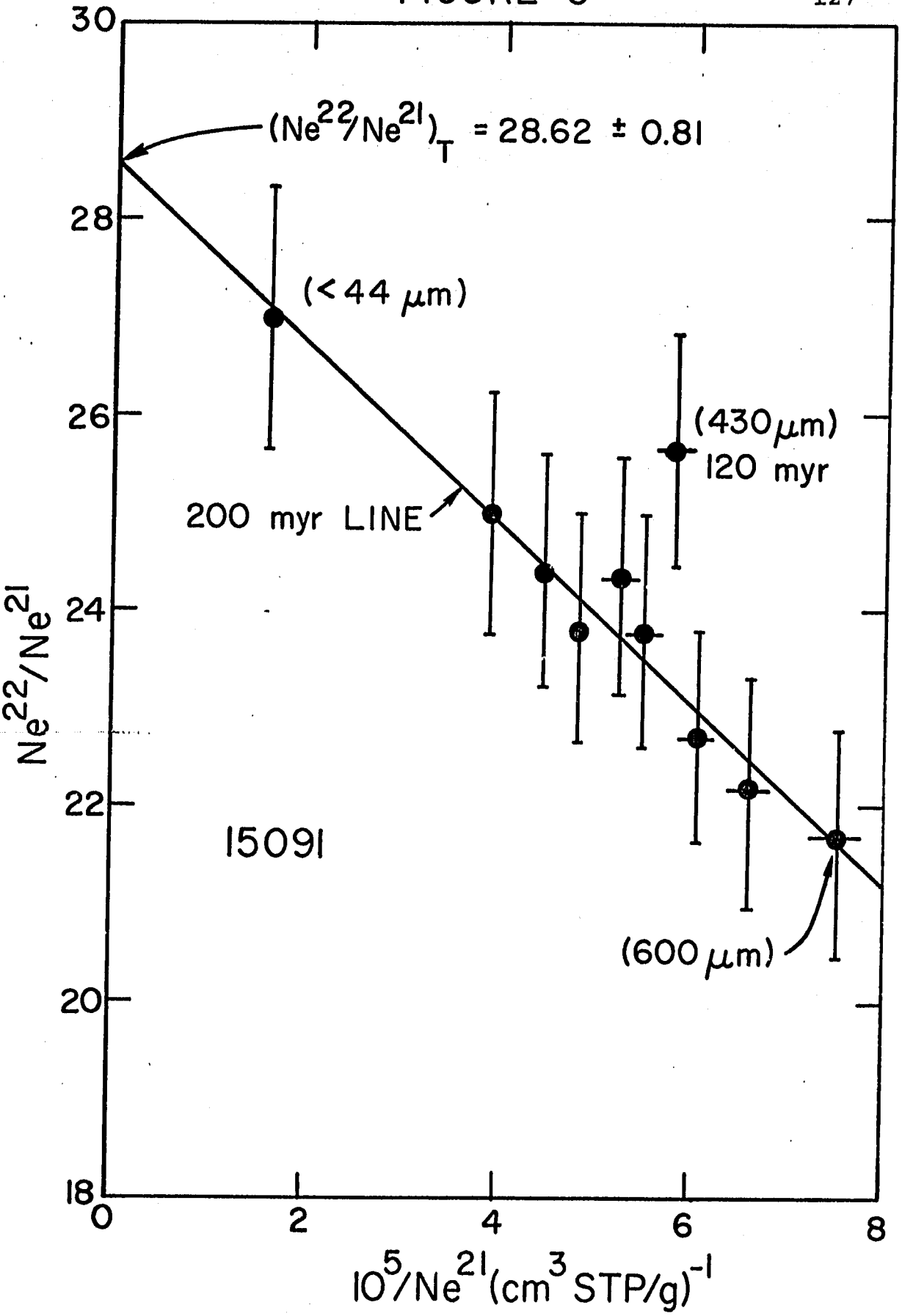
30
28
26
24
22
20
18
0
2
4
6
8
$(Ne^{22}/Ne^{21})_T = 28.62 \pm 0.81$
(< 44 μm)
(430 μm)
120 myr
200 myr LINE
15091
(600 μm)
Ne^{22}/Ne^{21}
$10^5/Ne^{21}(cm^3\ STP/g)^{-1}$

FIGURE 7

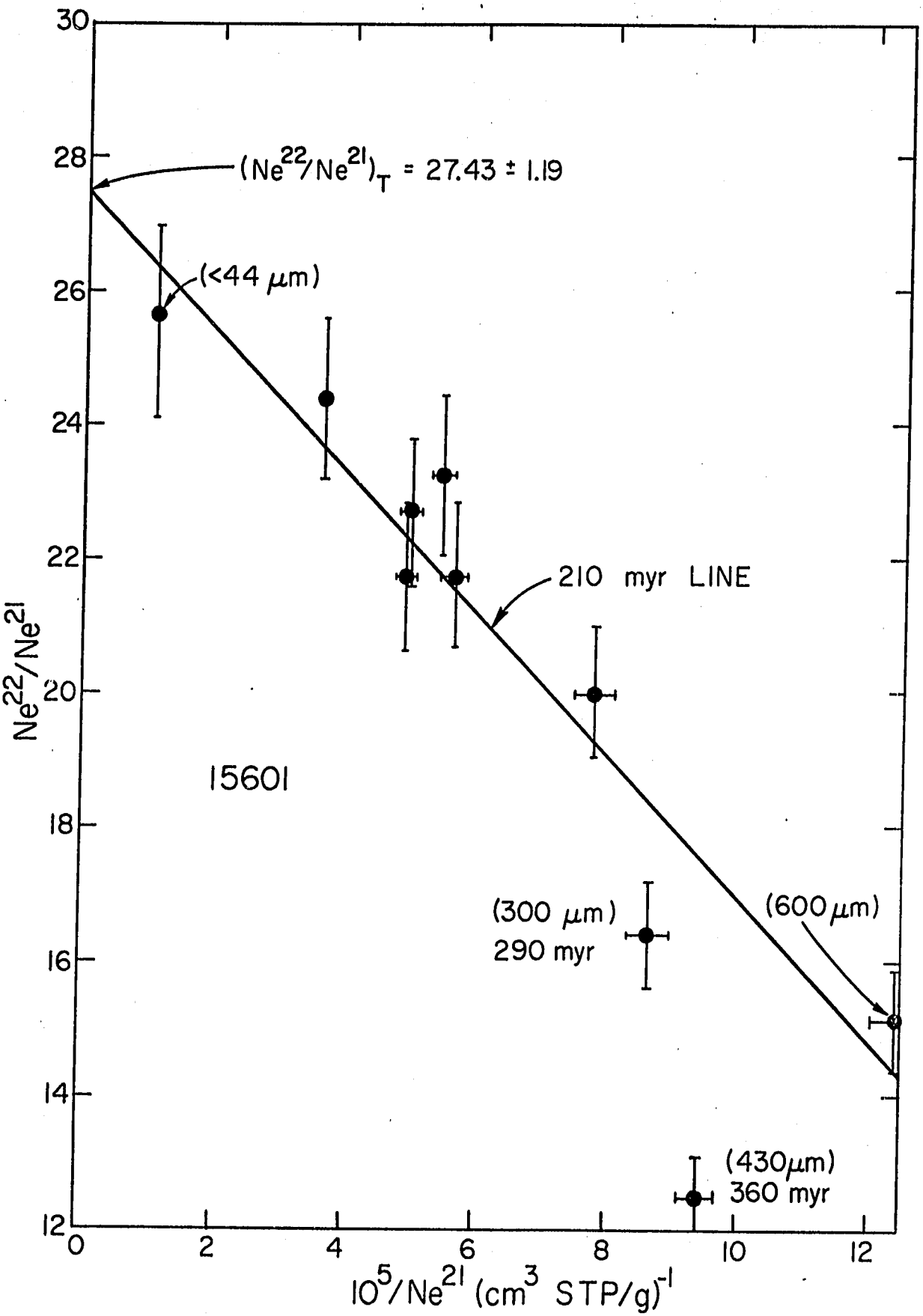
30
28
26
24
22
20
18
16
14
12
0
2
4
6
8
10
12
Ne^{22}/Ne^{21}
$10^5/Ne^{21}$ (cm^3 STP/g)$^{-1}$
$(Ne^{22}/Ne^{21})_T$ = 27.43 ± 1.19
(<44 μm)
210 myr LINE
15601
(300 μm)
290 myr
(600 μm)
(430μm)
360 myr

FIGURE 8

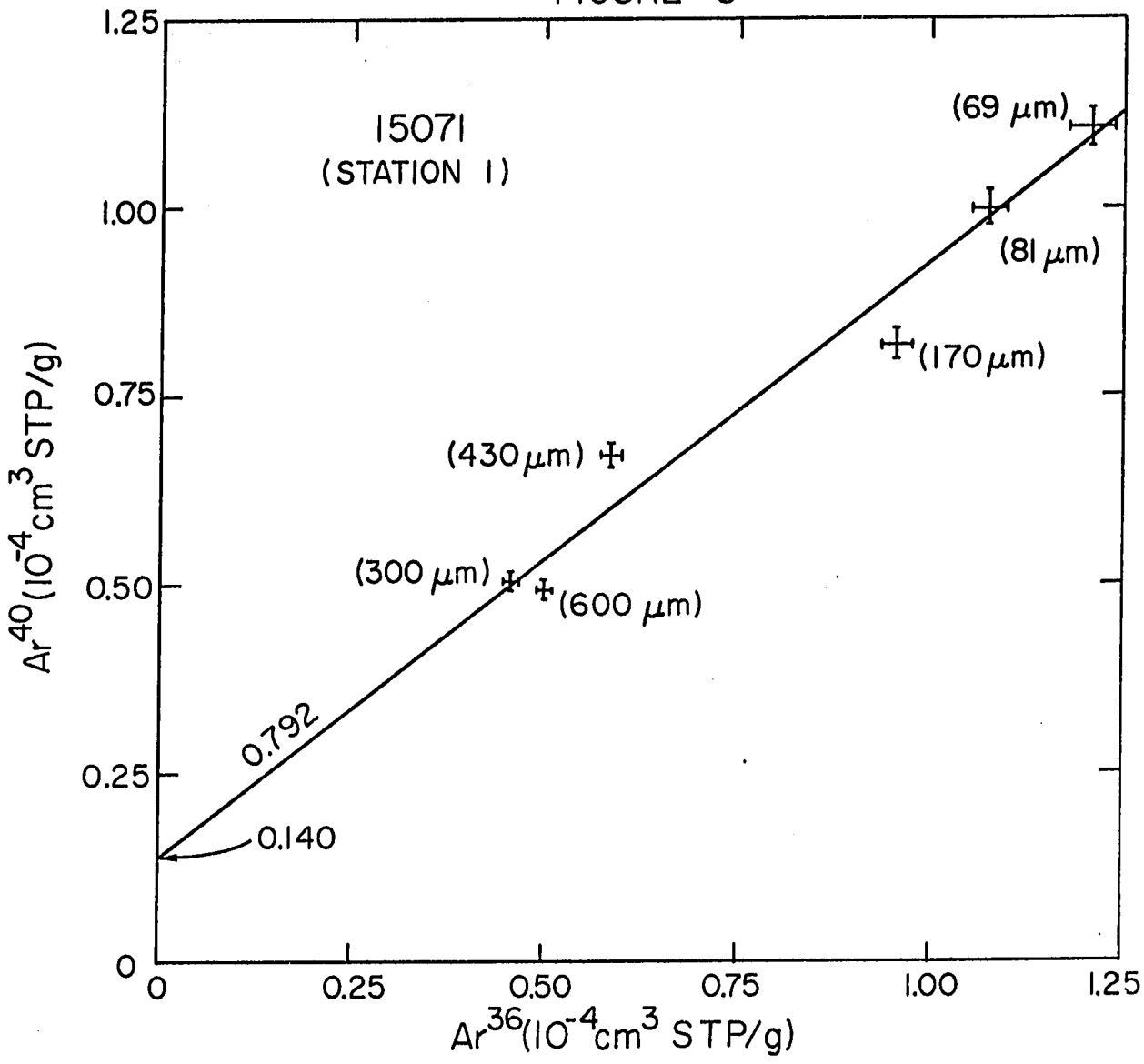
15071
(STATION 1)
(69 μm)
(81 μm)
(170 μm)
(430 μm)
(300 μm)
(600 μm)
0.792
0.140
1.25
1.00
0.75
0.50
0.25
0
0
0.25
0.50
0.75
1.00
1.25
Ar40(10-4cm3 STP/g)
Ar36(10-4cm3 STP/g)

FIGURE 9

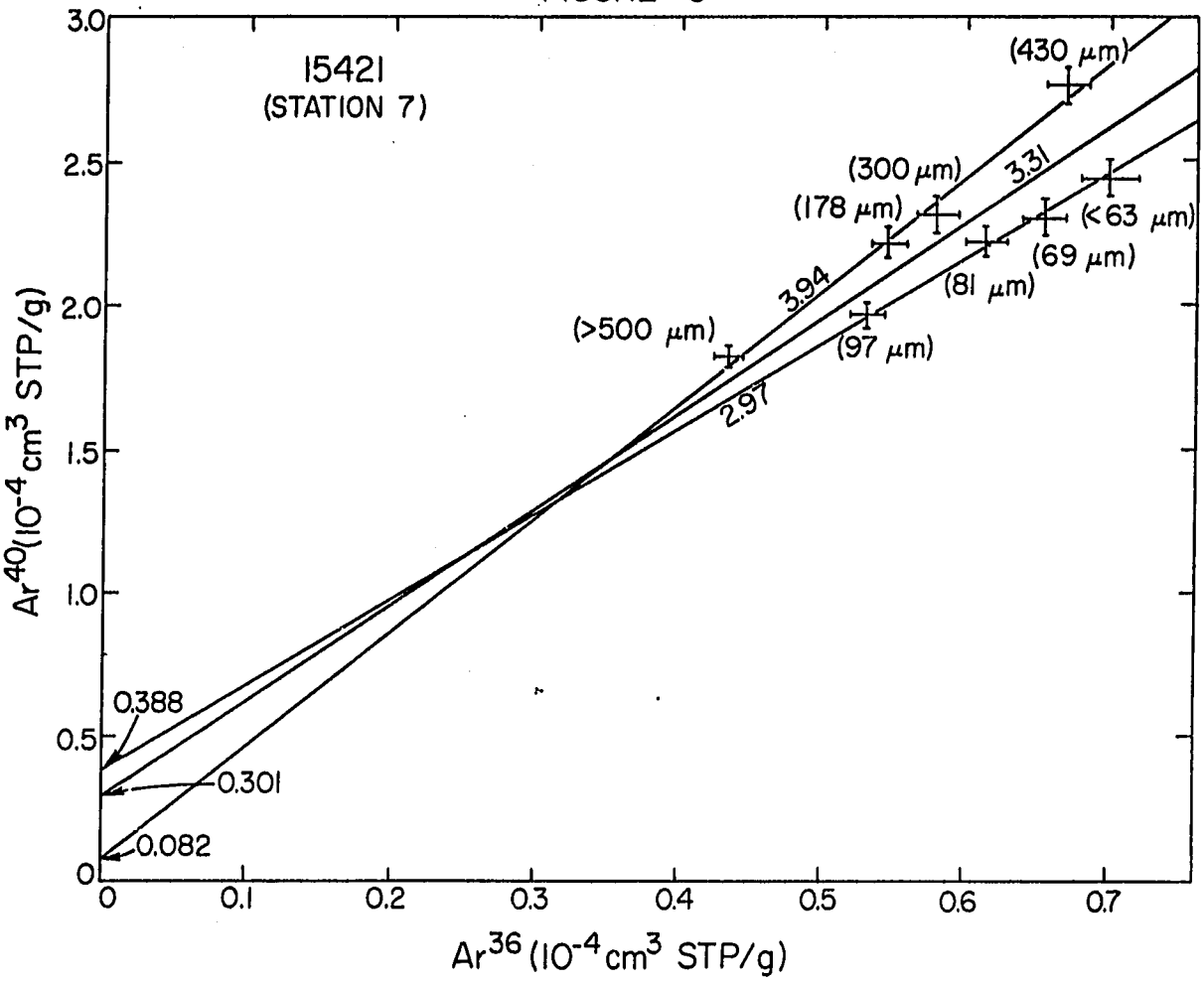
15421
(STATION 7)
(430 μm)
(300 μm)
(178 μm)
(<63 μm)
(69 μm)
(81 μm)
(97 μm)
(>500 μm)
3.31
3.94
2.97
0.388
0.301
0.082
3.0
2.5
2.0
1.5
1.0
0.5
0
0.1
0.2
0.3
0.4
0.5
0.6
0.7
Ar40(10-4 cm3 STP/g)
Ar36 (10-4 cm3 STP/g)

FIGURE 10

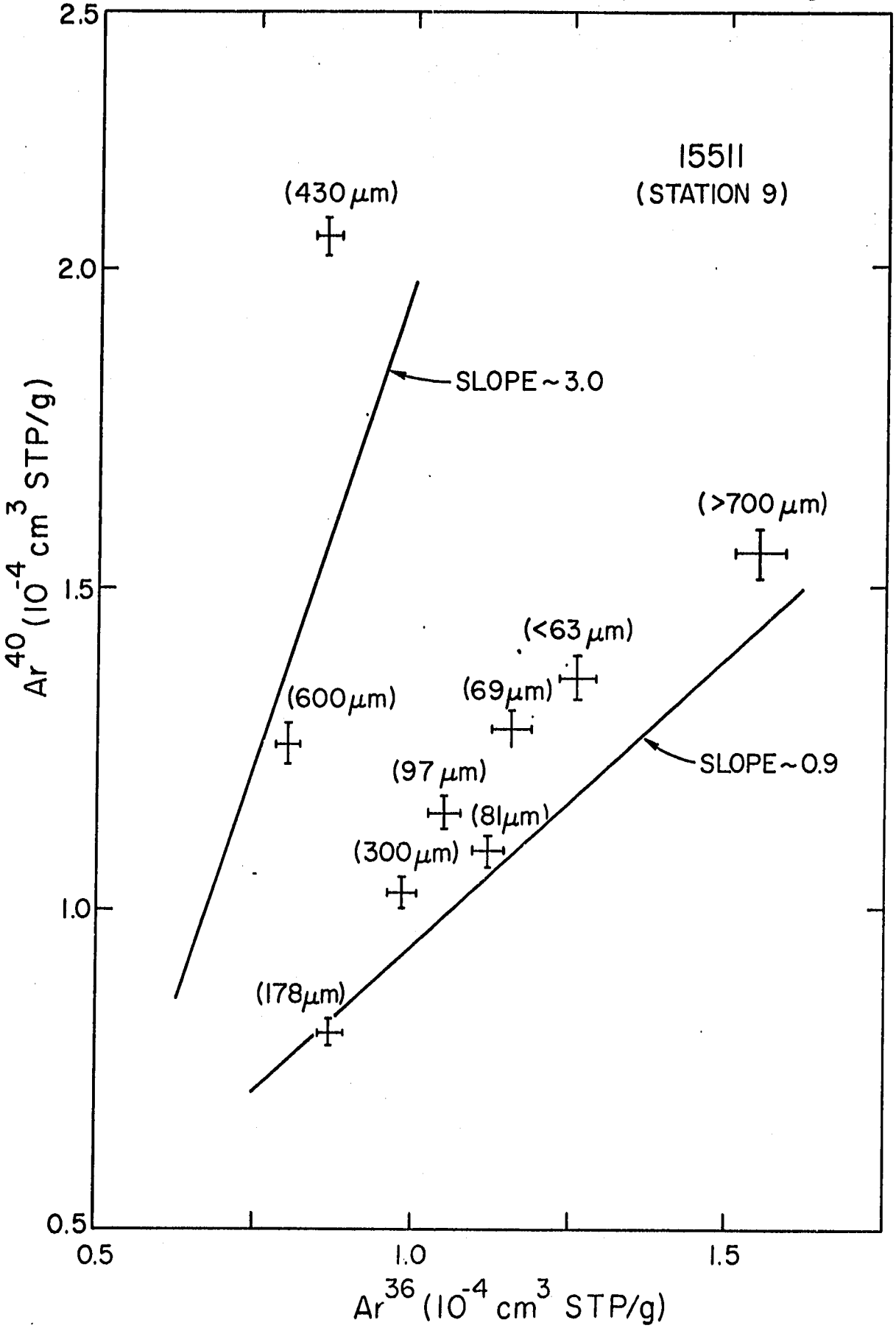
15511
(STATION 9)
(430 μm)
SLOPE ~ 3.0
(>700 μm)
(<63 μm)
(69 μm)
(600 μm)
SLOPE ~ 0.9
(97 μm)
(81 μm)
(300 μm)
(178 μm)
2.5
2.0
1.5
1.0
0.5
0.5
1.0
1.5
Ar40 (10-4 cm3 STP/g)
Ar36 (10-4 cm3 STP/g)

FIGURE 11

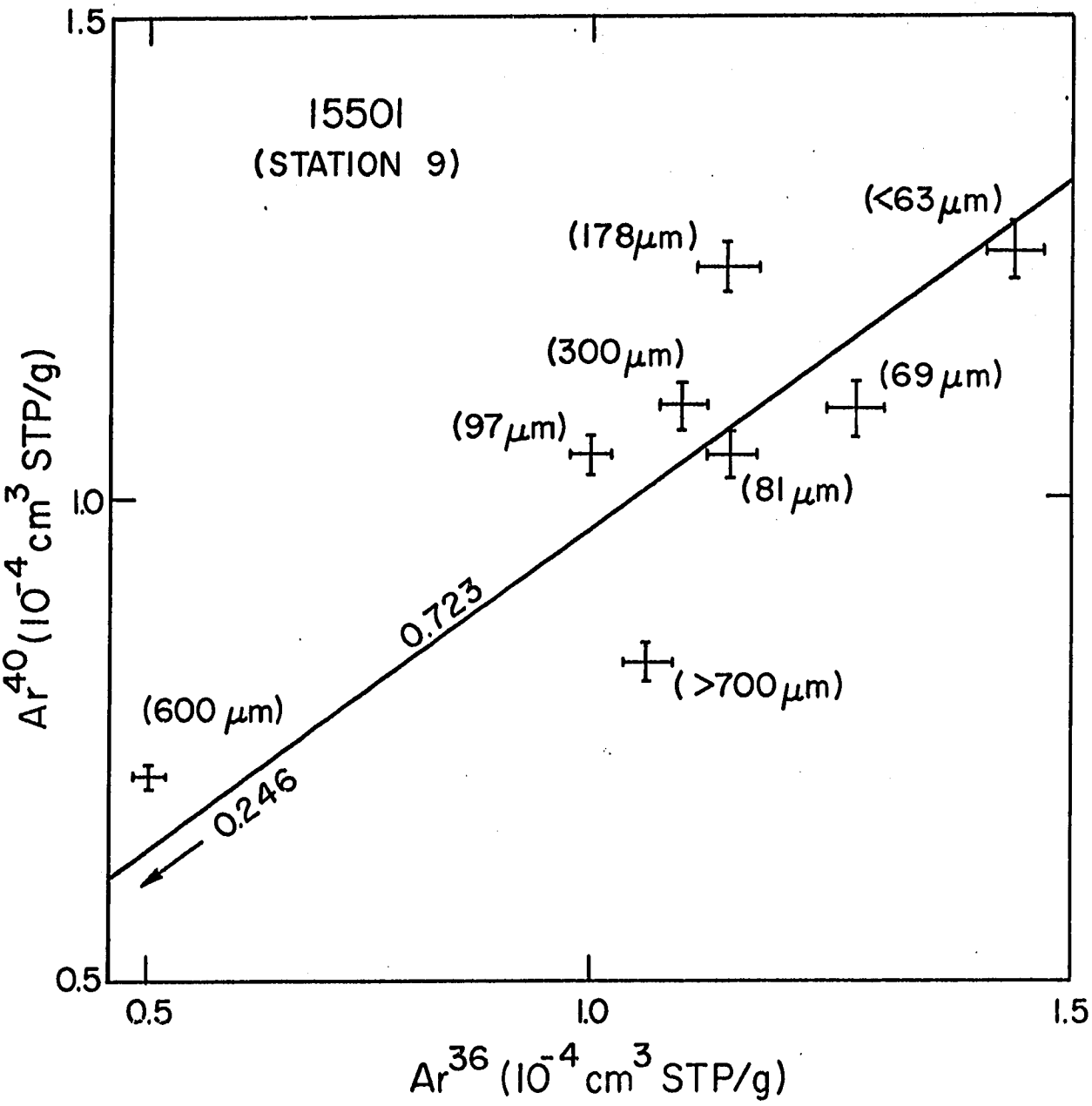
15501
(STATION 9)
(<63 μm)
(178 μm)
(300 μm)
(69 μm)
(97 μm)
(81 μm)
(600 μm)
(>700 μm)
0.723
0.246
1.5
1.0
0.5
0.5
1.0
1.5
Ar40 (10-4 cm3 STP/g)
Ar36 (10-4 cm3 STP/g)

FIGURE 12

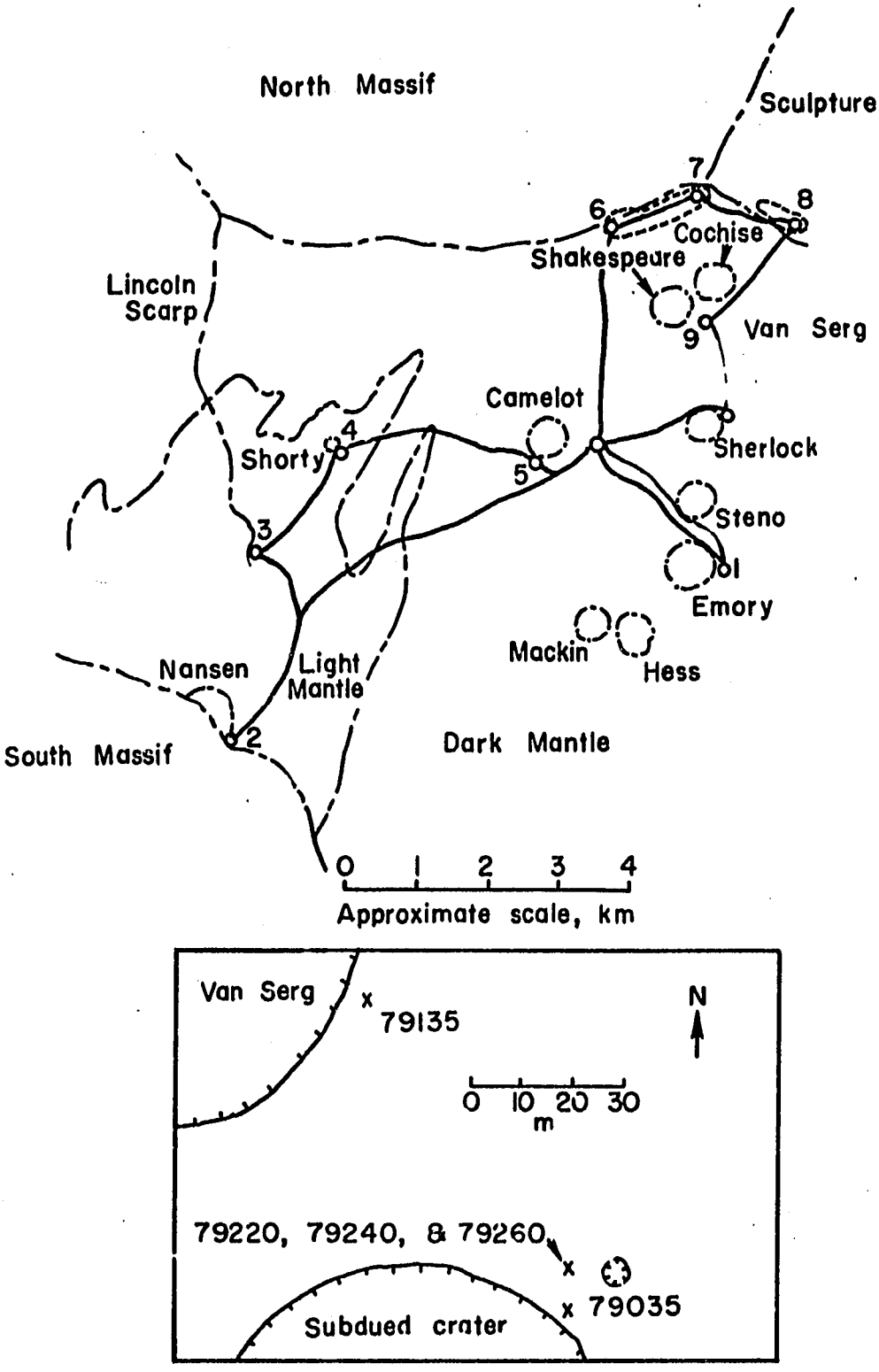

APOLLO 17 LANDING SITE AND VAN SERG CRATER

FIGURE 13

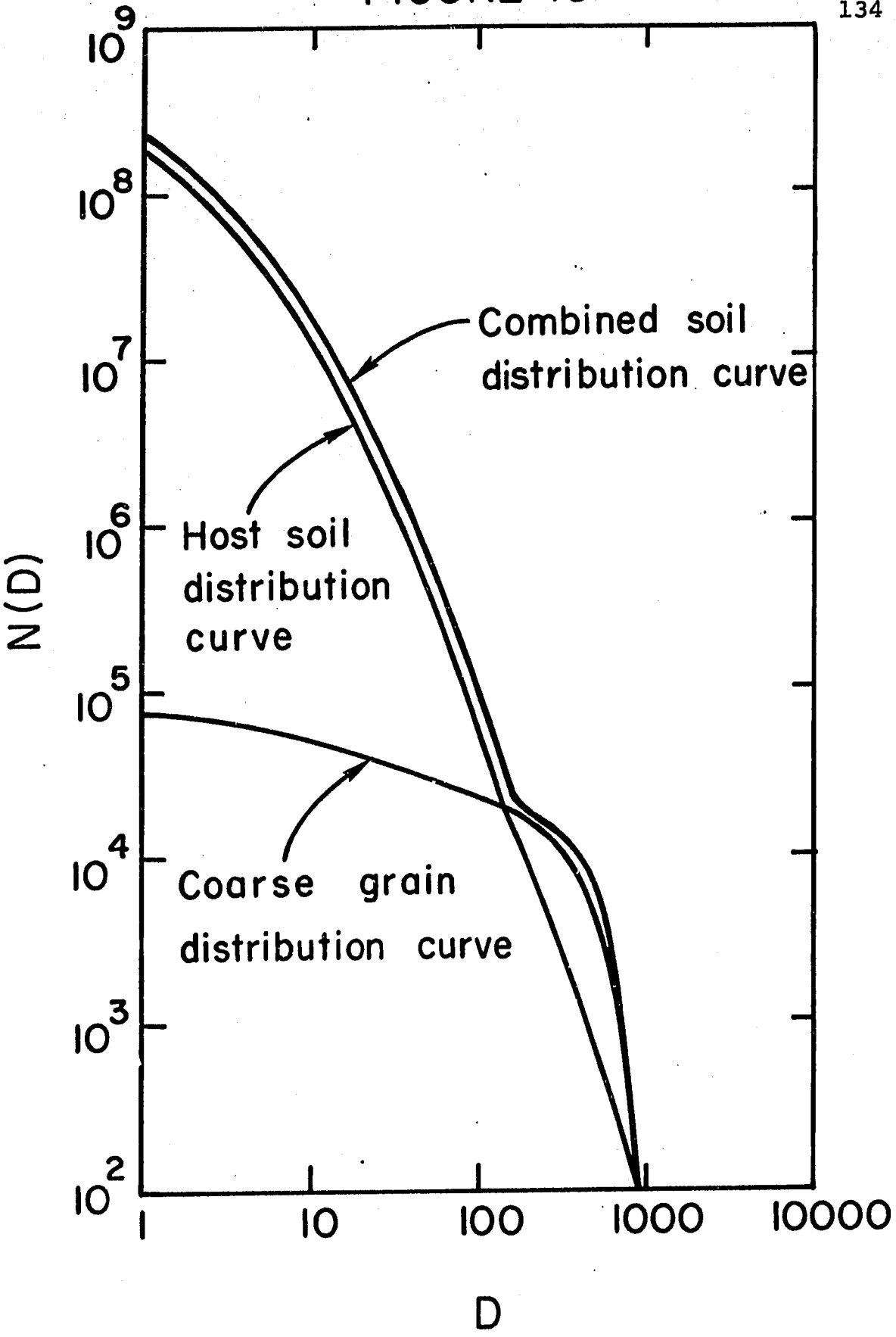
10^9
10^8
10^7
10^6
10^5
10^4
10^3
10^2
N(D)
Combined soil distribution curve
Host soil distribution curve
Coarse grain distribution curve
1
10
100
1000
10000
D

FIGURE 14

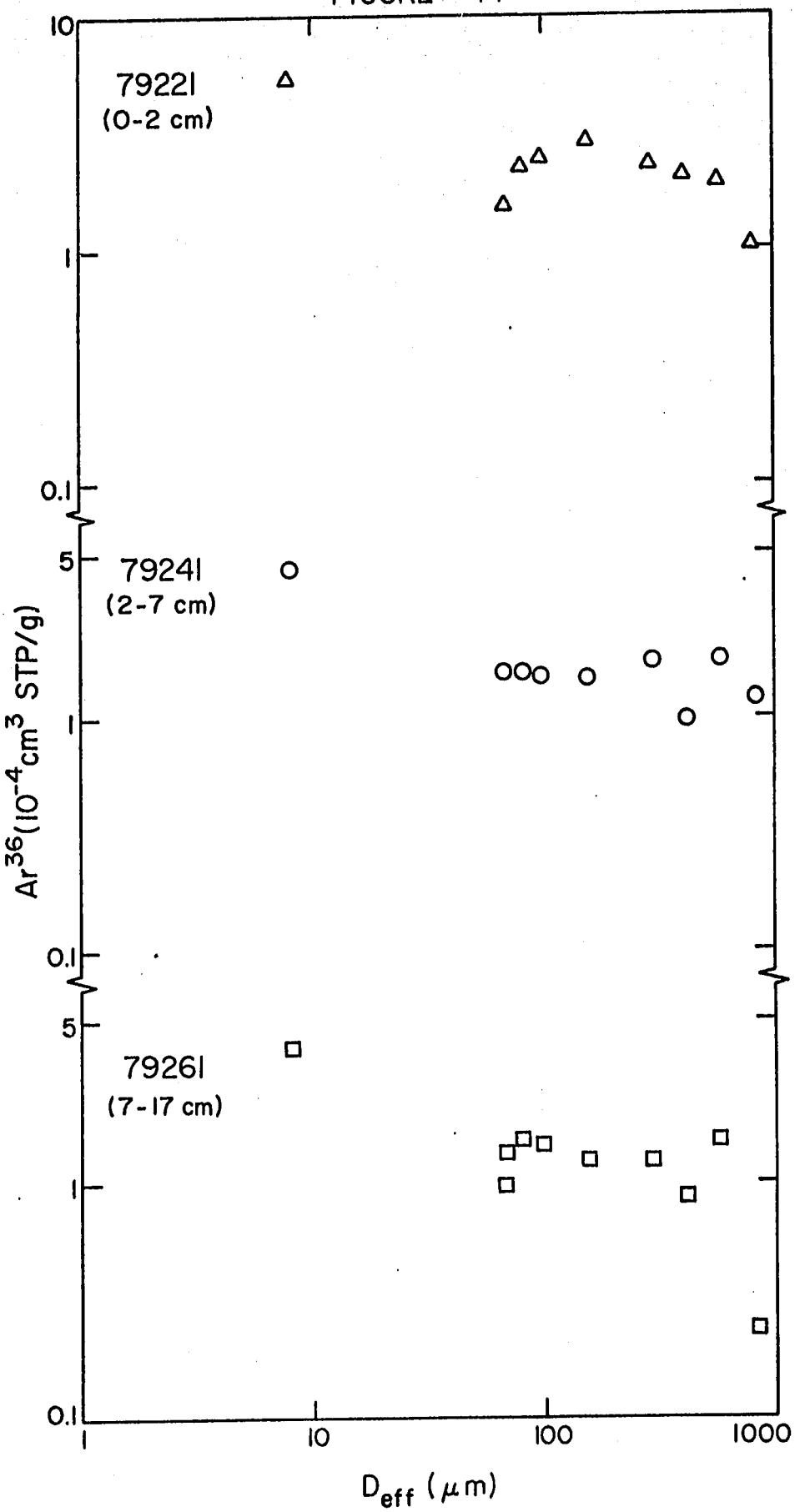
79221
(0-2 cm)
79241
(2-7 cm)
79261
(7-17 cm)
10
1
0.1
5
1
0.1
5
1
0.1
1
10
100
1000
$Ar^{36}(10^{-4}cm^3$ STP/g)
D_{eff} (μm)

FIGURE 15

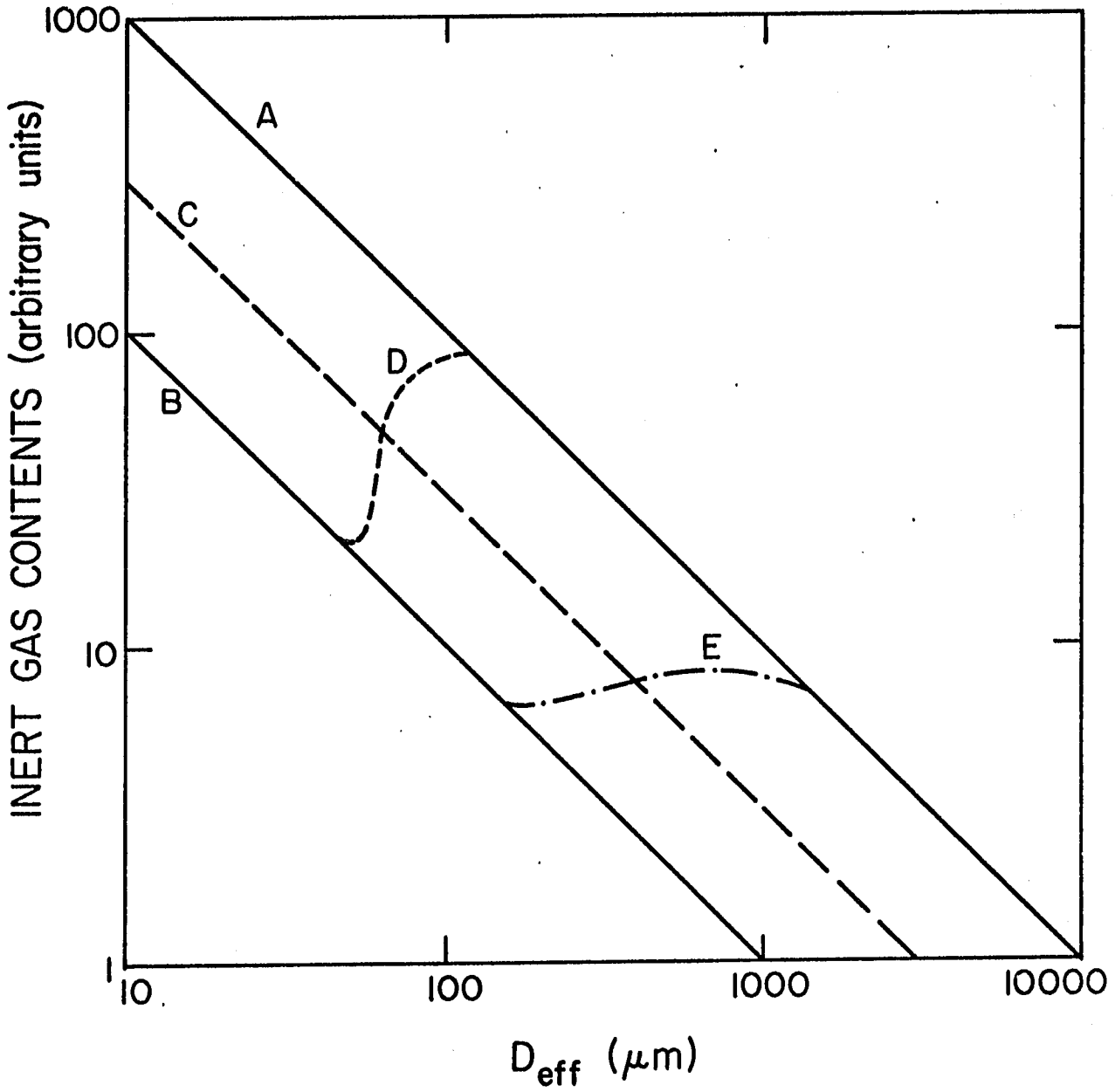
1000
100
10
1
INERT GAS CONTENTS (arbitrary units)
A
B
C
D
E
10
100
1000
10000
D_{eff} (μm)

FIGURE 16

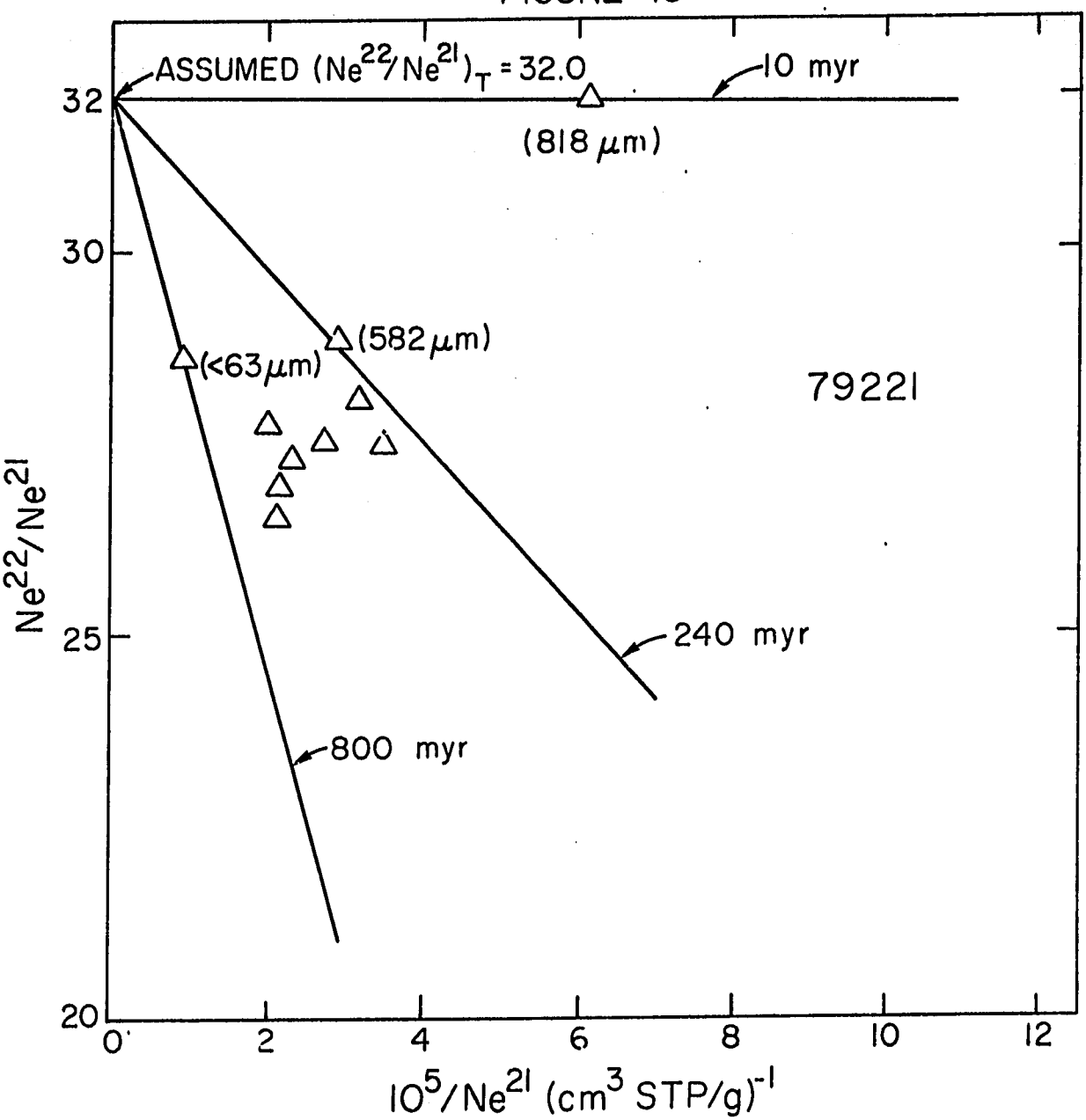
ASSUMED $(Ne^{22}/Ne^{21})_T = 32.0$
10 myr
(818 μm)
(582 μm)
(<63 μm)
79221
240 myr
800 myr
Ne^{22}/Ne^{21}
$10^5/Ne^{21}$ $(cm^3$ STP/g$)^{-1}$
32
30
25
20
0
2
4
6
8
10
12

FIGURE 17

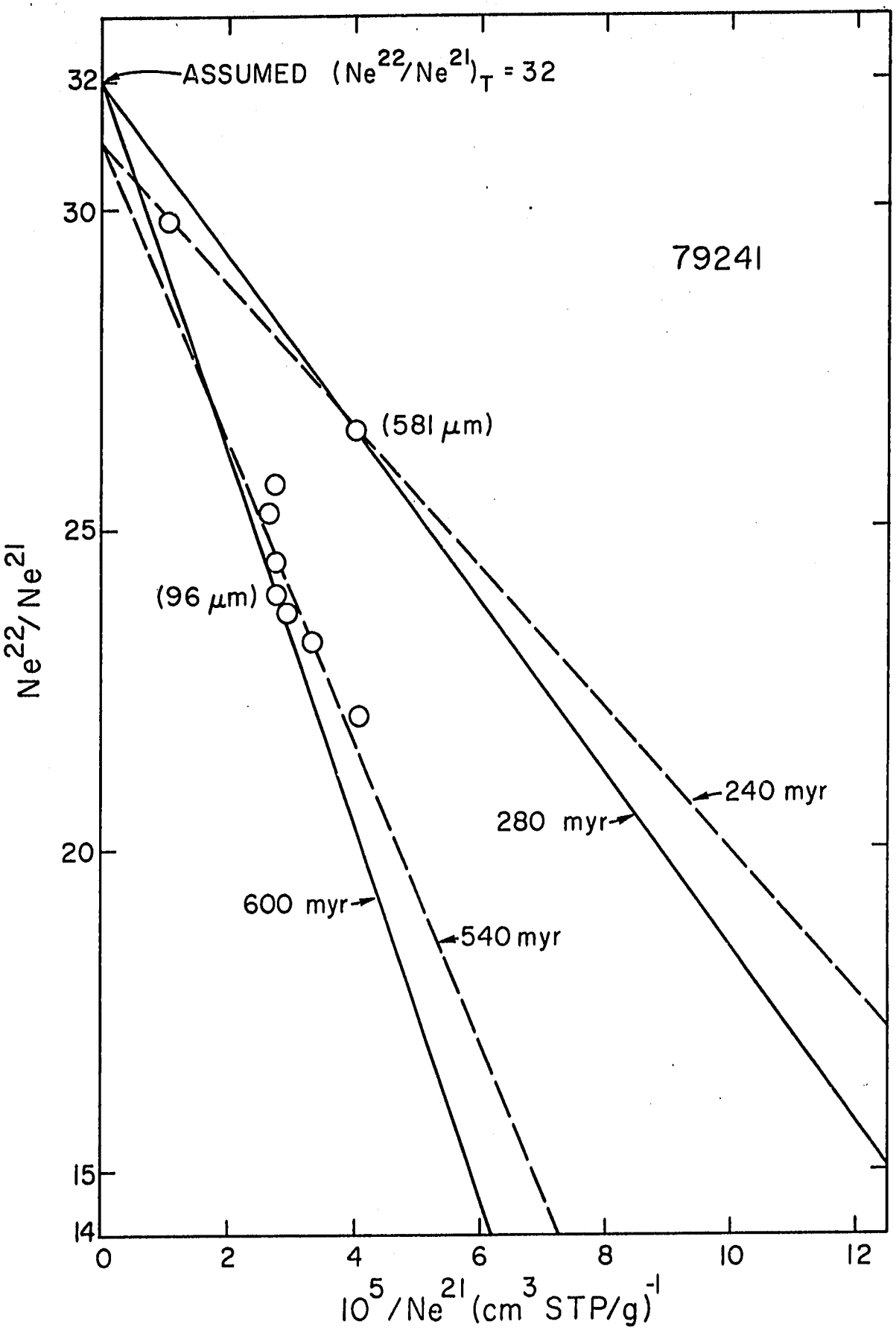
ASSUMED $(Ne^{22}/Ne^{21})_T = 32$
79241
(581 μm)
(96 μm)
240 myr
280 myr
600 myr
540 myr
Ne^{22}/Ne^{21}
$10^5/Ne^{21}$ $(cm^3$ STP/g$)^{-1}$
32
30
25
20
15
14
0
2
4
6
8
10
12

FIGURE 18

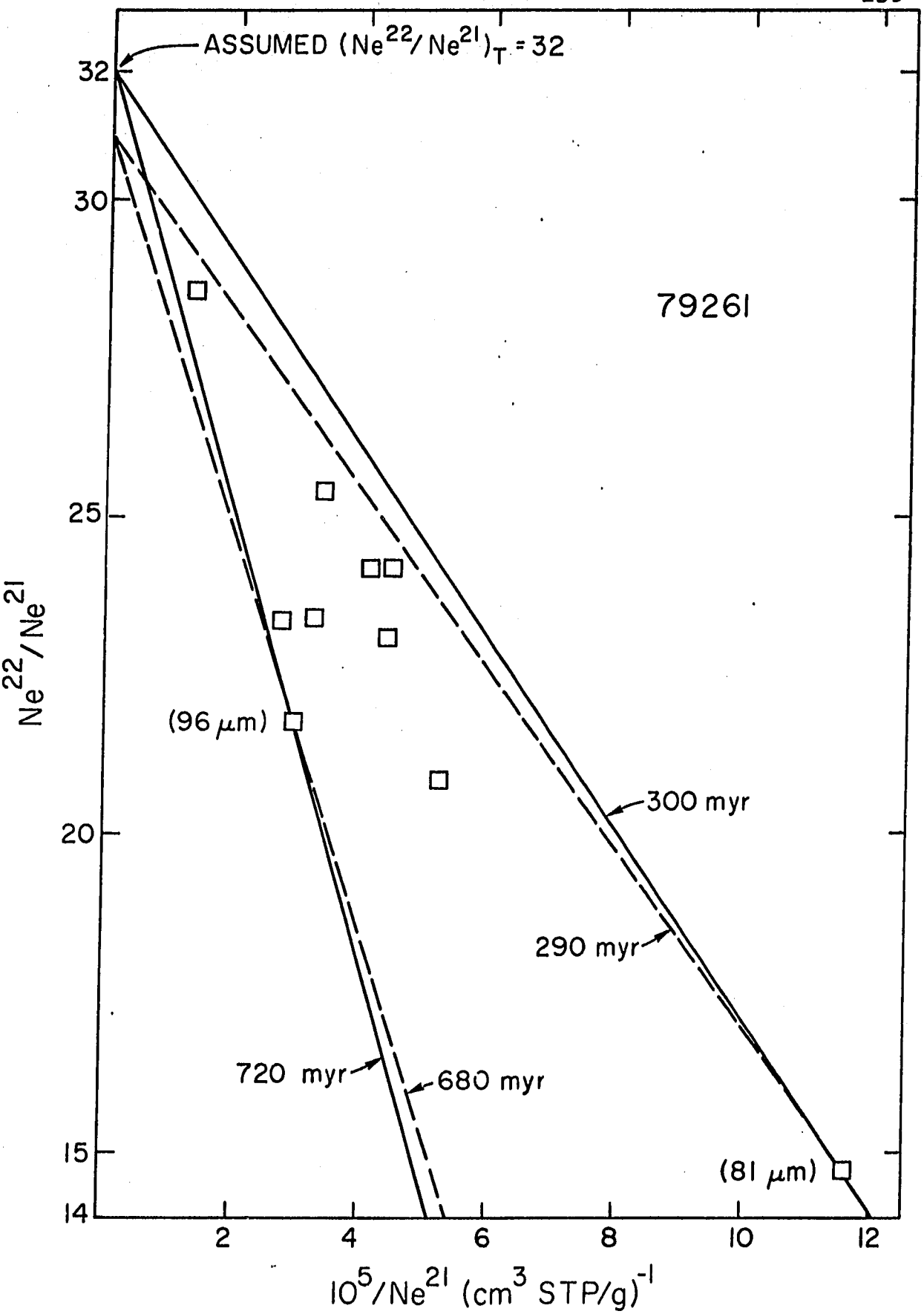
ASSUMED $(Ne^{22}/Ne^{21})_T = 32$
32
30
25
20
15
14
79261
(96 μm)
300 myr
290 myr
720 myr
680 myr
(81 μm)
2
4
6
8
10
12
Ne^{22}/Ne^{21}
$10^5/Ne^{21}$ $(cm^3$ STP/g$)^{-1}$

FIGURE 19

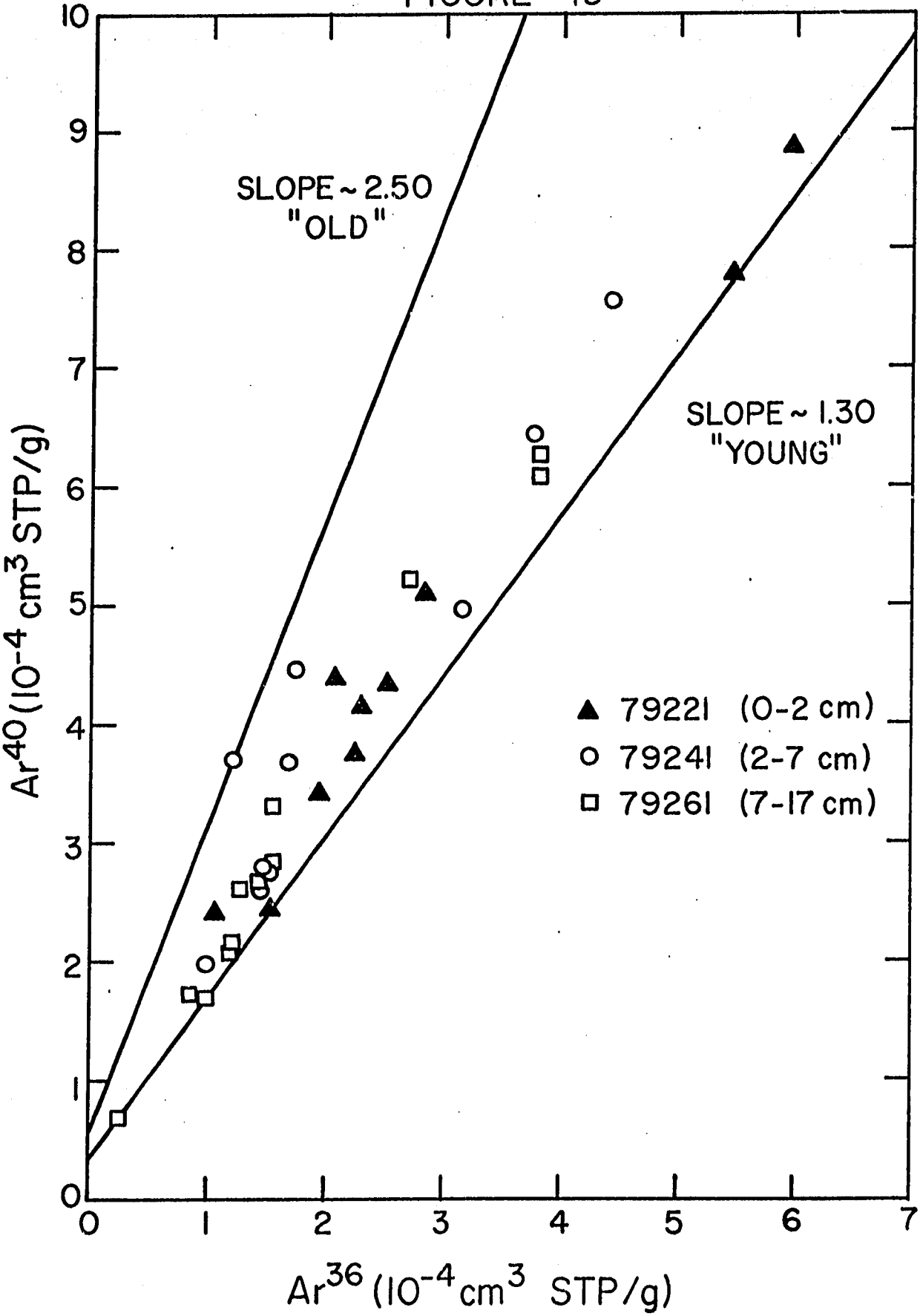
SLOPE ~ 2.50
"OLD"
SLOPE ~ 1.30
"YOUNG"
▲ 79221 (0-2 cm)
○ 79241 (2-7 cm)
□ 79261 (7-17 cm)
$Ar^{40}(10^{-4} cm^3 STP/g)$
$Ar^{36}(10^{-4} cm^3 STP/g)$
0
1
2
3
4
5
6
7
8
9
10

Bame, S. J., Hundhausen, A. J., Ashbridge, J. R., Strong, I. B., (1968), "Solar Wind Ion Composition", Phys. Rev. Lett., 20, 393-395.

Bame, S. J., Ashbridge, J. R., Hundhausen, A. J., Montgomery, M. D., (1970), "Solar Wind Ions: $^{56}Fe^{+8}$ to $^{56}Fe^{+12}$, $^{28}Si^{+7}$, $^{28}Si^{+8}$, $^{28}Si^{+9}$, and $^{16}O^{+6}$", J. Geophys. Res., 75, 6360-6365.

Baur, H., Frick, U., Funk, H., Schultz, L., Signer, P., (1972), "Thermal Release of Helium, Neon, and Argon from Lunar Fines and Materials", Proc. Third Lunar Sci. Conf., 2, 1947-1966.

Berstein, W., Fredricks, R. W., Vogl, J. L., Fowler, W. A., (1963), "The Lunar Atmosphere and the Solar Wind", Icarus, 2, 233-248.

Bibring, J. P., Chaumont, J., Comstock, G., Maurette, M., Meunier, R., (1973), "Solar Wind and Lunar Wind Microscopic Effects in the Lunar Regolith", Lunar Science IV, 72-74.

Bogard, D. D., Funkhouser, J. G., Schaeffer, O. A., Zähringer, J., (1971), "Noble Gas Abundances in Lunar Material--Cosmic-Ray Spallation Products and Radiation Ages from the Sea of Tranquillity and the Ocean of Storms", J. Geophys. Res., 76, 2757-2779.

Bogard, D. D., Nyquist, L. E., (1972a), "Noble Gas Studies on Regolith Materials from Apollo 14 and 15", Proc. Third Lunar Sci. Conf., 2, 1797-1820.

Bogard, D., D., Nyquist, L. E., (1972b), "Noble Gases in the Apollo 15 Drill Cores", The Apollo 15 Lunar Samples, 342-346.

Bogard, D.,D., Nyquist, L., (1973), "Ar^{40}/Ar^{36} Variations in Apollo 15 and 16 Regolith", Proc. Fourth Lunar Sci. Conf., 2, 1975-1986.

Bogard, D. D., Nyquist, L. E., Hirsch, W. C., Moore, D. R., (1973), "Trapped Noble Gas Abundances in Surface and Sub-Surface Fines from Apollo 15 and 16", Lunar Science IV, 79-81.

Bogard, D. D., Hirsch, W. C., Nyquist, L. E., (1974), "Noble Gases in Apollo 17 Fines: Mass Fractionation Effects in

Trapped Xe and Kr", Proc. Fifth Lunar Sci. Conf., 2, 1975-2003.

Buehler, F., Geiss, J., Meister, J., Eberhardt, P., (1966), "Trapping of the Solar Wind in Solids", Earth Planet. Sci. Lett., 1, 249-255.

Buehler, F., Eberhardt, P., Geiss, J., Meister, J., Signer, P., (1969), "Apollo 11 Solar Wind Composition Experiment: First Results", Science, 166, 1502-1503.

Butler, J. C., King, E. A., Jr., (1974), "Analysis of Grain Size-Frequency of Lunar Fines", Proc. Fifth Lunar Sci. Conf. 1, 829-842.

Cameron, A. G. W., (1968), "A New Table of Abundances of the Elements in the Solar System", Origin and Distribution of the Elements, 125-143.

Carr, M. H., Meyer, C. E., (1972), "Chemical and Petrographic Characteristics of the Regolith at the Apollo 15 Landing Site", The Apollo 15 Lunar Samples, 48-50.

Church, S. E., Tilton, G. R., (1975), "Lead Isotope Systematics of Soils and Soil Breccias from Taurus-Littrow" Lunar Science VI, 1, 143-145.

Criswell, D. R., (1972), "Lunar Dust Motion", Proc. Third Lunar Sci. Conf., 3, 2671-2680.

Criswell, D. R., (1975), "Rosiwal and Regolithic Retention of Solar Wind Elements", Lunar Science VI, 1, 169-171.

Eberhardt, P., Eugster, O., Anders, E., (1965), "Radiation Ages of Aubrites," J. Geophys. Res., 70, 4427-4434.

Eberhardt, P., Geiss J., Graf, H., Grögler, N., Krähenbühl, U., Schwaller, H., Schwarzmüller, J., Stettler, A., (1970), "Trapped Solar Wind Noble Gases, Exposure Age, and K/Ar Ages in Apollo 11 Lunar Fine Material", Proc. Apollo 11 Lunar Sci. Conf., 2, 1037-1070.

Eberhardt, P., Geiss, J., Graf, H., Grögler, N., Mendia, M. D., Mörgeli, M., Schwaller, H., Stettler, A., Krähenbühl, U., vonGuten, H. R., (1972), "Trapped Solar Wind Noble Gases in Apollo 12 Lunar Fines 12001 and Apollo 11 Breccia 10046", Proc. Third Lunar Sci. Conf., 2, 1821-1856.

Eberhardt, P., Geiss, J., Grögler, N., Stettler, A., (1973), "How Old is the Crater Copernicus?", Preprint.

Eugster, O., Grögler, N., Mendia, M. D., Eberhardt P., Geiss, J., (1973), "Trapped Solar Wind Noble Gases and

Exposure Age of Lunar 16 Lunar Fines", Geochim. et Cosmochim. Acta, 37, 1991-2004.

Fireman, E. L., (1974), "Regolith History from Cosmic-Ray Produced Nuclides", Proc. Fifth Lunar Sci. Conf., 2, 2075-2092.

Fleischer, R. L., Hart, H. R., Jr., (1974), "Uniformity of Uranium Content of Lunar Green and Orange Glasses", Lunar Science V, 1, 236-238.

Frick, U., Baur, H., Funk, H., Phinney, D., Schäfer, C., Schultz, L., Signer, P., (1973), "Diffusion Properties of Light Noble Gases in Lunar Fines", Proc. Fourth Lunar Sci. Conf., 2, 1987-2002.

Frick, U., Baur, H., Ducati, H., Funk, H., Phinney, D., Signer, P., "On the Origin of Helium, Neon, andArgon Isotopes in Sieved Mineral Separates from an Apollo 15 Soil", submitted to Geochim. et Cosmochim. Acta.

Fruchter, J. S., Stoeser, J. W., Lindstrom, M. M., Goles, G. G. (1973) "Apollo 15 Clastic Materials and their Relationship to Local Geologic Features", Proc. Fourth Lunar Sci. Conf., 2, 1227-1237.

Funkhouser, J. G., Schaeffer, O. A., Bogard, D. D., Zähringer, J., (1970), "Gas Analysis of the Lunar Surface", Proc. Apollo 11 Lunar Sci. Conf., 2, 1111-1116.

Geiss J., Eberhardt, P., Signer, P., Buehler, F., Meister, J., (1969), "The Solar-Wind Composition Experiment", Apollo 11 Preliminary Science Report, NASA SP-214, Section 8.

Goldstein, J. I., Hewins, R. H., Axon, H. J., (1974), "Metal Silicate Relationships in Apollo 17 Soils", Proc. Fifth Lunar Sci. Conf., 1, 653-671.

Heiken, G. (1974), "A Catalog of Lunar Soils", Draft, NASA.

Heiken, G., McKay, D. S., (1974), "Petrography of the Apollo 17 Soils", Proc. Fifth Lunar Sci. Conf., 1, 843-860.

Heymann, D., Yaniv, A., (1970), "Ar^{40} Anomaly in Lunar Samples from Apollo 11", Proc. Apollo 11 Lunar Sci. Conf., 2, 1261-1267.

Heymann, D., Yaniv, A., (1970), "Inert Gases in Fines from the Sea of Tranquillity", Proc. Apollo 11 Lunar Sci. Conf., 2, 1247-1253.

Heymann, D., Yaniv, A., Lakatos, S. (1972), "Inert Gases in Twelve Particles and One 'Dust' Sample from Lunar 16", Earth Planet. Sci. Lett., 13, 400-406.

Heymann, D., Lakatos, S., Walton, J.R., (1973), "Inert Gases in a Terra Sample: Measurements in Six Grain-Size Fractions and Two Single Particles from Luna 20", Geochim et Cosmochim. Acta, 37, 1991-2004.

Heymann, D., Walton, J. R., Jordan, J. L., Lakatos, S., Yaniv, A., (1975), "Light and Dark Soils at the Apollo 16 Landing Site", In Press (The Moon).

Hintenberger, H. et al. (1964), "Die Relativen Produktionsquerschnitte fur He-3 und Ne-21 aus Mg, Si, S, und Fe in Steinmeteoriten", Z. Naturforsch, 192, 88-92.

Hintenberger, H., Weber, H. W., Voshage, H., Wänke, H., Begemann, F., Wlotzka, F., (1970), "Concentrations and Isotopic Abundances of the Rare Gases, Hydrogen, and Nitrogen in Lunar Matter", Proc. Apollo 11 Lunar Sci. Conf., 2, 1269-1282.

Hintenberger, H., Weber, H. W., Takaota, N., (1971), "Concentrations and Isotopic Abundances of the Rare Gases in Lunar Matter", Proc. Second Lunar Sci. Conf., 2, 1607-1626.

Hintenberger, H., Weber, H. W., (1973), "Trapped Rare Gases in Lunar Fines and Breccias", Proc. Fourth Lunar Sci. Conf., 2, 2003-2020.

Hintenberger, H., Schultz, L., Weber, H. W., (1975), "Rare Gases in Ilmenite and Bulk Samples of Apollo 17 Soils and Breccias", Lunar Science VI, 1, 370-372.

Housley, R. M., Grant, R. W., Abdel-Gawad, M., (1972), "Study of Excess Fe Metal in the Lunar Fines by Magnetic Separation, Mössbauer Spectroscopy, and Microscope Examination", Proc. Third Lunar Sci. Conf., 1, 1065-1076.

Hübner, W., Heymann, D., Kirsten, T., (1973), "Inert Gas Stratigraphy of Apollo 15 Drill Core Sections 15001 and 15003", Proc. Fourth Lunar Sci. Conf., 2, 2021-2036.

Hundhausen, A. J., Ashbridge, J. R., Bame, S. J., Gilbert, H. E., Strong, I. B., (1967), "Vela-3 Satellite Observations of Solar Wind Ions: A Preliminary Report", J. Geophys. Res., 72, 87-100.

Husain, L., Schaeffer, O. A., Funkhouser, J., Sutter, J., (1972), "The Ages of Lunar Material from Fra Mauro, Hadley

Rille, and Spur Crater", Proc. Third Lunar Sci. Conf., 2, 1557-1567.

Jordan, J. L., Heymann, D., Lakatos, S., (1974), "Inert Gas Patterns in the Regolith at the Apollo 15 Landing Site", Geochim. et Cosmochim. Acta, 38, 65-78.

Kirsten, T., Müller, O., Steinbrunn, F., Zähringer, J., (1970), "Study of Distribution and Variations of Rare Gases in Lunar Material by Microprobe Technique", Proc. Apollo 11 Lunar Sci. Conf., 2, 1331-1344.

Kirsten, T., Steinbrunn, F., Zähringer, J., (1971), "Location and Variation of Trapped Rare Gases inApollo 12 Lunar Samples", Proc. Second Lunar Sci. Conf., 2, 1651-1670.

Kirsten, T., Deubner, J., Horn, P., Kaneota, I., Kiko, J., Schaeffer, O.A., Thio, S. K., (1972), "The Rare Gas Record of Apollo 14 and 15 Samples", Proc. Third Lunar Sci. Conf., 2, 1865-1889.

Kirsten, T., Horn, P., (1974), "Chronology of the Taurus-Littrow Region III: Ages of Mare Basalts and Highland Breccias and Some Remarks about the Interpretation of Lunar Highland Rock Ages", Proc. Fifth Lunar Sci. Conf., 2, 1451-1476.

Lakatos, S., Heymann D., Yaniv, A., (1973), "Green Spherules from Apollo 15: Inferences about their Origin from Rare Gas Measurements", The Moon, 7, 132-148.

Lunar Science Preliminary Examination Team, (1972), "Preliminary Examination of Lunar Samples", Apollo 15 Preliminary Science Report, NASA Sp-289, Section 6.

Lunar Science Preliminary Examination Team, (1973), "Preliminary Examination of Lunar Samples", Apollo 17 Preliminary Science Report, NASA SP-330, Section 7.

Manka, R. H., Michel, F. C., (1970), "Lunar Atmosphere as a Source of Argon 40 and Other Lunar Surface Elements", Science, 169, 278-280.

Manka, R. H., Michel, F. C., (1971), "Lunar Atmosphere as a Source of Lunar Surface Elements", Proc. Apollo 11 Lunar Sci. Conf., 2, 1717-1728.

McGetchin, T. R., Settle, M., Head, J. W., (1973), "Radial Thickness Variation in Impact Crater Ejecta: Implications for Lunar Basin Deposits", Earth Planet. Sci. Lett., 20, 226-336.

McKay, D. S., Fruland,R. M., Heiken, G. H., (1974), "Grain Size and the Evolution of Lunar Soils", Proc. Fifth Lunar Sci. Conf., 1, 887-906.

Moore, C. B., Lewis, C. F., Cripe, J. D., (1974), "Total Carbon and Sulfur Compounds of Apollo 17 Samples", Proc. Fifth Lunar Sci. Conf., 2, 1897-1906.

Muehlberger, W. R., Batson, R. M., Cernan, E. A., Freeman, V. L., Hait, M. H., Holt, H. E., Howard, K. A., Jackson, E. D., Larson, K. B., Reed, V. S., Rennilson, J. J., Schmitt, H. H., Scott, D. H., Sutton, R. L., Stuart-Alexander, D., Swann, G. A., Trask, N. J., Ulrich, G. E., Wilshire, H. G., Wolfe, E. W., (1973), "Preliminary Geologic Investigation of the Apollo 17 Landing Site", Apollo 17 Preliminary Science Report, NASA,SP-330, Section 6.

Nunes, P. D., Tatsumoto, M., Unruh, D. M., (1974), "U-Th-Pb Systematics of Some Apollo 17 Lunar Samples and Implications for a Lunar Basin Excavation Chronology", Proc. Fifth Lunar Sci. Conf., 2, 2075-2092.

Ogilvie, K. W., Burlaga, L. F., Wilkerson, T. D., (1968), "Plasma Observations on Explorer 34", J. Geophys. Res., 73, 6809-6824.

Pepin, R. O., Bradley, J. G., Dragon, J. C., Nyquist, L. E., (1972), "K-Ar Dating of Lunar Fines: Apollo 12, Apollo 14, and Luna 16", Proc. Third Lunar Sci. Conf.,2, 1589-1612.

Podosek, F. A., Huneke, J. C., Burnett, D. S., Wasserburg, G. J., (1971), "Isotopic Composition of Xenon and Krypton in Lunar Soil and Solar Wind", Earth Planet. Sci. Lett., 10, 199-216.

Powell, B. M., Aitken, E. K., Weiblen, P. W., (1973), "Classification, Distribution, and Origin of Lithic Fragments From the Hadley-Apennine Region", Proc. Fourth Lunar Sci. Conf., 1, 445-460.

Reynolds, J. H., (1956), "High Sensitivity Mass Spectrometer for Noble Gas Analysis", Review of Scientific Instruments, 27, 928-934.

Robbins, D. E., Hundhausen, A. J., Bame, S. J., (1970), "Helium in the Solar Wind", J. Geophys. Res., 75, 1178-1187.

Rose, J. H., Jr., Cuttita, F., Berman, S., Brown, F. W., Carron, M. K., Christian, R. P., Dwornik, E. J. Greenland, L. P., (1974), "Chemical Composition of Rocks and Soils

at Taurus-Littrow", Proc. Fifth Lunar Sci. Conf., 1, 1119-1134.

Schaeffer, O. A., Funkhouser, J. G., Bogard, D. D., Zähringer, J., (1970), "Potassium-Argon Ages of Lunar Rocks from Mare Tranquilitatis and Oceanus Procellarum", Science, 170, 2757-2779.

Schaeffer, O. A., Husain, L., Sutter, J., Funkhouser, J., Kirsten, T., Kaneoka, I., (1972), "The Ages of Lunar Materials from Fra Mauro and the Hadley Rille - Apennine Front Area", Lunar Science, III, 675-677.

Schmitt, H. H., Cernan, E. A., (1973), "A Geological Investigation of the Taurus-Littrow Valley", Apollo 17 Preliminary Science Report, NASA SP-330, Section 5.

Snyder, C. W., Neugebauer, M., (1964), "Interplanetary Solar-Wind Measurements by Mariner II", Space Res., 4, 89-113.

Stauffer, H., (1962), "On the Production Ratios of Rare Gas Isotopes in Stone Meteorites", J. Geophys. Res., 67, 2023-2028.

Swann, G. A., Bailey, N. G., Batson, R. M., Freeman, V. L., Hait, M. H., Head, J. S., Holt, H. E., Howard, K. A., Irwin, J. B., Larson, K. B., Muehlberger, W. R., Reed, V. S., Rennilson, J. J., Schaber, G. G., Scott, D. R., Silver, L. T., Sutton, R. L., Ulrich, G. E., Wilshire, H. G., Wolfe, E. W., (1972), "Preliminary Geologic Investigation of the Apollo 15 Landing Site", Apollo 15 Preliminary Science Report, NASA SP-289, Section 5.

Walton, J. R., Lakatos, S., Heymann, D., (1973), "Distribution of Inert Gases in Fines from the Cayley-Descartes Region", Proc. Fourth Lunar Sci. Conf., 2, 2079-2096.

Walton, J. R., (1974), "Production of Helium, Neon, and Argon in Lunar Material by Solar Cosmic Ray Protons", Ph.D. Thesis, Rice University.

Wänke, H., Palme, H., Spettel,B., Teschke, F., (1972), "Multielement Analyses and a Comparison of the Degree of Oxidation of Lunar and Meteoritic Matter", The Apollo 15 Lunar Samples, 265-267.

Wänke, H., Baddenhausen, H., Dreibus, G., Jagoritz, E., Kruse, H., Palme, H., Spettel, B., Teschke, F., (1973), "Multielement Analyses of Apollo 15, 16, and 17 Samples and the Bulk Composition of the Moon", Proc. Fourth Lunar Sci. Conf., 2, 1461-1481.

Wolfe, J. H., Silva, R. W., McKibben, D. D., Mason, R. H., (1966), "The Compositional, Anisotropic, and Nonradial Flow Characteristics of the Solar Wind", J. Geophys. Res., 71, 3329-3335.

Yaniv, A., Heymann, D., (1971), "Inert Gases from Apollo 11 and Apollo 12 Fines: Reversals in the Trends of Relative Element Abundances", Earth Planet. Sci. Lett., 10, 387-391.

Yaniv, A., Heymann, D., (1972), "Atmospheric Ar^{40} in Lunar Fines", Proc. Third Lunar Sci. Conf., 2, 1967-1980.

Yaniv, A., Taylor, G. J., Allen, S., Heymann, D., (1971), "Stable Rare Gas Isotopes Produced by Solar Flares in Single Particles", Proc. Second Lunar Sci. Conf., 2, 1705-1715.